ISSN 1450-7404

Journal of Research in Physics

Volume 31
Number 1
2007

DEPARTMENT OF PHYSICS

Faculty of Sciences
University of Novi Sad - Novi Sad - Serbia

Journal of Research in Physics

Published by: Department of Physics, Faculty of Sciences, University of Novi Sad,
Trg Dositeja Obradovića 4, 21000 Novi Sad, Serbia

Phone: +381-21-455318 Fax: +381-21-459367 E-mail: fizika@uns.ns.ac.yu
http://www.if.ns.ac.yu

Journal of Research in Physics Vol. 31, No. 1, 1 - 9 (2007)

Poincare Generators as Quadratic Heisenberg Operators and Equations of Motion

Igor Salom
Institute of Physics, P.O. Box 57, 11001 Belgrade, Serbia
e-mail: isalom@phy.bg.ac.yu

Received: *May 3, 2006*

Abstract

A particular scheme for obtaining conformal algebra (and its Poincare subalgebra) using quadratic polynomials of some abstract Heisenberg algebra operators κ^α and π_α is demonstrated. Such a setup turns out to be suitable for many purposes. In this paper the emphasis is put on the fact that in this approach massless Klein-Gordon, massless Dirac and free-field Maxwell equations show up as mathematical tautologies.

Key words: Poincare symmetry, conformal symmetry, free-field equations of motion

1. Introduction

Due to its enormous fundamental importance, Poincare symmetry and everything related to it draw continuous interest of physicists. In that sense the models where this symmetry is treated or realized in some alternative way, or models where this symmetry is a nontrivial subgroup of a larger symmetry, deserve in our opinion close attention.

In this paper we investigate a model where Poincare generators, as well as conformal generators, are constructed as quadratic polynomials of some abstract operators satisfying Heisenberg algebra. This concrete realization of Poincare algebra turns out to be interesting from various aspects. First of all, it is potentially interesting as the Poincare and conformal algebras here appear as a part of a larger symmetry, where a relatively simple form of symmetry breaking is required to reduce this larger symmetry to the observable symmetries [1].[1] Even if we ignore the existence of this larger symmetry, expressing of Poincare generators as quadratic functions of Heisenberg operators in this particular way allows a simplified treatment of some physical concepts. Such is the concept of electromagnetic duality symmetry that we analyzed in this context in [1]. In this approach, the generator of duality symmetry appears on the same footage with the rest of the Poincare generators, and it also turns out to generate chiral symmetry as well. It is also a curiosity of this approach that the whole conformal algebra is realized in a Hilbert space

---

[1] It can be argued that this larger algebra is, in some sense, simpler than the Poincare and conformal algebras, since its structural constants are derivable from Heisenberg algebra relations. Thus, this possibility might be attractive for those unsatisfied with discrepancy of alleged deepest fundamentality and still a significant complexity of the Poincare algebra.

of first quantization, and also in such a way which naturally allows states of half-integer angular momentum. Additionally, a slight modification of this model which is appropriate for describing multi-particle states offers a different insight into connection of spin and statistics.[2] Finally, an interesting feature of this approach is the fact that free equations of motion show up here as unavoidable mathematical tautologies, rather than as additional dynamical constraints put on the kinematic basis of a theory (which is otherwise common). It is this last property of the model that we wish to concentrate on in this paper.

The paper is organized as follows: in section 2 we construct conformal algebra in four dimensions $C(1,3)$ in terms of the Heisenberg algebra operators. In section 3 we point out mathematical identities of which some will be later shown to turn into equations of motion. In section 4 we construct single particle Hilbert space and derive free equations of motion. A brief comparison with Lagrangian prescription for obtaining the same equations of motion is also made. Finally, section 5 summarizes the results.

Throughout the text, Latin indices $i, j, k, \ldots$ will take values 1, 2 and 3, Greek indices from the beginning of alphabet $\alpha, \beta, \ldots$ will take values from 1 to 4 and will in general denote Dirac-like spinor indices, while Greek indices from the middle of alphabet $\mu, \nu, \ldots$ will take values from 0 to 3, denoting Lorentz four-vector indices.

2. Constructing Poincare algebra from Heisenberg operators

Let operators κ^α and π_α satisfy Heisenberg algebra in four dimensions [3]:

$$[\kappa^\alpha, \pi_\beta] = i\delta^\alpha_\beta, \quad [\kappa^\alpha, \kappa^\beta] = [\pi_\alpha, \pi_\beta] = 0. \tag{1}$$

There are three types of quadratic combinations of these operators: quadratic in κ^α, quadratic in π_α and mixed. Hermitian operators of each of these kinds can be written in matrix notation, respectively as:

$$\widehat{(A)}_{\kappa\kappa} \equiv A_{\alpha\beta}\kappa^\alpha\kappa^\beta, \qquad \widehat{(A)}_{\pi\pi} \equiv A^{\alpha\beta}\pi_\alpha\pi_\beta, \qquad \widehat{(A)}_{\pi\kappa} \equiv A^\alpha_\beta \frac{1}{2}\{\pi_\alpha, \kappa^\beta\}, \tag{2}$$

where A is an arbitrary four-by-four real matrix.[4] However, due to commutativity of the operators κ^α among themselves, and π_α among themselves, matrices appearing in definitions $\widehat{(A)}_{\kappa\kappa}$ and $\widehat{(A)}_{\pi\pi}$ are implied to be symmetric.

Such quadratic operators form an algebra with commutation relations easily derived from the Heisenberg algebra relations:

$$\begin{array}{ll} [\widehat{(A)}_{\pi\kappa}, \widehat{(B)}_{\pi\kappa}] = i(\widehat{[A,B]})_{\pi\kappa}, & [\widehat{(A)}_{\pi\kappa}, \widehat{(B)}_{\pi\pi}] = i(\widehat{AB+BA^T})_{\pi\pi}, \\ [\widehat{(A)}_{\pi\kappa}, \widehat{(B)}_{\kappa\kappa}] = -i(\widehat{[A^TB+BA]})_{\kappa\kappa}, & [\widehat{(A)}_{\pi\pi}, \widehat{(B)}_{\kappa\kappa}] = -4i(\widehat{AB})_{\pi\kappa}, \\ [\widehat{(A)}_{\kappa\kappa}, \widehat{(B)}_{\kappa\kappa}] = 0, & [\widehat{(A)}_{\pi\pi}, \widehat{(B)}_{\pi\pi}] = 0, \end{array} \tag{3}$$

To reveal the Poincare subalgebra in this structure, first we choose a set of six real matrices σ_i and $\tau_{\underline{i}}$, $i, \underline{i} = 1,2,3$ (four-dimensional analogues of Pauli matrices) satisfying

$$[\sigma_i, \sigma_j] = 2\varepsilon_{ijk}\sigma_k, \qquad [\tau_{\underline{i}}, \tau_{\underline{j}}] = 2\varepsilon_{\underline{ijk}}\tau_{\underline{k}}, \qquad [\sigma_i, \tau_{\underline{j}}] = 0, \tag{4}$$

---

[2] This we hope to elaborate on some later occasion.

[3] In spite of this, we stress that these operators do not represent coordinates and momenta. Furthermore, they will turn out to transform like Dirac spinors.

[4] A hat sign over a matrix will be used to emphasize the difference between the operator obtained from a matrix in the sense of definition (2) and the matrix itself.

as a basis of antisymmetric four-by-four real matrices[5] (we distinct tau indices from sigma indices by underlining the former). However, unlike Pauli matrices, these matrices are anti-hermitian, satisfying $\sigma_i^2 = \tau_{\underline{i}}^2 = -1$. As a basis for symmetric matrices we choose nine matrices $\alpha_{\underline{i}j} \equiv \tau_{\underline{i}}\sigma_j$ and a unit matrix denoted as α_0. In order to establish, later on, connection with standard notation, we state one corresponding representation of Dirac gamma matrices:

$$\gamma_0 = i\tau_{\underline{2}}, \qquad \gamma_i = \gamma_0\alpha_{\underline{3}i} = i\tau_{\underline{1}}\sigma_i, \qquad \gamma_5 = -i\gamma_0\gamma_1\gamma_2\gamma_3 = i\tau_{\underline{3}}. \tag{5}$$

Now, the set of 36 operators

$$\left\{\widehat{(\tau_{\underline{i}})}_{\pi\kappa}, \widehat{(\sigma_j)}_{\pi\kappa}, \widehat{(\alpha_0)}_{\pi\kappa}, \widehat{(\alpha_{\underline{i}j})}_{\pi\kappa}, \widehat{(\alpha_0)}_{\pi\pi}, \widehat{(\alpha_{\underline{i}j})}_{\pi\pi}, \widehat{(\alpha_0)}_{\kappa\kappa}, \widehat{(\alpha_{\underline{i}j})}_{\kappa\kappa}\right\} \tag{6}$$

can be chosen as the basis of algebra of quadratic operators.

Among the operators from this set, let us discard all those with underlined index having values $\underline{1}$ and $\underline{2}$. This resembles an idea of introducing a "preferred tau direction" (here, for concreteness, this "direction" was taken to be along the third "axis") and dropping out each entity which has tau indices but is not along this preferred direction. What we are left with is a subalgebra isomorphic with conformal algebra C(1,3) plus one additional generator that commutes with the rest of the subalgebra. Now we introduce new notation for the remaining generators:

$$M_{ij} = \varepsilon_{ijk}J_k \equiv \varepsilon_{ijk}\widehat{\left(\frac{\sigma_k}{2}\right)}_{\pi\kappa}, \quad M_{i0} = -M_{0i} = N_i \equiv \widehat{\left(\frac{\alpha_{\underline{3}i}}{2}\right)}_{\pi\kappa}, \quad D \equiv \widehat{\left(\frac{\alpha_0}{2}\right)}_{\pi\kappa},$$

$$P_i \equiv \widehat{\left(\frac{\alpha_{\underline{3}i}}{2}\right)}_{\pi\pi}, \quad P_0 \equiv \widehat{\left(\frac{\alpha_0}{2}\right)}_{\pi\pi}, \quad K_i \equiv \widehat{\left(\frac{\alpha_{\underline{3}i}}{2}\right)}_{\kappa\kappa}, \quad K_0 \equiv -\widehat{\left(\frac{\alpha_0}{2}\right)}_{\kappa\kappa} \tag{7}$$

The additional remaining operator is

$$Y_{\underline{3}} \equiv \widehat{\left(\frac{\tau_{\underline{3}}}{2}\right)}_{\pi\kappa}, \tag{8}$$

which commutes with all of the conformal generators.

We note that the entire algebra of all quadratic operators (2) that embeds the conformal algebra (7) is isomorphic with symplectic algebra in four dimensions. As most of the attempts to embed Poincare group seek the larger symmetry in the form of $GL(4,R)$ group, diffeomorphism group, or Poincare group of higher dimension, this approach is a novel one [2, 3].

3. Algebraic identities

Structural constants of conformal algebra in this approach are not simply "put by hand" like usually, but are instead contained in the combination of definitions (7) with the Heisenberg algebra of operators κ^α and π_α. However, commutation relations between quadratic operators (and hence among conformal generators) are not the only consequence

---

[5] One possible realization of such matrices is, for example: $\sigma_1 = -i\sigma_y \times \sigma_x$, $\sigma_2 = -iI_2 \times \sigma_y$, $\sigma_3 = -i\sigma_y \times \sigma_z$, $\tau_1 = i\sigma_x \times \sigma_y$, $\tau_2 = -i\sigma_z \times \sigma_y$, $\tau_3 = -i\sigma_y \times I_2$, where σ_x, σ_y and σ_z are standard two-dimensional Pauli matrices and I_2 is a two-dimensional unit matrix.

of the Heisenberg algebra of starting operators. By virtue of Heisenberg algebra (1) quadratic operators when expressed using τ, σ and α matrices turn out to satisfy many nontrivial mathematical identities. Of particular interest are identities:

$$\varepsilon_{\underline{ijk}}\varepsilon_{lmn}\widehat{(\alpha_{\underline{i}l})}_{\pi\pi}\widehat{(\alpha_{\underline{j}m})}_{\pi\pi} = \widehat{(\alpha^0)}_{\pi\pi}\widehat{(\alpha_{\underline{k}n})}_{\pi\pi}, \tag{9}$$

$$\widehat{(\alpha_{\underline{i}j})}_{\pi\pi}\widehat{(\sigma_j)}_{\pi\kappa} = -\widehat{(\alpha_0)}_{\pi\pi}\widehat{(\tau_{\underline{i}})}_{\pi\kappa}, \qquad \widehat{(\alpha_{\underline{i}j})}_{\pi\pi}\widehat{(\tau_{\underline{i}})}_{\pi\kappa} = -\widehat{(\alpha_0)}_{\pi\pi}\widehat{(\sigma_j)}_{\pi\kappa}, \tag{10}$$

and the following "orthogonality" relations:

$$\widehat{(\alpha_{\underline{i}j})}_{\pi\pi}\widehat{(\alpha_{\underline{i}k})}_{\pi\pi} = \delta_{jk}\widehat{(\alpha_0)}^2_{\pi\pi}, \qquad \widehat{(\alpha_{\underline{j}i})}_{\pi\pi}\widehat{(\alpha_{\underline{k}i})}_{\pi\pi} = \delta_{\underline{j}k}\widehat{(\alpha_0)}^2_{\pi\pi}. \tag{11}$$

Summation over repeated indices is implied.

There is a way to prove these identities by establishing a formal parallel of the quantities appearing in them with quantities appearing in the description of two different Euclidean three-dimensional coordinate systems. In that picture the operators $\widehat{(\alpha_{\underline{i}j})}_{\pi\pi}$ are "proportional" to the transition coefficients $\vec{e}_{\underline{i}} \cdot \vec{e}_j$ connecting two coordinate bases, while the operators $\widehat{(\sigma_i)}_{\pi\kappa}$ and $\widehat{(\tau_{\underline{i}})}_{\pi\kappa}$ correspond to angular momenta components in two referential systems, respectively. Then equations (11) correspond to orthogonality of rows and columns of the transition matrix $\vec{e}_{\underline{i}} \cdot \vec{e}_j$; identity (9) reflects the fact that vector product of two coordinate unit vectors equals the third unit vector, while relations (10) match expressions for angular momenta along the axes of one system decomposed along the axes of the other. We underline again that this correspondence is of purely formal mathematical character. Anyhow, we shall not elaborate this in any more detail.

Of course, a less elegant way to verify these results is by a direct calculation by taking some concrete choice of σ and τ matrices (in which case it suffices to choose some concrete values of free indices while the rest of the results would directly follow from the reasons of symmetry).

In the next section we will demonstrate that the massless free-field Klein-Gordon, Dirac and Maxwell equations are hidden among these mathematical tautologies.

But before that, let us notice that by choosing $\underline{i} = 3$ the first equation of (10) can be rewritten as

$$\vec{P} \cdot \vec{J} = P^0 Y_{\underline{3}}. \tag{12}$$

It reveals that the operator $Y_{\underline{3}}$ is in fact the helicity operator. (Note that $\vec{P} \cdot \vec{J} = -(P_1 J_1 + P_2 J_2 + P_3 J_3)$.)

Also, the algebraic identity obtained from (11) by taking $k = j = 3$ and rewriting it as

$$\eta^{\mu\nu} P_\mu P_\nu = (P_0)^2 - (P_1)^2 - (P_2)^2 - (P_3)^2 = 0 \tag{13}$$

implies that all states in this Hilbert space must be massless (not surprising due to the existence of conformal symmetry), so the value of energy P_0 is always simply the magnitude of spatial momentum.

4. Equations of motion

Let us consider single particle Hilbert space, which is analogue of the Hilbert space of non-relativistic quantum mechanics with operators of coordinates and momenta replaced by four pairs of $(\kappa^\alpha,\ \pi_\alpha)$ operators. In this space there exist basis vectors $|p,\theta,\varphi,y_{\underline{3}}\rangle$ that are eigenstates of both helicity operator $Y_{\underline{3}}$ and spatial momentum:

$$\begin{aligned} Y_{\underline{3}}|p,\theta,\varphi,y_{\underline{3}}\rangle &= y_{\underline{3}}|p,\theta,\varphi,y_{\underline{3}}\rangle, & P^1|p,\theta,\varphi,y_{\underline{3}}\rangle &= p\sin\theta\cos\varphi\ |p,\theta,\varphi,y_{\underline{3}}\rangle, \\ P^2|p,\theta,\varphi,y_{\underline{3}}\rangle &= p\sin\theta\sin\varphi\ |p,\theta,\varphi,y_{\underline{3}}\rangle, & P^3|p,\theta,\varphi,y_{\underline{3}}\rangle &= p\cos\theta\ |p,\theta,\varphi,y_{\underline{3}}\rangle, \end{aligned} \tag{14}$$

where $p\in[0,\infty),\theta\in[0,\pi],\varphi\in[0,2\pi)$ and $y_{\underline{3}}=0,\pm\frac{1}{2},\pm1,\ldots$ Spherical expressions for momenta eigenvalues are more appropriate here, since detailed calculation reveals that components of wave functions that have half-odd integer values of helicity must be 2π antiperiodic in angle φ when expressed in this basis. Normalization of the states is chosen to provide that under Lorentz transformations they transform as: $\Lambda|\vec{p},y_{\underline{3}}=0\rangle=\sqrt{\frac{p'^0}{p^0}}|\vec{\Lambda p},y_{\underline{3}}=0\rangle$.

Next, we define *scalar field vectors*, namely Hilbert space vectors that correspond to states of a single scalar particle created at a given point x:

$$|\phi(x)\rangle\equiv\int_{\Re^3}\frac{d^3p}{(2\pi)^{3/2}}\frac{1}{\sqrt{2p^0}}\,e^{ip_\mu x^\mu}|\vec{p},y_{\underline{3}}=0\rangle. \tag{15}$$

Such vectors have simple Lorentz transformation properties: $\Lambda|\phi(x)\rangle=|\phi(\Lambda x)\rangle$.[6]

For an arbitrary Hilbert state $|f\rangle$ we define its *scalar field representation* as $\phi_f(x)\equiv\langle\phi(x)|f\rangle$. Direct calculation shows that the action of conformal generators in this representation (defined for arbitrary generator G as $G\phi_f(x)\equiv\langle\phi(x)|G|f\rangle$) reduces to standard formulas for classical fields, so in particular it holds

$$P_\mu\phi_f(x)\equiv\langle\phi(x)|P_\mu|f\rangle=i\partial_\mu\phi_f(x). \tag{16}$$

By using identity (13) it is now easy to show that the scalar field representation function of an arbitrary state satisfies the massless Klain-Gordon equation:

$$0=\langle\phi(x)|(-P^\mu P_\mu)|f\rangle=\partial^\mu\partial_\mu\phi_f(x). \tag{17}$$

The helicity $\pm\frac{1}{2}$ states are obtained by applying the π_α operators to the scalar states. As these operators transform under the spinor representation of Lorentz group (as can be verified by calculating the commutator $[M_{\mu\nu},\pi_\alpha]$), the states

$$|\psi_\alpha(x)\rangle\equiv\sqrt{2}\pi_\alpha|\phi(x)\rangle \tag{18}$$

transform like spinors. More precisely, the function

$$\psi_{f\alpha}(x)\equiv\langle\psi_\alpha(x)|f\rangle, \tag{19}$$

that we are going to call *spinor field representation* of a state $|f\rangle$, transforms as a classical spinor field, under both Lorentz and conformal group. In particular, we find:

$$P_\mu\psi_{f\alpha}(x)=i\partial_\mu\psi_{f\alpha}(x)\ \text{ and }\ M_{\mu\nu}\psi_{f\alpha}(x)=i\left((x_\mu\partial_\nu-x_\nu\partial_\mu)\delta_\alpha^\beta+(\sigma_{\mu\nu})_\alpha^\beta\right)\psi_{f\beta}(x) \tag{20}$$

---

[6] Uniqueness of these vectors can be better understood if the vector $|\phi(0)\rangle$ is expressed in the basis $|\pi_1,\pi_2,\pi_3,\pi_4\rangle$ of the operator π_α eigenstates, where its wave function is simply a constant ($|\phi(0)\rangle\sim\int d^4\pi|\pi_1,\pi_2,\pi_3,\pi_4\rangle$). Action of any κ^α operator on such state vanishes, so it is obviously invariant under the action of any operator of the form $A^\alpha_\beta\pi_\alpha\kappa^\beta$, including Lorentz generators.

where, as usually, $\sigma_{\mu\nu} \equiv \frac{1}{4}[\gamma_\mu, \gamma_\nu]$. For the action of the $Y_{\underline{3}}$ operator in the spinor field representation we find:

$$Y_{\underline{3}}\psi_{f\alpha}(x) \equiv \langle\psi_\alpha(x)|Y_{\underline{3}}|f\rangle = i(\frac{\tau_{\underline{3}}}{2})_\alpha^\beta\,\psi_{f\beta}(x) = \frac{1}{2}(\gamma_5)_\alpha^\beta\,\psi_{f\beta}(x). \tag{21}$$

Just as in the scalar field case, it is easily shown that the massless Klein-Gordon equation is satisfied. Now we shall demonstrate that the function $\psi_{f\alpha}(x)$ for an arbitrary state $|f\rangle$ satisfies also the Dirac equation. Using results (20) and (21) mathematical identity (12) directly leads to the massless Dirac equation for spinor field functions:

$$\begin{aligned} 0 &= \langle\psi_\alpha(x)|P_0 Y_{\underline{3}} + \sum_i P_i J_i|f\rangle \\ &= \left(\frac{i}{2}(\gamma_5)_\alpha^\beta\,\partial_0 + \sum_{ijk} i\partial_i\,\varepsilon_{ijk}\left(ix_j\partial_k\,\delta_\alpha^\beta + \frac{i}{2}(\sigma_{jk})_\alpha^\beta\right)\right)\psi_{f\beta}(x) \\ &= \left(\frac{i}{2}(\gamma_5)_\alpha^\beta\,\partial_0 - \sum_i \frac{i}{2}(\gamma_5\gamma_0\gamma_i)_\alpha^\beta\,\partial_i\right)\psi_{f\beta}(x). \end{aligned} \tag{22}$$

Suppressing the spinorial indices and multiplying by $2\gamma_0\gamma_5$ from the left, we obtain the massless Dirac equation in its standard form:

$$i\gamma^\mu\partial_\mu\psi_f(x) = 0. \tag{23}$$

Just as we applied π_α operators once to scalar field vectors in order to obtain the basis for helicity $\pm\frac{1}{2}$ states, we can apply these operators twice, i.e. $\pi_\alpha\pi_\beta|\phi(x)\rangle$, to obtain the basis for field representation of helicity ± 1 states. However, four out of ten possible quadratic combinations of $\pi_\alpha\pi_\beta$ will not change helicity – these are the ones corresponding to momenta (since momenta commute with $Y_{\underline{3}}$). Using the six remaining combinations we define E and B vectors:

$$|E_i(x)\rangle \equiv \widehat{(\alpha_{\underline{1}i})}_{\pi\pi}|\phi(x)\rangle, \qquad |B_i(x)\rangle \equiv -\widehat{(\alpha_{\underline{2}i})}_{\pi\pi}|\phi(x)\rangle. \tag{24}$$

Here, the linear combination $|E_i(x)\rangle \mp i|B_i(x)\rangle$ has the helicity value ± 1.

Corresponding E and B field representation functions:

$$E_{fi}(x) \equiv \langle E_i(x)|f\rangle, \qquad B_{fi}(x) \equiv \langle B_i(x)|f\rangle, \tag{25}$$

have the same Lorentz transformation properties as electric and magnetic field, respectively.[7]

To derive one pair of free field Maxwell equations we can use identities (9) and directly obtain:

$$\begin{aligned} (\vec{\nabla}\times\vec{E}_f(x))_i &= \langle\phi(x)|\frac{1}{2i}\varepsilon_{ijk}\widehat{(\alpha_{\underline{3}j})}_{\pi\pi}\widehat{(\alpha_{\underline{1}k})}_{\pi\pi}|f\rangle = \langle\phi(x)|\frac{1}{2i}\widehat{(\alpha_0)}_{\pi\pi}\widehat{(\alpha_{\underline{2}i})}_{\pi\pi}|f\rangle = -\partial_0 B_{fi}(x), \\ (\vec{\nabla}\times\vec{B}_f(x))_i &= -\langle\phi(x)|\frac{1}{2i}\varepsilon_{ijk}\widehat{(\alpha_{\underline{3}j})}_{\pi\pi}\widehat{(\alpha_{\underline{2}k})}_{\pi\pi}|f\rangle = \langle\phi(x)|\frac{1}{2i}\widehat{(\alpha_0)}_{\pi\pi}\widehat{(\alpha_{\underline{1}i})}_{\pi\pi}|f\rangle = \partial_0 E_{fi}(x). \end{aligned} \tag{26}$$

---

[7] It is true that so defined E_{fi} and B_{fi} functions can take complex values, which is not a property of standard electric and magnetic fields. However, this is hardly avoidable in one first quantization approach like this, where E and B functions are understood to play role of a photon wave function (the idea that physical E and B fields instead of potential A_μ should be related to photon wave function is usually attributed to Majorana [4].

We note that this pair of Maxwell equations can be also obtained starting from the helicity identity (12), the same one from which we derived the Dirac equation. To this end we must first find representation of the $Y_{\underline{3}}$ operator:

$$Y_{\underline{3}}E_{fi}(x) \equiv \langle E_i(x)|Y_{\underline{3}}|f\rangle = iB_{fi}(x), \qquad Y_{\underline{3}}B_{fi}(x) \equiv \langle B_i(x)|Y_{\underline{3}}|f\rangle = -iE_{fi}(x). \tag{27}$$

Now, in a similar manner as we derived Dirac equation, we find:

$$\langle E_i(x)|P_jJ_j|f\rangle = -\langle E_i(x)|P_0Y_{\underline{3}}|f\rangle \Rightarrow (s_j)_{ik}\partial_jE_{fk} = -\partial_0B_{fi} \Rightarrow \varepsilon_{ijk}\partial_jE_{fk} = -\partial_0B_{fi},$$

$$\langle B_i(x)|P_jJ_j|f\rangle = -\langle B_i(x)|P_0Y_{\underline{3}}|f\rangle \Rightarrow (s_j)_{ik}\partial_jB_{fk} = \partial_0E_{fi} \Rightarrow \varepsilon_{ijk}\partial_jB_{fk} = \partial_0E_{fi}. \tag{28}$$

Summation over repeated indices is implied and the matrices s_j are matrices generating rotations in three-dimensional vector representation of rotation group. Matrix notation of intermediate result in (28) is the essence of what is sometimes called fermion-like formulation for electromagnetic field [4]. (One can draw closer parallels to Majorana's original fermion-like formulation by expressing these results in terms of linear combinations $E_{fi}(x) \pm iB_{fi}(x)$ of definite helicity.)

Finally, the two remaining Maxwell equations can be derived from mathematical identity (11) by taking consecutively $\underline{j} = 3, \underline{k} = 1$ and $\underline{j} = 3, \underline{k} = 2$:

$$\vec{\nabla}\vec{E}_f(x) = \langle\phi(x)|\ \frac{1}{2i}\left(\widehat{(\alpha_{\underline{3}1})}_{\pi\pi}\widehat{(\alpha_{\underline{1}1})}_{\pi\pi} + \widehat{(\alpha_{\underline{3}2})}_{\pi\pi}\widehat{(\alpha_{\underline{1}2})}_{\pi\pi} + \widehat{(\alpha_{\underline{3}3})}_{\pi\pi}\widehat{(\alpha_{\underline{1}3})}_{\pi\pi}\right)|f\rangle = 0,$$

$$\vec{\nabla}\vec{B}_f(x) = \langle\phi(x)|\ \frac{i}{2}\left(\widehat{(\alpha_{\underline{3}1})}_{\pi\pi}\widehat{(\alpha_{\underline{2}1})}_{\pi\pi} + \widehat{(\alpha_{\underline{3}2})}_{\pi\pi}\widehat{(\alpha_{\underline{2}2})}_{\pi\pi} + \widehat{(\alpha_{\underline{3}3})}_{\pi\pi}\widehat{(\alpha_{\underline{2}3})}_{\pi\pi}\right)|f\rangle = 0. \tag{29}$$

Following the same idea to raise helicity by the action of π_α operators, we define a field vector of helicity h that has spin projection on the third axis equal to s as:

$$|F_{h,s}(x)\rangle = (u_{\frac{1}{2}})^{h+s}(u_{-\frac{1}{2}})^{h-s}|\phi(x)\rangle, \tag{30}$$

for $h \geq 0$ and

$$|F_{h,s}(x)\rangle = (v_{\frac{1}{2}})^{|h|+s}(v_{-\frac{1}{2}})^{|h|-s}|\phi(x)\rangle, \tag{31}$$

for $h < 0$, where $u_{\pm\frac{1}{2}}$ and $v_{\pm\frac{1}{2}}$ are such linear combinations of π_α operators that respectively raise and lower the $Y_{\underline{3}}$ eigenvalue for $\frac{1}{2}$ while changing the J_3 value for the amount given in the index. Additionally, it must be satisfied $-|h| \leq s \leq |h|$ and h and s being both integers or both half-odd integers.

The field representation of helicity h of a state $|f\rangle$ is then a set of functions:[8]

$$F^{(h)}_{fs}(x) = \langle F_{h,s}(x)|f\rangle, \qquad\qquad s = -|h|, -|h|+1, \ldots, |h|. \tag{32}$$

By the same reasoning as in the scalar case we can verify that for any given helicity the corresponding field representation function satisfies Klein-Gordon equation of motion. Besides, starting from the helicity equation (12) we can derive generalization of the Dirac massless equation:

$$\left(ih\delta^{s'}_s\partial_0 + i(\Sigma^{(h)}_i)^{s'}_s\partial_i\right)F^{(h)}_{fs'}(x) = 0 \tag{33}$$

---

[8] These generic definitions differ from definitions we already have for the helicity $\pm\frac{1}{2}$ and helicity ± 1 fields (18, 19, 24, 25), but it is just a matter of choice of the basis.

Here $\Sigma_i^{(h)}$ denotes $(2h+1)$-dimensional representation matrix of spin around the ith axis.[9]

However, the Klein-Gordon and the generic equation (33) do not exhaust all the possible motion equations satisfied by these fields (for example, the first two Maxwell equations (29) are not of this type).

Where do equations (17, 23, 29, 26, 33) actually come from? They are obviously already contained in the form of algebra (3, 7) and then, depending on the type of "field representation", a concrete form of equation appears. In other words, equations of motion are here completely determined by the symmetry of the model (there are even no free parameters such as mass in the case of pure Poincare symmetry). Of course, it is not a novelty to derive free equations of motion directly from the symmetry requirements, although such derivations are not as straightforward as these delivered here. Derivations of equations (17, 23, 29, 26) based on symmetry arguments can be found, for example, in [5].

Nevertheless, it is much more common to derive dynamics of a theory starting from a Lagrangian, using the least action principle. Standard Lagrangian density that would produce equations (17, 23, 29, 26) would be:

$$\mathcal{L} = \frac{1}{2}\partial_\mu\phi\ \partial^\mu\phi + \overline{\psi}\ i\gamma^\mu\partial_\mu\psi + \frac{1}{4}F_{\mu\nu}F^{\mu\nu}. \tag{34}$$

So, it counts three nontrivial terms and this number would grow to infinity if all equations from the class (33) are included. Though all of the terms in this lagrangian are to a large extent determined by symmetry requirements, the deeper symmetry that allowed us to automatically obtain equations of motion is hidden in (34). Therefore, examples like this are good to remind us that the Lagrangian formalism is not the only way to obtain dynamics and that it does not have to be always the most appropriate one.

5. Conclusion

The conformal generators were expressed in this paper as quadratic functions of operators satisfying Heisenberg algebra. As a consequence of this, free equations of motion followed from a number of mathematical identities that connect operators of the quadratic algebra (2). In such a model where the dynamics is already contained in algebra, we pointed out that Lagrangian formalism appears as a comparably very complex way to derive equations of motion. Existence of such a model casts a doubt on whether the Lagrangian method is really always the appropriate one.

Acknowledgments

The author wants to thank to Prof. Djordje Šijački for numerous suggestions and helpful comments. The work was supported in part by the Serbian Ministry of Science and Environmental Protection, under contract No. 141036.

---

[9] By deriving this general equation, as well as its particular cases (23) and (28), from the helicity identity, we most clearly demonstrated that these equations are essentially just a helicity eigenvalue problems.

References

1. I. Salom, "Algebraic Approach to the Duality Symmetry", http://arxiv.org/abs/hep-th/0602282.
2. Yu. F. Pirogov, "Space-time Revisited", 13th Intern. Seminar on High Energy Physics "Quarks-2004", Pushkinskie Gory, Russia (2004), http://arxiv.org/abs/gr-qc/0409067.
3. D. Bailin, A. Love, Rep. Prog. Phys. **50**, 1087 (1987); L. O'Raifeartaigh, N. Straumann, "Early History of Gauge Theories and Kaluza-Klein Theories, with a Glance at Recent Developments", http://arxiv.org/abs/hep-ph/9810524.
4. E. Majorana, Nuovo Cim. **9**, 335 (1932); Nuovo Cim. **14**, 171 (1937); E. Majorana, Scientific Manuscripts (1928-1932), edited by R. Mignani, E. Recami; M. Baldo, Lett. Nuovo Cim. **11**, 568 (1974).
5. J. P. Elliott, P. G. Dawber, *Symmetry in Physics*, (The Macmillan Press LTD, London and Basingstoke, 1979).

Journal of Research in Physics Vol. 31, No. 1, 11 - 18 (2007)

Stark Broadening Measurements of Low-intensity Xe II Lines in Pulsed Discharge

M. Ćirišan[1], R. J. Peláez[2], S. Djurović[1], J. A. Aparicio[2] and S. Mar[2]
[1] *Department of Physics, Faculty of Sciences, Trg Dositeja Obradovića 4,*
21000 Novi Sad, Serbia
[2] *Departamento de Fisica Teórica, Atómica y Óptica, Facultad de Ciencias,*
Universidad de Valladolid, 47071 Valladolid, Spain
e-mail: djurovic@uns.ns.ac.yu

Received: *July 3, 2006*

Abstract

The results of Stark parameters measurements for low-intensity Xe II spectral lines are presented. All Stark parameters were measured in a pulsed arc plasma. Most of the presented results are quite new in the literature and they can increase the present database of measured Stark parameters. Some of presented data are compared with available theoretical and experimental results. The spectroscopic measurements of noble gases are always of a great interest.

Key words: Plasma, spectral line, Stark broadening

1. Introduction

Stark broadening of Xe II spectral lines has been the subject of many experimental ([1-3] and references therein) and theoretical [4, 5] studies. Investigation of ionized xenon spectra is always of interest for many areas, such as laser physics, fusion diagnostics, collision physics, astrophysics, etc.

The aim of this work was to measure the Stark parameters of low-intensity Xe II lines. Here, the results of 25 Stark width and 5 shift measurements for Xe II spectral lines are reported. Results for 19 widths and 4 shifts are for the first time presented in this paper. Seven of these lines belong to $5d-4f$, six to $5d-6p$, four to $6s-6p$, five to $6p-6d$, and three to $6p-7s$ transitions.

In this experiment, pulsed arc plasma, mixture of 95 % helium and 5 % xenon, was used. Measured electron densities and temperatures were in the range of $(0.2-1.8)\cdot 10^{23}$ m^{-3} and $18300-25500$ K respectively. These results are important for plasma diagnostic purposes and for astrophysical applications.

In obtaining Stark widths, special attention was paid to the experimental and data treatment procedures. Other broadening mechanisms have also been taken into account.

2. Experimental details

Experimental apparatus and diagnostic methods are described elsewhere [6-8]. Here we give only a short description.

Excitation unit contained a capacitor bank of 20 μF, charged up to 9.2 kV approximately. The mixture of helium (95 %) and xenon (5 %) at a pressure of 3 kPa continuously flowed through the discharge lamp. Under these conditions plasma emission lasted for about 200 μs.

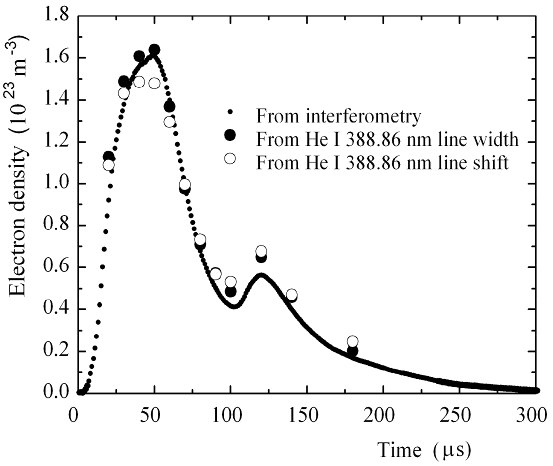

Figure 1. Results of electron density measurements by interferometry and Stark shift and width of the He I 388.86 nm line.

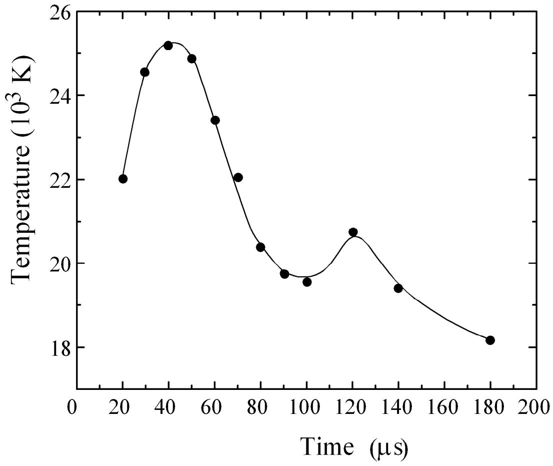

Figure 2. Temporal evolution of the electron temperature.

The lamp was a cylindrical tube of Pyrex glass, 175 mm in length and 19 mm in internal diameter. Used percentage of xenon (5 %) in the mixture was low enough to obtain minimal self-absorption, but still high enough to get maximal spectral line intensity.

Electron density was in the range $(0.2-1.8)\cdot 10^{23}$ m^{-3}. Two different techniques were used to obtain electron density: the spectroscopic method, using He I 388.86 nm line, and the interferometric method. Stark width and shift parameters of He I 388.86 nm line were measured, and Griems theoretical model [9] was used to obtain the electron densities. Two-wavelength interferometric method was also used for electron density determination. This is the way to avoid other particles influence on the change of refractivity index and electron density determination [10, 11]. These two methods were used only for comparison. The differences between spectroscopic and interferometric measurements were lower than 15 %. Electron density data obtained by the interferometric method, with an uncertainty of about 10 %, were used in this work. Results of the two measurements are shown in Fig. 1.

Electron temperature was determined by a Botzmann-plot of 24 Xe II lines and it was in the range (18300 − 25500 K). Estimated errors are lower than 15 %. Results of electron temperature measurements are shown in Fig. 2.

3. Experimental data treatment

The experimental data treatment is explained in detail in our previous work [8]. Here, only short description will be given.

Spectra were recorded using a spectrometer equipped with an optical multichannel analyzer OMA detector with 512 channels. Exposure times were usually 5 μs. The spectral measurements were taken in the first order of diffraction. The instrumental function was estimated by introducing a laser beam (632.85 nm) into the entrance slit of the spectrometer. Halfwidth of this line was approximately 3 channels (18 pm) and it has been taken into account as instrumental broadening.

For each observed instant of plasma life, five spectra of the same region were recorded. Another five spectra were recorded using a mirror, placed behind the plasma tube. Results of both recordings were averaged. Comparison of these two averaged spectra was used for self-absorption checking, which showed that there was no self-absorption at the observed lines. Self-absorption effect was avoided thanks to the low percentage of xenon in the plasma and low intensity of spectral lines.

An incandescent calibrated lamp and a deuterium lamp were used to obtain the spectrometer transmittance for the wavelength range $300 - 650$ nm and for all OMA channels. All spectra were divided by this transmittance curve, whose uncertainty was estimated to be lower than 4 %.

The recorded spectra were fitted to sums of asymmetrical Lorentzian functions which represent the spectral profiles and a linear function which represent the emission from continuum [7]. An example of a part of Xe II spectrum and its fit is shown in Fig. 3. Wavelengths were taken from reference [12].

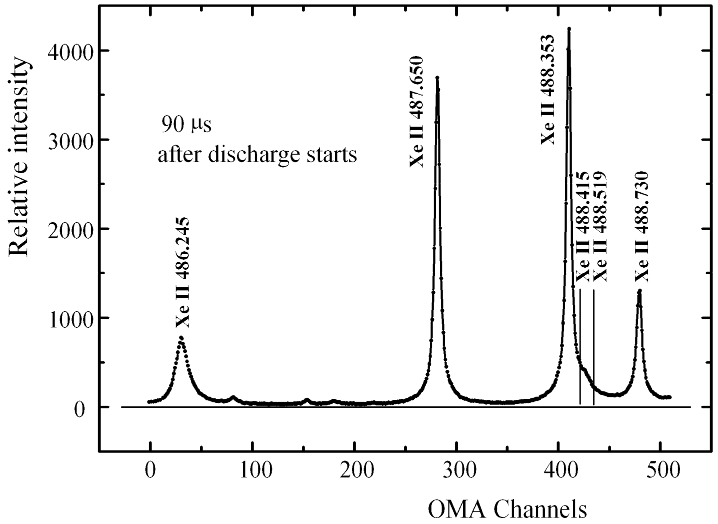

Figure 3. Example of a part of Xe II experimental spectrum and its fit.

To obtain Stark halfwidth from experimental halfwidth, appropriate deconvolution procedure was used, taking into account other broadening mechanisms. Doppler width was small, lower than 7 pm, due to the great weight of the emitter atom. On the other hand, van der Waals broadening was about 0.43 pm at $T = 20000$ K [13 Eq (4.113)]. Ionic broadening was always lower than 1 pm [13 Eq (4.104)] and resonance broadening was about 0.2 pm [9 Eq (218b)]. It is obvious that van der Waals and resonance broadening were negligibly small for plasma conditions in this experiment, and these mechanisms were not considered in the final calculations. In the deconvolution procedure [14] total Gaussian width component (Instrumental + Doppler) and Stark width component were taken into account.

4. Results and discussion

Results of Stark width measurements are organized in two groups. In the first group are results concerning the lines from visible region ($410 - 650$ nm). These results are given in Table 1.

Table 1. Experimental Stark halfwidths of some Xe II lines; w_m - this work ($T_e = 22000$ K). Calculated Stark halfwidths [16] are denoted with w_{calc}. Halfwidths from other authors, w_{moa}, are given with their temperatures. All data are normalized to electron density of 10^{23} m^{-3}.

Configuration	Wavelength (nm)	w_m (pm)	w_{calc} [16] (pm)	w_{moa} (pm)	[Ref]	T_e (K)
$5p^4\ (^3\mathrm{P}_2)\ 5d\ [2] - 5p^4\ (^3\mathrm{P}_2)\ 6p\ [1]^\circ$	467.456	43.29 C				
$5p^4\ (^3\mathrm{P}_1)\ 5d\ [1] - 5p^4\ (^3\mathrm{P}_1)\ 6p\ [2]^\circ$	651.283	98.41 A				
$5p^4\ (^3\mathrm{P}_2)\ 5d\ [0] - 5p^4\ (^3\mathrm{P}_1)\ 6p\ [1]^\circ$	536.807	57.21 B		47.85	[17]	14500
				102.7	[7]	10000
$5p^4\ (^3\mathrm{P}_0)\ 5d\ [2] - 5p^4\ (^1\mathrm{D}_2)\ 6p\ [3]^\circ$	453.249	37.27 C		55	[18]	11000
$5p^4\ (^3\mathrm{P}_0)\ 5d\ [2] - 5p^4\ (^1\mathrm{D}_2)\ 6p\ [2]^\circ$	413.101	30.90 A				
$5p^4\ (^1\mathrm{D}_2)\ 6s\ [2] - 5p^4\ (^1\mathrm{D}_2)\ 6p\ [1]^\circ$	504.492	67.51 A	48.28	63.39	[17]	14500
				64	[19]	20600
	597.113	65.60 A	45.49			
$5p^4\ (^3\mathrm{P}_2)\ 6p\ [1]^\circ - 5p^4\ (^3\mathrm{P}_2)\ 6d\ [1]$	437.378	193.93 A				
$5p^4\ (^1\mathrm{D}_2)\ 5d\ [3] - 5p^4\ (^3\mathrm{P}_2)\ 4f\ [4]^\circ$	477.319	121.81 C				
$5p^4\ (^3\mathrm{P}_0)\ 6p\ [1]^\circ - 5p^4\ (^3\mathrm{P}_1)\ 6d\ [2]$	411.214	135.82 B				
$5p^4\ (^3\mathrm{P}_1)\ 6p\ [0]^\circ - 5p^4\ (^3\mathrm{P}_1)\ 7s\ [1]$	471.518	185.31 B				
$5p^4\ (^3\mathrm{P}_1)\ 6p\ [2]^\circ - 5p^4\ (^3\mathrm{P}_1)\ 6d\ [3]$	444.813	146.23 A		132	[18]	11000
$5p^4\ (^3\mathrm{P}_1)\ 6p\ [2]^\circ - 5p^4\ (^3\mathrm{P}_1)\ 6d\ [2]$	440.688	136.41 B		147.77	[20]	23000
$5p^4\ (^3\mathrm{P}_1)\ 6p\ [1]^\circ - 5p^4\ (^3\mathrm{P}_1)\ 7s\ [1]$	544.545	122.75 A				
$5p^4\ (^1\mathrm{D}_2)\ 6p\ [1]^\circ - 5p^4\ (^1\mathrm{D}_2)\ 7s\ [2]$	499.117	214.13 B		256	[7]	10000

The line transitions are arranged in the same way as it was done in NIST atomic spectra database [15]. In the first two columns, configurations and wavelengths of the lines are given. Next two columns present measured Stark halfwidths, and comparison with calculations based on modified semiclasical formula [16]. All measured data given in Table 1 correspond to the temperature of 22000 K and are normalized to $N_e = 10^{23}$ m^{-3}. Estimated errors for width measurements are classified as A (25 %), B (< 40 %) and C (> 40 %). The high percentage errors are the result of lines having low intensity and, in some cases, even overlapping with more intensive neighbor lines.

Semiempirical calculations were performed for two lines from the multiplet (^{1}D$_2$) $6s$ [2]–(^{1}D$_2$) $6p$ [1]° because a complete set of perturbing levels exists only for these two lines. For semiempirical calculations jK-coupling scheme was used. The ratio between measured and calculated widths is $w_m/w_{calc} \approx 1.4$.

Stark width of Xe II 504.492 nm line as a function of electron density is plotted, as an example, in Fig. 4. It is obvious that there is a clear linear trend.

The results of other authors are given in the last column along with their corresponding temperatures for electron density of $N_e = 10^{23}$ m^{-3}. An example of comparison of experimental data, calculated data and the data of other authors is shown in Fig. 5.

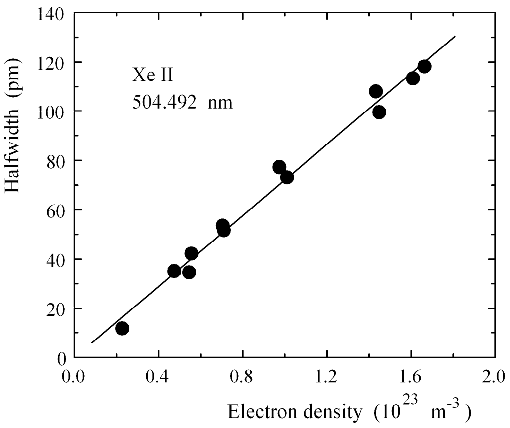

Figure 4. Example of Xe II 504.492 nm line halfwidth vs. electron density.

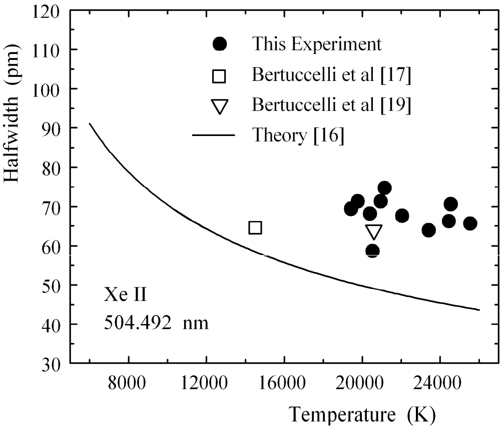

Figure 5. Stark halfwidth of Xe II 504.492 nm line as a function of temperature.

Comparison of our experimental data with those of other authors show approximately good agreement (see Table 1). However, small number of existing experimental data do not allow us to make any general conclusion. The same situation is with the comparison between theoretical and experimental data and the halfwidth temperature dependence.

Second group of the Xe II Stark width results for the lines from UV spectral region is given in Table 2. The table is organized in the same way as Table 1. For these lines no other experimental data are available in the literature.

Table 2. Experimental Stark halfwidths of some UV Xe II lines; w_m - this work. Calculated Stark halfwidths [16] are denoted with w_{calc}. Data are normalized to $N_e = 10^{23}$ cm^{-3} and $T = 22000$ K.

Configuration	Wavelength (nm)	w_m (pm)	w_{calc} (pm)
$5p^4$ (^{3}P$_2$) $6s$ [2] – $5p^4$ (^{3}P$_1$) $6p$ [2]°	332.746	22.08 A	18.75
	356.430	28.13 B	21.33
$5p^4$ (^{3}P$_2$) $5d$ [0] – $5p^4$ (^{1}D$_2$) $6p$ [2]°	384.858	23.68 B	
$5p^4$ (^{3}P$_0$) $5d$ [2] – $5p^4$ (^{3}P$_2$) $4f$ [2]°	310.440	59.71 B	
	311.274	56.50 A	
$5p^4$ (^{3}P$_1$) $5d$ [2] – $5p^4$ (^{3}P$_2$) $4f$ [2]°	346.126	85.49 A	
$5p^4$ (^{3}P$_2$) $6p$ [1]° – $5p^4$ (^{3}P$_2$) $6d$ [1]	384.987	164.69 A	
$5p^4$ (^{1}D$_2$) $5d$ [1] – $5p^4$ (^{1}D$_2$) $4f$ [2]°	310.151	67.84 B	
$5p^4$ (^{1}D$_2$) $5d$ [2] – $5p^4$ (^{3}P$_1$) $4f$ [4]°	400.235	168.13 C	
$5p^4$ (^{1}D$_2$) $5d$ [2] – $5p^4$ (^{3}P$_1$) $4f$ [3]°	393.892	150.75 A	

Semiempirical calculations were performed for two lines from the multiplet (^{3}P$_2$) $6s$ [2]–(^{3}P$_1$) $6p$ [2]° because a complete set of perturbing levels exists only for these two lines. For semiempirical calculations jK-coupling scheme was used as well as in previous case. The ratio between measured and calculated widths is $w_m/w_{calc} \approx 1.2$ for 332.746 nm line and 1.3 for 356.430 nm line.

Stark width of Xe II 310.440 nm line as a function of electron density is plotted, as an example, in Fig. 6. The linear trend is obtained again. An example of comparison of the experimental and calculated data [16] for 332.746 nm line is shown in Fig. 7.

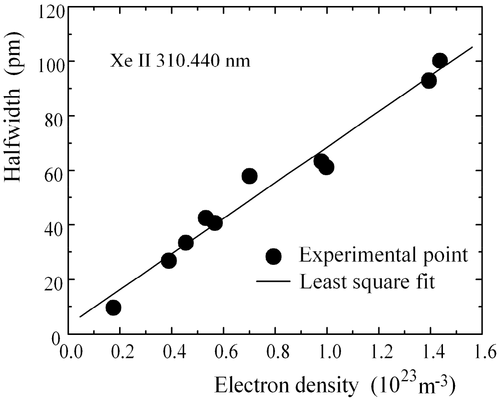

Figure 6. Example of Xe II 310.440 nm halfwidth vs. electron density.

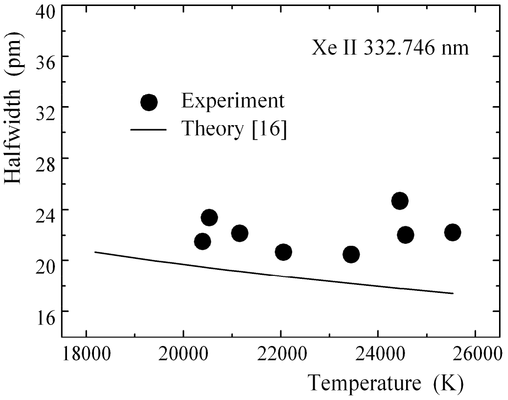

Figure 7. Stark halfwidth of Xe II 332.746 nm line as a function of temperature.

The measured Stark shifts are shown in Table 3, which is organized in the same way as Table 1. Estimated errors for shift measurements are about 16 %.

Table 3. Experimental Stark shifts of Xe II lines; d_m - this work. Calculated Stark shifts [16] are denoted with d_{calc}, and Stark shifts measured by other authors with d_{moa}. Data are normalized to $N_e = 10^{23}$ cm^{-3} and $T = 22000$ K.

Configuration	Wavelength (nm)	d_m (pm)	d_{calc} (pm)	d_{moa} (pm)
$5p^4$ (^{3}P$_0$) $6s$ [0] – $5p^4$ (^{3}P$_1$) $6p$ [1]°	426.984	-5.42	-8.54	
$5p^4$ (^{3}P$_2$) $6s$ [2] – $5p^4$ (^{3}P$_1$) $6p$ [2]°	332.746	-3.20	-5.18	
	356.430	-3.95	-6.95	
$5p^4$ (^{3}P$_2$) $6p$ [2]° – $5p^4$ (^{3}P$_2$) $7s$ [2]	482.335	57.52	38.72	
	486.245	55.15	39.28	57 [7]

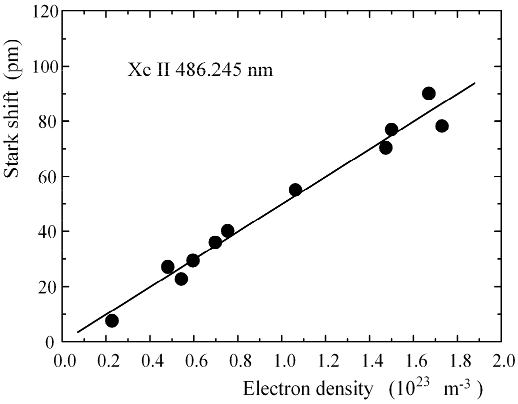

Figure 8. Example of Xe II 486.245 nm line halfwidth vs. electron density and its linear fit.

Semiempirical calculations were performed using the jK-coupling scheme. The ratio of the measured and calculated shift values for $6s - 6p$ transitions is $d_m/d_{calc} \approx 0.6$, while for $6p - 7s$ transition is $d_m/d_{calc} \approx 1.4$. Only one experimental result from other authors [7] was found - for Xe II 486.245 nm line, and it is given in the last column. The agreement of this and our experimental result is very good.

Stark shift of Xe II 486.245 nm line as a function of electron density is plotted, as example, in Fig. 8. Linear trend shows consistency of the results and a good quality of measurements.

5. Conclusion

Radiation from a low-pressure pulsed arc plasma has been studied in order to determine Stark parameters of some singly ionized xenon lines. In this work, only low intensity lines were considered. Twenty five Xe II spectral lines were considered for Stark width measurements and five for shift measurements in a wide spectral region (310 – 650 nm). The data for these lines are mostly missing in the literature.

These data can be used for diagnostic purposes, for demonstration of regularities and similarities of the line widths inside of multiplets or transition arrays, for theory testing, and they can also be of interest in astrophysics.

Acknowledgments

We gratefully thank S. González for his collaboration in the experimental arrangement, and the Spanish Dirección General de Investigación Cientfica y Técnica (Ministerio de Educación y Ciencia) and the Consejeria de Educación y Cultura de Castilla y León for their financial support under contract nos. FIS2005-03155 and VA015A05. S. Djurović and M. Ćirišan thank to the Ministry of Science and Environmental Protection of the Republic of Serbia for partial support (141024). Dr J. A. Aparicio would like to express his personal acknowledgement to the Organización Nacional de Ciegos de España (ONCE) for its help.

References

1. N. Konjević, M. S. Dimitrijević and W. L. Wiese, J. Phys. Chem. Data **13**, 649 (1984).
2. N. Konjević and W. L. Wiese, J. Phys. Chem. Data **19**, 1307 (1990).
3. N. Konjević, A. Lesage, J. R. Fuhr and W. L. Wiese, J. Phys. Chem. Data **31**, 819 (2002).
4. L. Č. Popović and M. S. Dimitrijević, Astron. Astrophys. Suppl. Ser. **116**, 359 (1996).
5. H. O. Di Rocco, Nuovo Cimento D **12**, 1485 (1990).
6. J. A. del Val, S. Mar, M. A. Gigosos, I. de la Rosa, C. Perez and V. Gonzales, Jpn. J. Phys. **37**, 4177 (1998).
7. M. A. Gigosos, S. Mar, C. Perez and M. I. de la Rosa, Phys. Rev. E **49**, 1575 (1994).
8. S. Djurović, R. J. Peláez, M. Ćirišan, J. A. Aparicio and S. Mar, J. Phys. B: At. Mol. Opt. Phys. **39**, 2901 (2006).
9. H. R. Griem, *Spectral line broadening by plasmas*, (Academic Press, New York, 1974).
10. J. A. Aparicio, M. A. Gigosos, V. R. González, C. Pérez, M. I. de la Rosa and S. Mar, J. Phys. B **31**, 1029 (1998).
11. M. I. de la Rosa, C. Pérez, A. M. de Frutos and S. Mar, Phys. Rev. A **42**, 7389 (1990).

12. A. R. Striganov and N. S. Sventiskii, "Tables of Spectral Lines of Neutral and Ionized Atoms", New York Plenum, (1968).

13. H. R. Griem, *Plasma spectroscopy*, (Academic Press, New York 1964).

14. J. T. Davies and J. M. Vaughan, Astrophys. J. **137**, 1302 (1963).

15. NIST Atomic spectra database, http://physics.nist.gov./asd.

16. M. S. Dimitrijević and N. Konjević, J. Quant. Spectrosc. Radiat. Transfer **24**, 451 (1980).

17. D. Bertuccelli, G. Bertuccelli and H. O. Di Rocco, Physica Scripta **43**, 469 (1991).

18. A. Lesage, D. Abadie and M. H. Miller, Phys. Rev. A **40**, 1367 (1989).

19. D. Bertuccelli, G. Bertuccelli and H. O. Di Rocco, Rev. Sci. Instrum. **62**, 966 (1991).

20. T. L. Pitman and N. Konjević, J. Quant. Spectrosc. Radiat. Transfer **35**, 247 (1986).

Journal of Research in Physics Vol. 31, No. 1, 19 - 30 (2007)

Evaluation of Efficiency Calibration Methods of Semiconductor Gamma Spectrometers

J. Slivka, I. Bikit, M. Vesković, M. Krmar, N. Todorović, D. Mrdja, S. Forkapić
Department of Physics, Faculty of Sciences, Trg Dositeja Obradovića 4,
21000 Novi Sad, Serbia
e-mail: slivka@im.ns.ac.yu

Received: *February 2, 2007*

Abstract

A number of different calibration sources were used to establish the efficiency of three semiconductor gamma spectrometers employed to measure low-level activity concentrations in voluminous environmental samples. The advantages and drawbacks of these methods involving the calculation of effective solid angle ratio are discussed. The obtained efficiency curves were verified on samples distributed within the IAEA-CU-2006-03 World-wide open proficiency test on the determination of gamma emitting radionuclides.

Key words: Gamma spectrometry, environmental samples, efficiency calibration, effective solid angle.

1. Introduction

The main problem of gamma spectrometry applied in environmental radioactivity monitoring is the necessity to measure the activity concentration using samples with large mass/volume in order to obtain the satisfactory resulting precision, yet within reasonably long measurement times. The variety of environmental samples size requires at least several types of sample holders. This means that for every detector it is necessary to perform the detection efficiency calibration for a number of different geometries. The situation becomes even more complex because the detection efficiency for a given geometry also depends on the sample properties, e. g. on its density and elemental composition.

The energy range of gamma- and X-rays emitted by natural and man-made radionuclides which are the object of analysis in environmental radioactivity monitoring usually is taken to be from 30 keV to 3000 keV. Hence, the detection efficiency calibration for a given sample type (of a given density and elemental composition) is actually the procedure of establishing a continuous efficiency curve in the mentioned energy range. Here, under the term "efficiency", the full energy peak efficiency is assumed. In special cases, when the activity concentration of a single nuclide is being determined, the complete efficiency curve is not required; instead the efficiency value at a single energy or at few energies satisfies, but we will not discuss these cases here.

There are a number of procedures for detection efficiency determination [3], which usually must be combined. The purely experimental approach is, in principle, the most reliable one; it is based on the measured spectrum of a calibration source emitting gamma rays in the energy range of interest. The known activities A of the radionuclides in the source enable the determination of detection efficiency ε at the energies present in their spectra through the relation

$$\varepsilon = \frac{R}{A\, p_\gamma},$$

where R is the measured net count rate under the full energy peak, and p_γ the relative yield of gamma rays of the given energy. The measurement uncertainty of this data $s(\varepsilon)$ can be reduced to the combination of uncertainties $s(A)$, which has the order of magnitude of a few percents for quality sources commercially available, and $s(p_\gamma)$, which is almost negligible for strong gamma lines, but also reaching a few percents for the weaker ones. The energy range from 30 keV to 3000 keV must be, as evenly as possible, covered by lines from the spectrum of such a source. On the other hand, it is desirable for the radionuclides to emit monoenergetic gamma rays, otherwise quite commonly coincidence summing occurs when gamma rays from cascade transitions leave simultaneously their energy in the detector. There is not a plenty of radionuclides commercially available with monoenergetic transitions and with long enough half-lives, hence, radionuclides with several energies in their spectra are used quite commonly. However, then mathematical corrections for coincidence summing are needed, which introduce an additional component to the uncertainty of the efficiency curve [10].

Two types of calibration sources are in common use: sealed sources with fixed shape and given activity, and standard radioactive materials with given specific activity. It would be ideal for the experimental detection efficiency calibration to dispose of calibration sources in shapes and with compositions corresponding to the sample sources the activities of which will be determined from the efficiency curve. Although it is possible to make calibration sources of various shapes from radioactive materials, it is practically impossible to always satisfy the requirement of equal sample and calibration source density and composition. Because of that, the purely experimental detection efficiency calibration is usually not feasible for a wide class of variable sources - at least some mathematical corrections have to be introduced.

A completely opposite approach to detection efficiency determination is the purely computational one. The full energy peak efficiency depends on gamma ray energy and on detector parameters in a complex manner, which cannot be described analytically. The most prospective approach to calculate the detection efficiency is by the Monte Carlo method based on simulation of the history of individual photons. Every photon is followed on its path from the emission at a point of the source, through the source to the detector, and within the detector. The photon interacts through photoelectric absorption, Compton scattering, or pair production, and electrons, positrons, and secondary photons are produced, which are also followed through the detector. To obtain the total result of interactions, at each point the probability of every interaction type at every possible scattering angle is used. If a particle leaves the detector, the tracking is stopped. The input information needed for the Monte Carlo procedure is as follows:

- the dimensions of the source and the distance to the detector,

- the dimensions of the detector end cap and of the sensitive and insensitive zones of the detector,
- the elemental composition and the density of all materials which the photons are passing through,
- the photon attenuation coefficients for all these materials,

and in more detail:

- the probabilities for all relevant photon interactions in the detector material as a function of energy and scattering angle,
- the information on the transport of electrons and positrons through the detector material.

The results of modern Monte Carlo computations give detection efficiencies with uncertainties comparable to the ones from experimental calibrations subject to various required mathematical corrections [4], [8]. The prerequisite for a successful Monte Carlo simulation is the exact knowledge of the dimensions of the detector crystal, which are usually given by the supplier, but also the exact knowledge of the parts around the crystal, as well as the distribution of the sensitive and insensitive zones, which often remains uncertain to the user. A detector with these parameters verified in detail can be ordered, but usually it is then much more expensive.

While for the purely computational determination of the detection efficiency the complex Monte Carlo method is unavoidable, there are simpler methods which allow the conversion of the detection efficiency measured with a calibration source of a given geometry and composition to the detection efficiency of a different geometry and composition on the given detector [9], [1]. These methods usually still require the first four of the above quoted items, but the accuracy of the data is of less concern, because the errors resulting from these relative recalculations are canceled to some extent. The most commonly used of these methods are based on the calculation of effective solid angles for samples of various geometry and composition. The first of these methods was developed by [7] for coaxial detectors and cylindrical samples, and in [6] it was extended to cylindrical samples with diameters larger than the detector crystal diameter. This method was experimentally tested for point, disk, and cylindrical sources at different distances on a number of detectors and an agreement of experimental and recalculated values within 3 % was obtained when the detector parameters were well known. A user-oriented program for personal computers, Angle, based on these methods, is presented in [5].

As one can see from this introduction, the laboratory practice of gamma spectrometry applied to environmental samples basically prefers the experimental detection efficiency calibration, but which must be subject to a number of computational corrections in order to be used for samples of different geometry and composition. The direct experimental calibration by itself, together with all consequential corrections, introduce a number of uncertainties into the final result, hence the analysis of possible deviations is of crucial importance for this branch of gamma spectrometry.

In this work, the results of efficiency calibration and the advantages and drawbacks of the method are discussed in case of using the three spectrometers at the Laboratory of Radioactivity and Dose Measurement at the Department of Physics, Faculty of Science, Novi Sad. Sources of radioactive materials of known activity concentration, certified and laboratory made, as well as a number of certified sealed radioactive sources, were used for basic experimental calibration. The above mentioned program Angle was used to recalculate the detection efficiency for samples of other dimensions and composition. The activity concentration of samples of soil, grass, and water, distributed within the IAEA-CU-2006-03 World-wide open proficiency test on the determination of gamma emitting radionuclides were measured on thus calibrated detectors. The Agency sends the actual activity concentration values to the participant only upon the arrival of participant's laboratory results, which stimulates critical reassessments of calibration procedures and spectra processing. Taking part in such tests and evaluation of the results is a mandatory action in the permanent enhancement of the Laboratory Rules of Quality according to JUS ISO IEC 17025:2001.

2. Experimental details

Detectors

The properties of the three detectors used in this evaluation are summarized in Table 1. Numbers designated with asterisks are only estimates, not given by the supplier.

Table 1. Properties of the detectors.

Code	K	L	M
Product of	Canberra	EG&G ORTEC	Canberra
Type	Closed end coaxial, p-type	Closed end coaxial, n-type GMX	Closed end coaxial, p-type
Model	GC3518	GMX-20190	GC2520
Cryostat	7935SL-7	LLB-GMX-HJ	7600SL/S
Relative efficiency [%]	35.6	32.4	22.4
Bias voltage [kV]	4.5	- 2.5	4.0
FWHM [keV] @122 keV	0.813		0.882
FWHM [keV] @1332 keV	1.77	1.83	1.76
Peak/Compton	63.2	57	56.4
External contact layer	0.9 mm Ge(Li)	0.3 μm Ge(B)	0.6 mm Ge(Li)
Internal contact layer	0.3 μm Au	0.9 mm Ge(Li)	1 μm Au*
Crystal diameter [mm]	61	56	51
Crystal height [mm]	52	65.2	58.5
Core radius [mm]	4.5	4.6	4.6*
Core height [mm]	34	57.1	38*
Active crystal volume [cm^3]	138.5	155	110*
Entrance window	1.5 mm Al	0.5 mm Be	0.5 mm Al
Distance from window [mm]	5	3.5	5
Detector end cap	1.5 mm Al	1.3 mm Al	1.5 mm Al
Shielding	12 cm Pb	12 cm Pb	25 cm Fe
Background (30 – 3000 keV) [s^{-1}]	3.11	0.98	1.40

Calibration sources

Sources used to calibrate the detection efficiency were of both commercial origin and laboratory made. Properties of radioactive materials used to prepare cylindrical calibration sources are summarized in Table 2. Properties of sources of both kind used for the detection efficiency calibration are summarized in Table 3. The mass attenuation coefficients of SRM and F were measured in the narrow beam geometry with point sources ^{133}Ba, ^{152}Eu, and ^{241}Am to cover the energy range of interest. The XCOM program [2] was used to verify the assumed chemical composition of these materials; the mass attenuation coefficients were found to be compatible with the composition Si 35 %, O 50 %, Al 8 %, and Fe 7 % for SRM and with the formula $Ca_3(PO_4)_2$ for F. The SRM and F calibration sources were prepared and sealed a long time before measurement, this way the Rn equilibrium of the natural radioactive series is reestablished.

Table 2. Radioactive materials used to prepare calibration sources.

Code	SRM	F	KCl
Type	Certified standard reference material SRM 4350B	Radioactive material, activity concentration measured in another laboratory	Pro analysi chemical substance
Origin	NBS, USA	Vinca Institute, Serbia	Merck, Germany
Matrix	River sediment	Phosphate ore	KCl
Main radionuclides	^{40}K, ^{60}Co, ^{137}Cs, ^{152}Eu, ^{241}Am , ^{232}Th series, ^{238}U series	^{238}U series	^{40}K
Approx. activity concentration [Bq/kg]	4 - 560	1500	$16.3 \cdot 10^3$
Reference date	1981.09.09.	-	-

Table 3. Calibration sources.

Code	Origin	Material, density [g/cm^3]	$r \times h$ [cm], V [cm^3]	Main radionuclides	Approx. activity, ref. date
PA	Amersham, UK	-	Point source kit	^{60}Co, ^{133}Ba, ^{137}Cs, ^{241}Am	400 kBq, 1976.06.01.
PF	Framatome, France	-	Point source kit	^{22}Na, ^{51}Cr, ^{54}Mn, ^{57}Co, ^{60}Co, ^{85}Sr, ^{88}Y, ^{137}Cs, ^{152}Eu, ^{241}Am	400 kBq, 2005.02.15.
C7230SRM	Lab made	SRM, 0.950	3.48 × 2.80, 106.4	^{40}K, ^{60}Co, ^{137}Cs, ^{152}Eu, ^{241}Am, ^{232}Th series, ^{238}U series	0.4..56 Bq, 1981.09.09.
C7230×2SRM	Lab made	SRM, 0.947	3.48 × 5.60, 212.8	^{40}K, ^{60}Co, ^{137}Cs, ^{152}Eu, ^{241}Am, ^{232}Th series, ^{238}U series	0.8..112 Bq, 1981.09.09.
C7230F	Lab made	F, 1.527	3.48 × 2.80, 106.4	^{238}U series	250 Bq
C7230×2F	Lab made	F, 1.527	3.48 × 5.60, 212.8	^{238}U series	500 Bq
C7031KCl	Lab made	KCl, 0.923	3.26 × 3.05, 101.6	^{40}K	1.5 kBq
C7230×2KCl	Lab made	KCl, 0.882	3.48 × 5.60, 212.8	^{40}K	3.1 kBq
Bottle	Framatome, France	Resin, 1.15	4.74 × 7.06, 484	^{152}Eu	33.8 kBq, 2005.01.26.
Marinelli	Framatome, France	Resin, 1.15	5.56 × 5.60, 450	^{152}Eu	32.5 kBq, 2005.01.27.

Test samples

The efficiency calibration was checked with samples distributed within the IAEA-CU-2006-03 World-wide open proficiency test on the determination of gamma emitting radionuclides in June 2006. Every participant obtained 200 g of spiked soil, 100 g of grass contaminated with ^{137}Cs, and about 500 ml of spiked water. Cylindrical and Marinelli shaped sources were prepared according to the IAEA instructions. Their properties are presented in Table 4. For soil, the usual composition of O 47 %, Si 35 %, Al 8 %, Fe

3.9 %, C 2.1 %, K 1.3 %, Na 0.6 %, Mg 0.6 %, and N 0.1 % was assumed, compatible with attenuation coefficients of many previously used soil samples. For grass, the elemental formula C_3H_6O was assumed where needed for mass attenuation coefficient calculation.

Table 4. Sources prepared from IAEA test samples.

Code	Material	Geometry, $r \times h$ [cm], V [cm^3]	Density, [g/cm^3]	radionuclides
CF0601	Soil	Cylinder, 3.48 × 2.80, 106.4	1.03	^{54}Mn, ^{60}Co, ^{65}Zn, ^{109}Cd, ^{134}Cs, ^{137}Cs, ^{210}Pb, ^{241}Am
CF0602	Grass	Cylinder, 3.48 × 5.60, 213	0.45	^{40}K, ^{137}Cs
CF0603	Water	Cylinder, 3.22 × 9.91, 299	1.00	^{54}Mn, ^{60}Co, ^{65}Zn, ^{109}Cd, ^{134}Cs, ^{137}Cs, ^{210}Pb, ^{241}Am
MF0603	Water	Marinelli, 5.54 × 8.98, 514	1.00	^{54}Mn, ^{60}Co, ^{65}Zn, ^{109}Cd, ^{134}Cs, ^{137}Cs, ^{210}Pb, ^{241}Am

Measurement procedure

The detector K was connected to the digital spectroscopy processing unit Canberra 1300 InSpector. The other two detectors were connected to conventional gamma spectrometer circuitry with HV units, amplifiers, and ADCs, while the signals were stored in 2 of the 4 inputs of a Canberra Multiport Multichannel Analyzer unit.

The point calibration sources were measured at 25 cm distance from detector entrance windows. The measurement time ranged from 5 ks up to 130 ks in order to get small statistical uncertainties even for gamma lines with smaller p_γ. The highest dead time at this distance was for the ^{152}Eu source, 5 % for the detector K, 7 % for the detector L, and 3 % for the detector M.

The extended volume calibration sources were measured in contact geometry. The measurement time ranged from 70 ks for Bottle and Marinelli, up to 320 ks for C7230SRM. Beacause of a too high count rate and dead time, Bottle and Marinelli were not measured on the L detector. The highest accepted dead time for the K detector was 11 %, produced by the Marinelli calibration source.

The test sources were also measured in contact geometry. The MF0603 sample was measured only on the detector K, while the others were measured on all three detectors. Typical measurement times were about 75 ks. In all cases the dead time was less than 1 %. For all samples, the measurements were repeated at least 3 times, except for the detector L, where only one measurement per sample was performed.

Processing of gamma spectra requires the background count rate to be subtracted from the sample count rate. For all three detectors the background spectra were collected for at least 150 ks up to 320 ks.

After data collection, the samples of soil and grass were dried at 105°C for several hours in order to establish the dry mass. The difference from the initial mass was about 2 % for soil, and about 8 % for grass.

Processing of gamma spectra

The gamma spectra were acquired and analyzed using the Canberra Genie 2000 software. First, the necessary nuclide libraries were constructed using the Nuclide Library

Editor, selecting only the relevant nuclides and transitions, and carefully avoiding possible annoying interferences from non-existent nuclides. This is mostly a trial and error procedure.

The next step was to describe the activities of all the calibration sources, which was quite straightforward using the Certificate File Editor.

The Geometry Composer software component was used to construct files which describe every source-detector combination used in this work. This is needed to derive the peak-to-total efficiencies used for cascade coincidence correction for multiline nuclides. If the detector is not certified by Canberra, as in our case, the software accepts a generic detector only, chosen by the user as the closest to one from the predefined list of detectors, based on the crystal diameter. This arbitrariness is later reflected as the uncertainty of the coincidence corrected line intensities much larger than uncertainties introduced purely by statistics and efficiency. The sources are characterized by their geometry (also relative to the detector), as well as by their elemental composition.

The actual spectra analysis was performed making use of the Gamma Acquisition & Analysis software component (GA&A). The peaks were located using the Unidentified 2nd Difference method, and the peak area was established using the Nonlinear Fit method (Fit singlets was enabled in the Sum / Nonlinear Fit step). Then the peak area was corrected by standard background subtraction using previously processed background spectra.

The calculation of efficiency for calibration sources was performed using the previously prepared certificate files. The Perform Cascade Correction option was enabled. Regrettably, in the present edition of the software the cascade correction is not supported for multiline nuclides with complex decay schemes, like the ones from natural radioactive series.

The obtained efficiency values were fitted by the software to the function designated as "Dual" which has the form

$$\ln(\varepsilon) = a_0 + a_1 \ln(E_\gamma) + a_2 \ln^2(E_\gamma) + a_3 \ln^3(E_\gamma) + a_4 \ln^4(E_\gamma) + a_5 \ln^5(E_\gamma). \qquad (1)$$

Detection efficiencies calculation

The detection efficiencies for the sources prepared from test samples were calculated from the calibration source efficiencies (obtained in the previous step) using the method of relative effective solid angles, mentioned in the Introduction. In principle, with this method any unknown detection efficiency ε can be calculated from the known one ε_0 by the relation

$$\varepsilon = \varepsilon_0 \frac{\Omega}{\Omega_0}, \qquad (2)$$

where Ω and Ω_0 are the effective solid angles, first for the source-detector arrangement with a known efficiency, and the second for the source-detector arrangement with unknown efficiency.

The effective solid angles were calculated using the above software Angle [5]. As the input, this program needs the characterization (dimensions, density, and elemental composition of all materials) of the detector, with all its surrounding absorbing layers, and of the source, together with its container. The calculations were performed to the Gauss coefficient order 16 degree of precision on an energy grid ranging from 30 keV to 3000 keV with 35 values distributed to approximately evenly cover the logarithm of the energy range. The

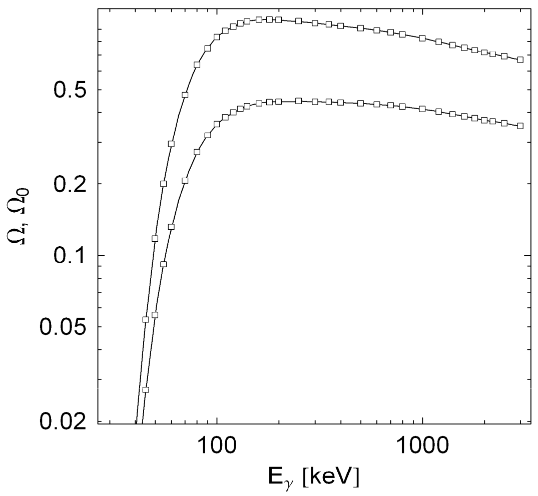

Figure 1. A typical pair of interpolated effective solid angle functions.

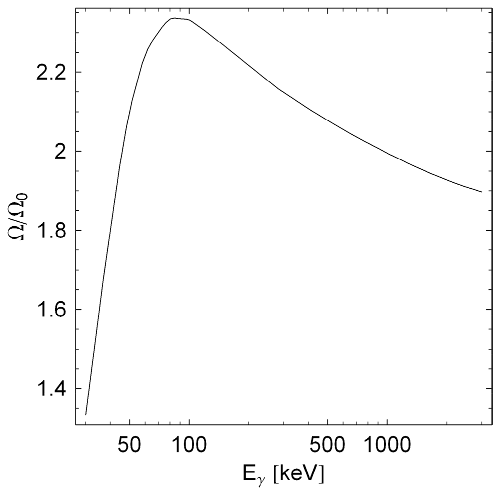

Figure 2. A typical ratio of effective solid angles as a function of energy.

obtained point values were interpolated to smooth functions $\Omega(E_\gamma)$ and $\Omega_0(E_\gamma)$, yielding this way also their ratio as a function of E_γ. No uncertainty analysis was performed at this step. A typical pair of solid angle functions is presented in Figure 1 and the corresponding ratio function in Figure 2.

Efficiency values $\varepsilon(E_\gamma)$ were calculated from (2) on the same energy grid on which the $\varepsilon_0(E_\gamma)$ was given for the actual calibration source. After processing all calibration sources, this procedure resulted in up to 200 $\varepsilon(E_\gamma)$ points for a given detector-test-sample arrangement, many of which were on the same or close energies. By taking the solid angle conversion as uncertainty-free, the relative uncertainties of ε remained the same as those of ε_0. The efficiency calibration routine of the GA&A software accepts only up to 80 points by direct entry, so the number of them had to be reduced. This was done firstly by dropping those with large uncertainties, which anyway would have very little influence to the final fit function, and secondly, by deriving the weighted mean of the ε values at the same or close energies. The remaining set of value pairs served as input to the GA&A program, where it was fit to the Dual efficiency curve (1).

3. Results and discussion

Efficiency curves

Some of the efficiency curves obtained as described in the previous section, together with the input point data, are shown in Figures 3 - 6. Large uncertainties of some data points, especially at low energies, as well as larger deviations of some points with smaller uncertainties, reflect the fact that this efficiency calibration method takes raw input data from very different sources, with different nuclides, activities, geometries, compositions. However, having in mind all the corrections made, and all the assumptions taken, the resulting efficiency curve actually looks quite well. The error corridor of the curve is rather narrow, due to the large number of data points, which diminishes the influence of outlier points.

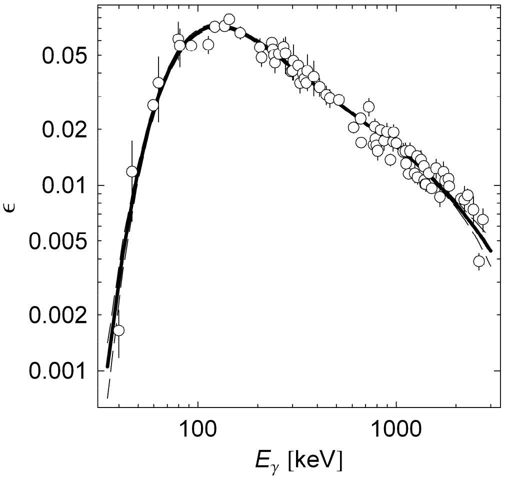

Figure 3. Input data and the calculated efficiency curve for the soil sample on detector K.

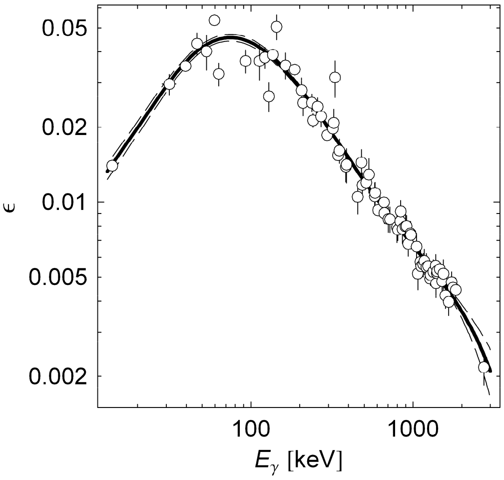

Figure 4. Input data and the calculated efficiency curve for the grass sample on detector L.

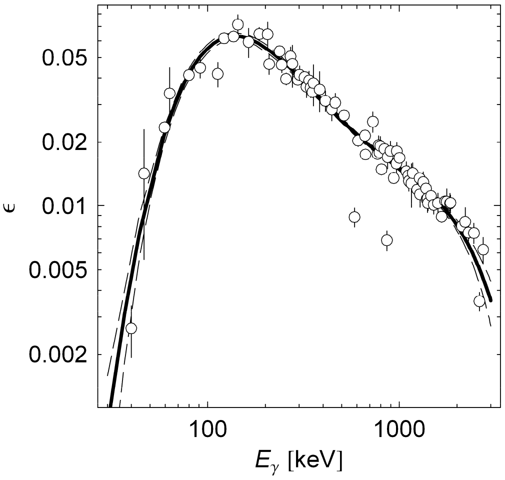

Figure 5. Input data and the calculated efficiency curve for the Marinelli water sample on detector K.

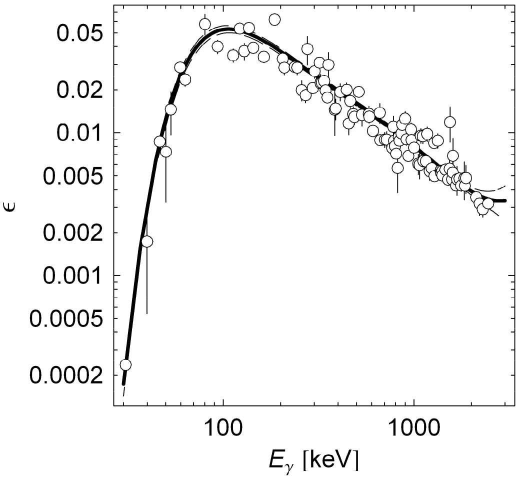

Figure 6. Input data and the calculated efficiency curve for the soil sample on detector M.

Measured activity concentrations and the comparison to IAEA values

The analysis of spectra acquired from test samples was performed in a manner similar to the spectra analysis of calibration source spectra, except that the efficiency calibration was taken as described in the previous section. The software could not automatically manage the peak separation of the relatively weak ^{109}Cd line at 88.0 keV from the complex multiplet structure of the background around this energy, hence some interactive peak fitting was needed. All the other line intensities and the nuclide identification and activity data were accepted as results of automatic processing.

The activity concentration data from spectra measured repeatedly on the same detector gave results in most cases coinciding within 1σ limits, and all of them were within 2σ

limits, with the exception of ^{109}Cd, which varied more widely from spectrum to spectrum. Weighted mean of the results for every detector, the laboratory weighted mean, and the IAEA data are presented in Tables 5-7. The numbers in the parentheses represent the 1σ of the last significant digit.

Table 5. Activity concentration of tested radionuclides in IAEA F0601 sample of soil.

Nuclide	Activity concentration [Bq/kg]				
	K	L	M	KLM	IAEA
^{54}Mn	50.1(9)	51.0(6)	40.7(8)	48(3)	48(1)
^{60}Co	59.6(13)	59.8(5)	57.0(7)	58.9(9)	56.1(14)
^{65}Zn	79.7(11)	80.7(11)	72.7(10)	77.3(26)	77.5(25)
^{109}Cd	0.17(3)e+03	0.16(5)e+03	104(15)	120(20)	178(8)
^{134}Cs	66.8(7)	67.4(5)	55.4(6)	64(4)	64.2(19)
^{137}Cs	54.8(5)	55.1(6)	43.8(8)	53(3)	52.6(11)
^{210}Pb	259(18)	274(23)	240(17)	255(11)	260(13)
^{241}Am	111.7(23)	110.8(28)	77.0(19)	95(12)	96.6(28)

With the exception of ^{109}Cd, data in Table 5 show a very good agreement between the laboratory mean values and the IAEA data for the soil sample. Most of values coincide within 1σ limits. However, if one looks at the single detector data, the detector M shows the largest deviations from true values. Actually, the detector M causes the failure of the ^{109}Cd result.

Table 6. Activity concentration of tested radionuclides in IAEA F0602 sample of grass.

Nuclide	Activity concentration [Bq/kg]				
	K	L	M	KLM	IAEA
^{40}K	1024(18)	1147(26)	1030(24)	1.05(4)e+03	1059(28)
^{137}Cs	11.90(6)e+03	12.60(13)e+03	9.32(6)e+03	10.9(10)e+03	11.32(18)e+03

Table 7. Activity concentration of tested radionuclides in IAEA F0603 sample of water. On detector K: KC - cylindrical source, KM - Marinelli source; detectors L and M - cylindrical source only.

Nuclide	Activity concentration [Bq/kg]					
	KC	KM	L	M	KLM	IAEA
^{54}Mn	4.45(24)	4.59(7)	4.81(22)	3.89(22)	4.55(11)	4.890(17)
^{60}Co	5.42(11)	5.31(5)	5.68(19)	4.79(21)	5.33(9)	5.80(4)
^{65}Zn	6.6(4)	6.65(19)	6.7(4)	5.4(6)	6.57(16)	7.27(8)
^{109}Cd	18.2(22)	20.0(8)	6.4(3)	11.6(13)	8.9(29)	19.62(10)
^{134}Cs	12.66(15)	12.19(9)	13.36(24)	10.02(14)	11.9(6)	13.03(10)
^{137}Cs	16.29(21)	16.15(16)	17.5(4)	12.72(29)	15.8(8)	16.72(8)
^{210}Pb	21(11)	6.9(24)	10.4(12)	15(4)	10.1(13)	9.55(15)
^{241}Am	3.33(24)	3.35(12)	3.03(16)	2.62(25)	3.18(14)	3.660(23)

It is evident from Table 6 that there is a perfect match between the mean laboratory values and the ones from IAEA for the grass sample. Still, there is room for improvement for ^{137}Cs on both the L and M detectors.

As can be seen from Table 7, there is a fair agreement between the laboratory mean values and the IAEA data for the water sample, again with the exception of ^{109}Cd. The largest deviations are again on the M detector. Large uncertainties for ^{210}Pb on detectors K and M show the big advantage of the GMX detector L in the low energy range (46.5 keV).

4. Conclusion

The results of the discussed comparative measurements of activity concentration in the IAEA-CU-2006-03 World-wide open proficiency test samples of soil, grass, and water show that there is a fair to excellent agreement between the laboratory and IAEA data for all the radionuclides except for ^{109}Cd. This single inconsistency is not due to an error of efficiency calibration, but to strong interference of the relatively intensive background on the detector M around 88 keV.

The results of individual detectors taken separately are slightly worse, with detector M showing the largest deviations from "true" data, in spite of the fact that all detectors were calibrated in the same manner, with the same calibration sources, using very similar efficiency calibration calculations, and the same spectra processing procedures. This difference may be ascribed to the incomplete knowledge of all the detector M parameters, as was noted in its description.

Every of the used efficiency calibration methods have its advantages and drawbacks. The calibration with point sources might look as the simplest. However, large distances must be kept for multiline sources in order not to provoke too large coincidence corrections. Also, the effective angle ratio for cylinder/point transformation is the largest, possibly introducing higher uncertainties.

Cylindrical calibration sources were made in the same geometry as the measured sample, and SRM even has a matrix similar to the soil sample, but the activity of SRM is impractically low. On the other hand, the phosphate ore F is more active, but it is not officially asserted. With both of these materials the radioactive equilibrium of the natural series is assumed, but this might deviate slightly. The coincidence correction might be significant, but is very complicated and was not performed. However, the composite contribution of the large number of gamma lines of natural series distributed along the whole energy region of interest hopefully cancels some of these inconsistencies.

The used closed voluminous calibration sources have the disadvantage of high count rate, giving rise to high dead time which might not be corrected precisely by the electronics. Also, the multiline ^{152}Eu needs significant coincidence correction. The asserted activity is expressed as for the water matrix (although it is resin) and the effective angle transformation ratio for other geometries is large.

Different calibration sources after effective angle ratio corrections produced results for a given detection efficiency which sometimes are not within statistical tolerance, in most cases for reasons which are not easily, if at all, traceable. This is mostly expressed in the low energy region. However, taken altogether, the large number of efficiency calibration data obtained by different calibration methods produced efficiency curves which proved to be correct.

Acknowledgments

The authors acknowledge the financial support of the European Agency for Reconstruction through the Ministry of International Economic Relations within the Neighboring Programme Hungary-Serbia (Action entitled ”Regional Water Resources Investigations in the Scope or Sustainable Development”, Grant No. 04SER02/01/009) and of the Ministry of Science of Republic of Serbia (project: Nuclear spectroscopy and rare processes, Number 141002B).

References

1. J. C. Aguiar, E. Galiano, J. Fernandez, Appl. Rad. Isot **64**, 1643 (2006).
2. M. J. Berger, J. H. Hubbell, S. M. Seltzer, J. Chang, J. S. Coursey, R. Sukumar, and D. S. Zucker, XCOM: Photon Cross Section Database, NIST, http://physics.nist.gov/PhysRefData/Xcom/Text/XCOM.html, (1998).
3. K. Debertin, R. G. Helmer, *Gamma- and X-ray Spectrometry with Semiconductor Detectors*, (North-Holland, New York, 1988).
4. M. Garcia-Talavera, H. Neder, M. J. Daza, B. Quintana, Appl. Rad. Isot. **52**, 777 (2000).
5. S. Jovanović, A. Dlabač, N. Mihaljević, P. Vukotić, XIX Jugoslovenski simpozijum za zaštitu od zračenja, Golubac, 1997, Jugoslovensko društvo za zaštitu od zračenja, Beograd, 1997, p. 127.
6. J. Lippert, Int. J. Appl. Radiat. and Isot. **34**, 1097 (1983).
7. L. Moens, J. De Donder, Lin Xilei, F. De Corte, A. De Wispelaere, A. Simonits, J. Hoste, Nucl. Instr. and Meth. **187**, 451 (1981).
8. J. M. Puzović, I. V. Aničin, Nucl. Instr. and Meth. in Phys. Res. A **414**, 279 (1998).
9. O. Sima, C. Dovlete, J. Radioanal and Nucl. Chemistry **200**, 191 (1995).
10. T. Vidmar, A. Likar, Nucl. Instr. and Meth. in Phys. Res. A **555**, 251 (2005) .

Journal of Research in Physics Vol. 31, No. 1, 31 - 36 (2007)

Cross-section for X-ray Production by Cosmic Muons

I. Bikit*, D. Mrdja*, I. Aničin**, M. Vesković*, S. Forkapić*
Department of Physics, Faculty of Sciences, University of Novi Sad, Serbia
**Faculty of Physics, University of Belgrade, Serbia*
e-mail: bikit@im.ns.ac.yu

Received: *February 9, 2007*

Abstract

Muons have a small cross-section for interactions and high energy, so they are very penetrating and give the significant contribution to the gamma spectra of Ge detectors, even in deep underground laboratories. One of the muon interaction effects with material is X-ray production. Having in mind that gold is often used as a detectors component, in this paper the production of X-rays in gold sample is analyzed by using a coincidence system based on plastic scintillation detector and Ge detector. The production rate of K_α rays per Au mass unit from coincidence gamma spectrum is determined as $R \approx 7.1 \cdot 10^{-4}$ g^{-1}s^{-1}. Taking into account the measured muon flux of $\Phi = 54$ s^{-1}m^{-2}, the muon cross-section $\sigma_{K_\alpha} \approx 43$ Barn, for Au K_α X-rays production is calculated. Also, the cross-sections of X-ray production by cosmic muons in lead and tungsten are measured. Unexpectedly, the results obtained did not reveal Z dependence in the $Z = 74 - 82$ region.

Key words: Cosmic muons, X-ray production, cross section

1. Introduction

Cosmic rays consist primarily of very high energy protons and alpha-particles originating from stellar processes. The top of Earth's atmosphere is bombarded by a flux of these charged particles. The primary cosmic rays collide with the nuclei of air molecules and produce a secondary particle showers that include protons, neutrons, pions (charged and neutral), kaons, photons, electrons and positrons. The secondary particles then undergo electromagnetic and nuclear interactions to produce additional particles in a cascade processes.

Some of the charged pions will interact via the strong force with air molecule nuclei, but others will spontaneously decay via the weak force into muon and neutrino or antineutrino:

$$\pi^+ \rightarrow \mu^+ + \nu_\mu$$

$$\pi^- \rightarrow \mu^- + \bar{\nu}_\mu$$

Muons interact with matter only through the electromagnetic and weak forces, traveling a relatively long distance while losing its kinetic energy, and finally decay into an electron and antineutrino. Also, after deceleration, negative muons can bind to the atomic nuclei and then interact with protons before they spontaneously decay:

$$\mu^- + p \rightarrow n + \nu_\mu .$$

Application of high-resolution gamma spectrometry to the problems with low event rates has important role in nuclear and subnuclear physics and particle astrophysics [1]. The interaction of cosmic rays with various types of materials can be observed in case that the detector construction and shielding materials are carefully selected to have high radiopurity. Studies of cosmic ray interactions, especially of most penetrating muon component, lead to improving of low background experiments.

There are four types of different spectral components of Ge detectors [2] caused by muons:

1. characteristic X-rays of materials close to the Ge crystal
2. bremsstrahlung continuum from muon generated electron showers
3. annihilation peak produced in shower pair production [3] and
4. activation of materials by muons.

The exploration of the characteristic X-rays induced by cosmic muons in various materials (gold, lead, tungsten) is presented in this paper. Some of non-accelerator low background particle physics experiments based on using Ge detectors include materials mentioned above. Those materials are potential sources of muon-induced X-rays and lead to increasing of low energy part of the gamma spectrum. In the present work we measured the cross-sections for X-ray production by cosmic muons.

2. Experimental results and discussion

Measurements of cross-sections for X-rays production by cosmic muon flux is based on coincidence electronic circuit of high purity extended range Ge detector and scintillation plastic detector. Our experiment was designed to measure the production of fluorescence characteristic X-rays of materials in the vicinity of a Ge detector by secondary particles that emerge from interactions of CR muons with heavy lead shields of low-background Ge detectors. It was designed to be insensitive to the X-rays directly produced by CR muons in the target material, since these production rates are easily evaluated by contemporary simulation codes, GEANT4 for instance, and there is little interest to determine this yield experimentally. Production by the secondaries, however, is a complex process involving many different low-energy cascades, and is much more difficult to evaluate. Figure 1 illustrates the geometry of the experiment and explains why the direct production of X-rays by muons does not contribute to the X-ray lines.

The schematic view of the coincidence system is shown in Fig. 2. The GMX type "ORTEC" HPGe spectrometer with nominal efficiency of 32 % is placed inside the lead shield of cylindrical shape with the outer diameter of $\Phi = 410$ mm, and wall thickness of 120 mm. The inner absorption layer consists of 3.5 mm thin and 0.5 mm made of copper. The plastic detector with dimensions of 0.5 m × 0.5 m × 0.05 m was positioned above the lead shield, and samples were placed at the distance of 7.5 mm from the Ge detector end cap. The SCA window (Δt) of TAC/SCA module was 270 ns and the gating of Ge detector energy signals was done by signals of 110 μs width from the DELAY/GATE generator, fed by SCA output of TAC/SCA. The threshold on CFD of plastic detector corresponded

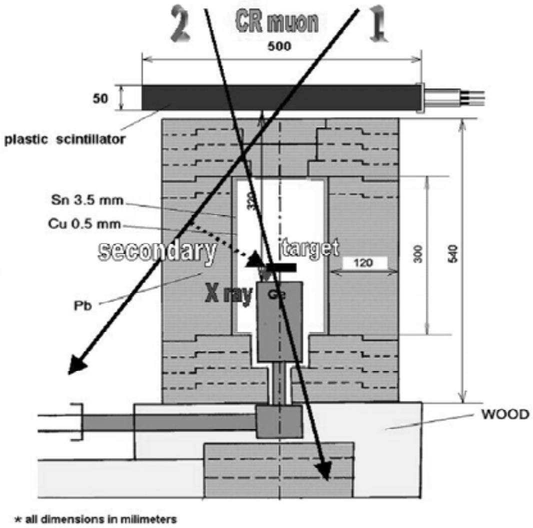

Figure 1. Arrangement of detectors and materials in the experiment. CR muon passes through the plastic scintillation detector and triggers the HPGe detector. The muon marked "1" then produces a secondary (dotted line) in the heavy lead shield which is in turn stopped in the target where it induces the emission of the X-ray, which is registered by the HPGe detector in the X-ray peak. If the muon (marked "2") hits the target and produces the X-ray which is detected by the Ge detector, it also passes through the Ge detector and its energy loss is summed with the X-ray, which is then registered ouitside the X-ray peak.

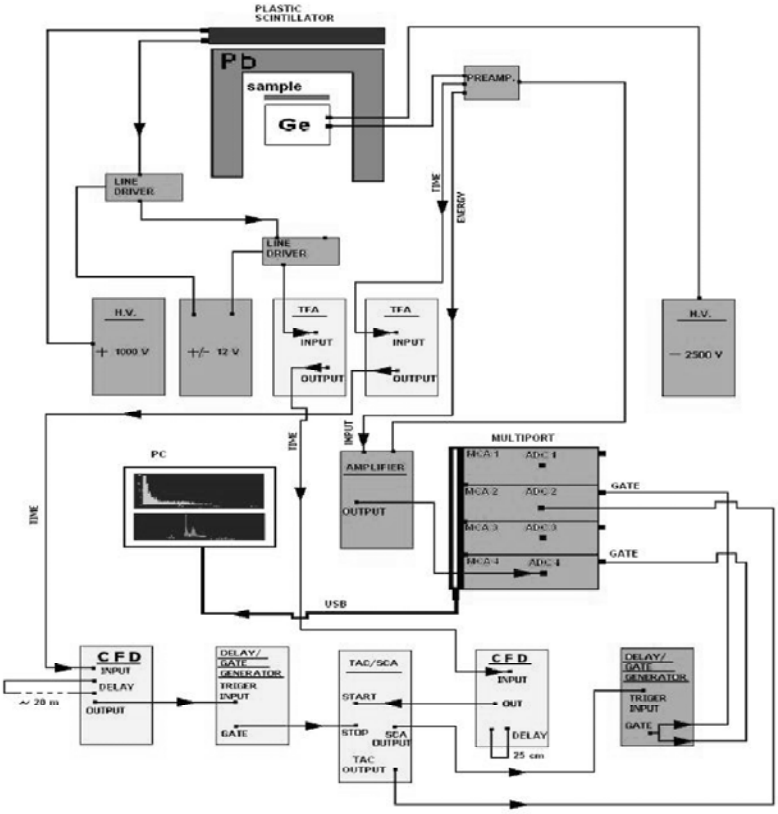

Figure 2. The schematic view of the coincidence circuit.

to an energy of about 6 MeV (beginning of muon deposited energy peak in 5 cm thick plastic detector) and the threshold on CFD of Ge detector was about 35 keV.

The characteristics of disk-shaped samples are presented in Table 1.

Table 1. The characteristics of samples.

No.	Substance	Mass [g]	Radius [cm]	Thickness [cm]
1	Au	40.6	3.34	0.06
2	Pb	53.2	3.69	0.11
3	WO_3	20.2	3.35	0.25

The coincidence Ge spectra of Au, Pb and WO_3 are shown in Fig. 3. Using the equation

$$\sigma = \frac{R}{N\Phi}$$

the cross-sections σ for muon producing of K_α X-rays were calculated, where:

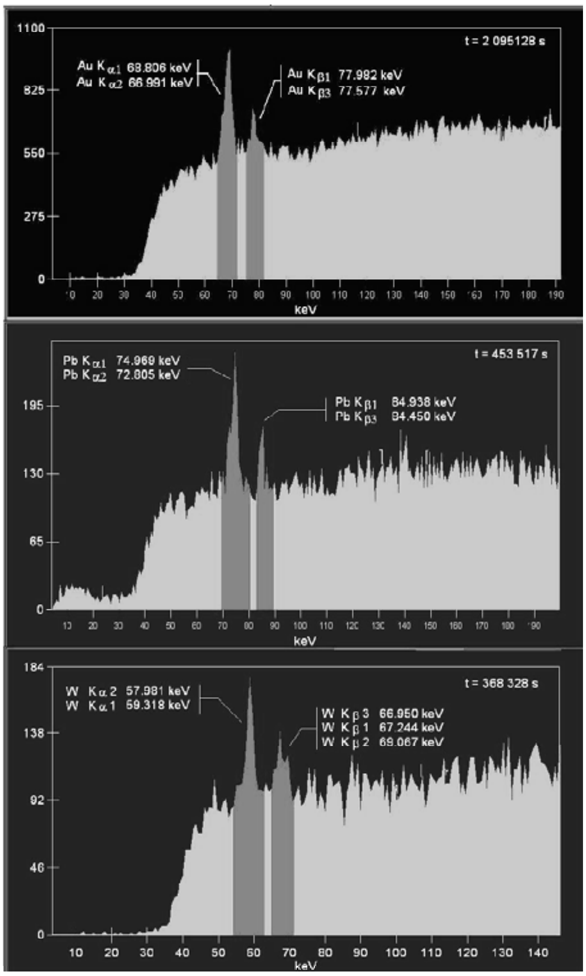

Figure 3. The coincidence spectra of the HPGe detector. When gold, lead and tungsten targets are positioned in front of the detector. Only K_α and K_β lines of the corresponding element are seen in the spectra.

R - number of produced X K_α-quanta in the sample per unit of time :

$$R = \frac{n}{\varepsilon t}$$

(n - number of events in X K_α-photo peak of the coincidence spectrum, ε - efficiency of detection, t - live time of measurements)
N - number of atoms (Au, Pb, W) in the sample
Φ - measured muon flux: 54 $\mathrm{s}^{-1}\mathrm{m}^2$ (for cosmic muons with mean energy of about 2 GeV)

The results of calculations are presented in Table 2, and in Fig. 4.

Table 2. Values of the effective cross sections.

No.	Element	Atomic number	Cross-section [Barn]
1	Au	79	43 ± 3
2	Pb	82	46 ± 4
3	W	74	49 ± 7.5

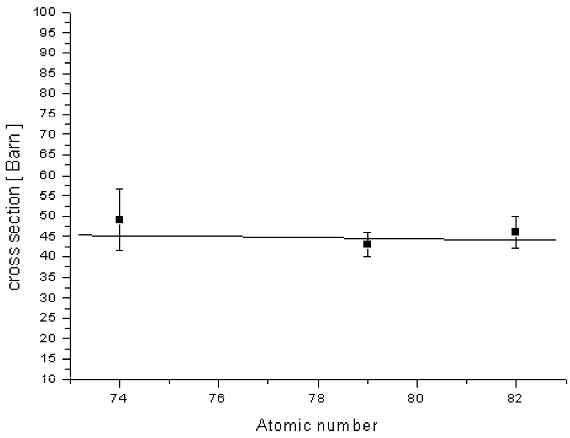

Figure 4. Z dependence of the cross section values.

3. Conclusion

The cross-sections for producing of X-rays by cosmic muons have relatively high values for the analyzed materials with high atomic number (W, Au, Pb) - about 45 Barn. The Z dependence of cross-sections in this narrow Z region $(74 - 82)$ is not noticeable, having in mind almost constant measured values of cross-sections. That is qualitatively different from the probability of muon capture in target nuclei, although it has strong Z dependence: $\sigma_{cap.} \sim Z^4$ [4], or production of positron annihilation radiation by cosmic rays muons: $\sigma_{ann} \sim Z^2$ [3].

Further explorations on this field will be continued.

Acknowledgments

The authors acknowledge the Provincial Secretariat for Science and Technological Development of the Autonomous Province of Vojvodina (Project No 114-451-00631/2006-1) and Ministry of Science and Environmental Protection of the Republic of Serbia (Project: Nuclear spectroscopy and rare processes, Number 141002B) for the financial support of this research.

References

1. G. Heusser, Annu. Rev. Nucl. Part. Sci. **45**, 543 (1995).
2. G. Heusser, Nuclear Instruments and Methods in Physics Research A **369**, 539 (1996).
3. J. M. Puzović, I. V. Aničin, Nuclear Instruments and Methods in Physics Research A **480**, 565 (2002).
4. R. Nunez-Lagos, A. Vitro, Appl. Radiat. Isot. **47**, 1011 (1996).

Journal of Research in Physics Vol. 31, No. 1, 37 - 46 (2007)

Dehydrogenation of Low-temperature ECR-plasma Silicon Nitride Films under Rapid Thermal Annealing

A. Kovalchuk, G. Beshkov*, S. Shapoval
Institute of Microelectronic Technology, Russian Academy of Sciences,
Chernogolovka, Moscow district 142432, Russia
e-mail: anatolij@ipmt-hpm.ac.ru
**Institute of Solid State Physics, Bulgarian Academy of Sciences, Sofia, Bulgaria*
e-mail: beshkov@issp.bas.bg

Received: *February 16, 2007*

Abstract

Some theoretical aspects of the mechanism and kinetics of low-temperature silicon nitride thermal annealing were considered. We have introduced a formula for silicon nitride - $H_xSi_rN_zH_y$, in view of the fact that the hydrogen H_x bonded to Si and hydrogen H_y bonded to N have different influences on the values of bulk or surface charge and mechanical stress. The influence of rapid thermal annealing on the concentrations of (Si–H) and (N–H) bonds (C(Si–H) and C(N–H)) in ECR-plasma silicon nitride $H_xSi_rN_zH_y$ films was studied. Four series of rapid thermal annealing experiments lasting $t = 15, 30, 60, 180$ s were carried out at six temperatures $T = 450, 600, 700, 800, 1000, 1200°$C for each series. Both C(Si–H) and C(N–H) start to decrease at the temperature $T = 700°$C, but then C(Si–H) shows a paradoxically sharp increase beginning from $T = 1000°$C. We assume that this effect is determined by kinetics of diffusion controlled reactions in solid phase and that there is a large difference of oscillator strengths constant between (Si–H) and (H–Si–H) stretching modes in the infrared spectra. For calculation of C(Si–H) and C(N–H) integrated processing of Fourier transform infrared spectra (FTIRS) was used.

Key words: Silicon nitride, rapid thermal annealing, ECR-plasma, Fourier transform infrared spectra

1. Introduction

There is a great interest in amorphous silicon nitrides $H_xSi_rN_zH_y$ since they are widely used as encapsulation, passivation, dielectric and barrier layers. Amorphous silicon nitride thin films are used in different fields because of their advantageous electrical and/or optical properties. These films are especially suitable for the silicon surface electronic passivation in high efficiency Si solar cell technology, as antireflection coatings (according to well-known ratio of the refractive indexes: $[n(H_xSi_rN_zH_y)]^2 \approx n(\mathrm{Si})$) [1]. Besides, to get a low interface state density, the field-effect passivation [2] plays an important role for the low recombination rates at the ($H_xSi_rN_zH_y$)/Si interface: in the Si-rich $H_xSi_rN_zH_y$ a large number of fixed charges are created near the interface to the Si. These charges induce band bending under the Si-surface, which leads to the inversion of holes at a p-Si surface. The inversion of holes leads to a low recombination rate, since these holes are excluded from the processes of hole-electron recombination [3]. A characteristic property of amorphous silicon nitride is the presence of the electronic states located in the forbidden energy band. The effect of localization of electrons and holes, injected into amorphous silicon nitride, is the basis of memory elements. In a MNOS-memory element the positive or negative charge is stored in deep traps of silicon nitride near the interface with SiO_2 and rewriting is performed by applying the pulses with an amplitude $> 10^6$ V/cm.

Low-temperature silicon nitride thin films are suitable for gate and interlayer dielectrics for thin film transistors (TFT) on low-temperature glass and plastic substrates, for barrier layers in gate stack high-k dielectric structures, for passivation and encapsulation layers in III/V microelectronics applications, and for encapsulation layer on non-conventional substrates (i.e. plastic or metal foil) [4]. The mechanical, chemical and optical properties of silicon nitride allow the fabrication of membranes in surface micromachining technology and microinterferometers in optoelectronic technology. In recent years, low-temperature silicon nitride has been used in microbridge structure technology for manufacturing uncooled microbolometers ("0.2 μm thick bridge of silicon nitride suspended about 2 μm above the underlying silicon substrate") [5].

Plasma-enhanced chemical vapor deposition (PECVD) is the most popular procedure for low-temperature silicon nitride deposition. However, high-energy ion emission from volume of RF-discharger on microstructure surface gives rise to well-known defectiveness problem in microelectronics applications. The combination of remote plasma enhanced chemical vapor deposition (RPECVD) with the subsequent rapid thermal annealing in an inert ambient may be suitable for ultra-thin silicon nitrides gate dielectrics [6]. The electron cyclotron resonance (ECR) plasma method shares the advantages of the remote plasma system in view of low ion energy ($\sim$ 30 eV). Moreover, high plasma density ($\sim 10^{12}$) provides sufficient flows of the active species (i.e., :N., :N.$^+$, :SiH_2, :SiH_2^+, :Si.H, :Si.H$^+$, :Si:, :SiP:$^+$) for deposition of high quality low- or room-temperature silicon nitrides without performing a post-deposition processing step.

Low-temperature silicon nitride $H_xSi_rN_zH_y$ contains a large amount of hydrogen atoms (up to 38 %) chemically bonded to Si and N. The presence of hydrogen atoms in silicon nitride structure leads to the passivation of structural defects (i.e. dangling ≡Si· and =N· bonds) in the bulk of the film and at the insulator-semiconductor interface, and reduces the density of electrically active defects (i.e. ≡Si–Ši–Si≡). It is probable that the deep traps and emission centers in the silicon nitride are silicon clusters, i.e. ≡Si–Ši–Si≡ with the average size of ~ 10 Å, simulating both the donors and acceptors centers. It is necessary to note, that the clusters model of traps explains full compensation of donors and acceptors and simultaneous existence of deep traps for electrons and holes. The electrical quality of $H_xSi_rN_zH_y$ depends on the relative concentrations of ≡Si–, =N– and H– atoms, and the way these atoms are integrated into the network structure, especially the distribution of H– bonded in (Si–H) and (N–H).

For example, silicon nitride high-temperature annealing, during which concentrations of (Si–H) and (N–H) bonds vary [7], has an essential influence on the period of charge storage in a MNOS-memory element. Variation of the hydrogen concentration in passivation silicon nitride films allows one to control the main parameters of the Al_xGa_yN/GaN

- HEMT transistors.

The silicon nitride films, obtained at the excess of NH_3 or N_2 in the reactor valve, contain the hydrogen mainly connected with nitrogen. It is known, that the presence of =NH and $-NH_2$ groups decreases the mechanical stress in films [8]. The silicon nitride films, obtained at the excess of SiH_4 in the reactor valve, contain the hydrogen mainly connected with silicon. It is considered that the presence of ≡SiH and $=SiH_2$ groups in the clusters (i.e. ≡Si–Ši–Si≡) is responsible for the ability to store charge in the bulk of the film and accounts for the influence on the number of fixed charges near the $H_xSi_rN_zH_y$ interface [8].

We have introduced a formula for silicon nitride as $H_xSi_rN_zH_y$, where the hydrogen H_x connected to Si and hydrogen H_y connected to N exert different influences on the values of bulk or surface charge and mechanical stress.

The presence of hydrogen and superfluous silicon in the silicon nitride films essentially expands their functionalities and in this sense has a positive value. However, the –H bonded in the $H_xSi_rN_zH_y$ network shows poor thermal stability and may lead to degradation of the favorable electronic and structural properties of the films [9]. For example, a well known degradation phenomenon is observed in MNOS devices. Therefore, the prediction of the silicon nitride properties under temperature or high electric field stresses is very important for microelectronic devices in view of the reliability and improvement of parameter reproducibility.

The thermal annealing of low-temperature silicon nitride in vacuum or in an inert gas atmosphere results in a decrease of hydrogen bonds concentration with the formation of long-living radicals ≡Si and =N· (dangling bonds), that is, it is possible to treat it as the conductivity centers concentration increase. Also, new (Si–Si) and (Si–N) bonds are formed, the gases H_2, N_2, NH_3 are in parallel observed and the increase of films conductivity can be observed as well. The thermal annealing of low-temperature silicon nitride at temperatures higher than 1200 K results in crystallization of layers and approaching of their structure to Si_3N_4.

2. Theoretical part

Chemical composition (x, r, z, y) and the resulting density ρ, depending on the conditions and the way of $H_xSi_rN_zH_y$ films deposition, can vary over a wide range. It is very convenient to normalize the sum $(x+r+z+y)$ to 100 units, then $(x+r+z+y) = 100$ % and $x = C$(Si–H), $r = C$(Si), $z = C$(N), $y = C$(N–H) and for total hydrogen contents $h = (x+y)$. For the known samples of high-temperature deposition (temperatures higher than 1200 K) silicon nitride films have $h_{min} \approx 7$ % and $\rho_{max} \approx 3.1$ g/cm^3. In the samples of low-temperature deposition (temperatures lower than 600 K) silicon nitride films are characterized with $h_{min} \approx 14$ % and $h_{max} \approx 38$ %. It is obvious that ρ decreases with increase in h, as well as with increase in C(Si–Si) (since ρ(Si) ≈ 2.42 g/cm^3). Assuming $\rho = 2.9$ g/cm^3, for the composition $H_8Si_{36}N_{48}H_8$ with $h = 16$ % an average distance $s \approx 3.9$ Å between the centers of hydrogen neighbor atoms is obtained. Thereby, the existence of mechanisms of hydrogen atoms displacement on $(s - 2R_H)/2 \approx 1.5$ Å can open a way to possibility of bimolecular reactions in low-temperature silicon nitride.

The mechanism and kinetics of thermal annealing depend not only on the concentrations of (Si–H) and (N–H) bonds, but also on distribution of H– bonds in the $H_xSi_rN_zH_y$ network between ≡SiH, $=SiH_2$, =NH, $-NH_2$ groups and, apparently, on the thickness of

the film in case of rapid annealing. It is necessary to have in mind the exponential temperature dependence of the $\cdot$H, H_2, :N., :NH, $\cdot NH_2$, NH_3 diffusion coefficients in the solid phase: $D_i = D_{0i} \times \exp(-A_i/RT)$, where A_i - activation energy for diffusion processes. According to [10]
$\rightarrow D_o(\cdot\mathrm{H}) = 8 \cdot 10^{-4}\ \mathrm{cm}^2/\mathrm{s},\ \ A(\cdot\mathrm{H}) = 4.30 \cdot 10^4\ \mathrm{J/mol}$,
$\rightarrow D_o(\mathrm{H}_2) = 5 \cdot 10^{-4}\ \mathrm{cm}^2/\mathrm{s},\ \ A(\mathrm{H}_2) = 4.30 \cdot 10^4\ \mathrm{J/mol}$,
$\rightarrow D_o(:\mathrm{N}.) = 4 \cdot 10^{-4}\ \mathrm{cm}^2/\mathrm{s},\ \ A(:\mathrm{N}.) = 2.34 \cdot 10^5\ \mathrm{J/mol}$.
And, according to well known estimation formula $\tau(x) = \langle x^2\rangle/2D$, we can estimate the times of diffusion output of H_2 and :N. from the silicon nitride film of the thickness $d = 1000$ Å $(\langle x^2\rangle = d^2/3)$
$\rightarrow \tau(\mathrm{H}_2, 800\ \mathrm{K}, 1000\ \text{Å}) = 2.1 \cdot 10^{-5}\ \mathrm{s}$,
$\rightarrow \tau(:\mathrm{N}., 800\ \mathrm{K}, 1000\ \text{Å}) = 7.9 \cdot 10^{7}\ \mathrm{s} = 2.5$ years.
But, for the time diffusion output :N. from a cell with a radius $\langle c\rangle = 2$ Å, in view of the Gauss distribution, $(2\langle c^2\rangle = \pi\langle c\rangle^2)$ and $\tau(c) = \langle c^2\rangle/6D$ is obtained
$\rightarrow \tau(:\mathrm{N}., 800\ \mathrm{K}, 2\ \text{Å}) = 500\ \mathrm{s}$.

It is also necessary to have in mind the dependence of the $\cdot$H, H_2, :N., :NH, $\cdot NH_2$, NH_3 diffusion coefficients in the film on its chemical composition. We assume that the low-temperature silicon nitride contains a large amount (more than 20 %) of hydrogen in the $\equiv$SiH, $=SiH_2$, =NH, $-NH_2$ groups, like a three-dimensional polymer (the polymer constructed from linear macromolecules, connected among themselves by cross-linking bonds, so that a spatial grid is formed).

It is obvious that with an increase of hydrogen contents the structure of silicon nitride will approach the structure of a standard polymeric film. At the hydrogen contents $h =$ 60 %, a silicon nitride would become similar to linear polymer → $-[H_2Si_1N_1H_1]-$
At the hydrogen contents $h = 63$ % it will be a liquid → $H_6Si_3N_4H_6$
At the hydrogen contents $h = 67$ % it will be a gas → $H_2Si_1N_2H_4$

By modeling diffusion controlled chemical processes accompanied by silicon nitride annealing, we obtained diffusion activation energy dependence on the hydrogen contents $\rightarrow a_i(h) = A_i \times [1 - (h/H)^2]^{1/2}$, where A_i - activation energy for the non-hydrogen film and $H = const = 63$ %. Therefore, it is necessary to bear in mind that a relatively small increase of diffusion activation energy $a_i(h)$ in the annealing process (when h decreases) can result in a very large reduction of diffusion coefficients. For example, when $D_o = 4 \cdot 10^{-4}\ \mathrm{cm}^2/\mathrm{s}$, $A = 2.34 \cdot 10^5$ J/mol at $h = 0.36$ it is obtained $\rightarrow a(0.36) = 1.92 \cdot 10^5$ J/mol, which results in a change of the output time diffusion from $\tau(0.36) = 1$ s → to $\tau(0.00) =$ 500 s in case of the cell $\langle c\rangle = 2$ Å.

It is well known that polymer-like films contain various low-molecular fragments C→ (Fig. 1: 1-7) and trailer groups –C→ (Fig. 1: 8-10).

It is necessary to take into account that nano cracks containing nano voids W with bonded –H, as well as nano voids V without bonded –H, in the structure of polymer-like silicon nitride increase diffusion mobility of $\cdot$H, H_2, :N., :NH, $\cdot NH_2$ and low-molecular fragments C.

In Table 1 the cycle of $H_xSi_rN_zH_y$ thermal annealing solid-phase process is presented. We assume that turning diffusion of C and, maybe, jumping diffusion of C between nano voids, according to the equations (1-3) are the basic mechanisms of bonded –H displacement at a distance of ∼ 1 Å. We cannot exclude the presence of linear macromolecular fragments shifting diffusion inside nano voids and nano cracks at a distance of ∼ 1 Å. The equations (1-4) represent the mechanisms of bimolecular reactions limited by the jumping

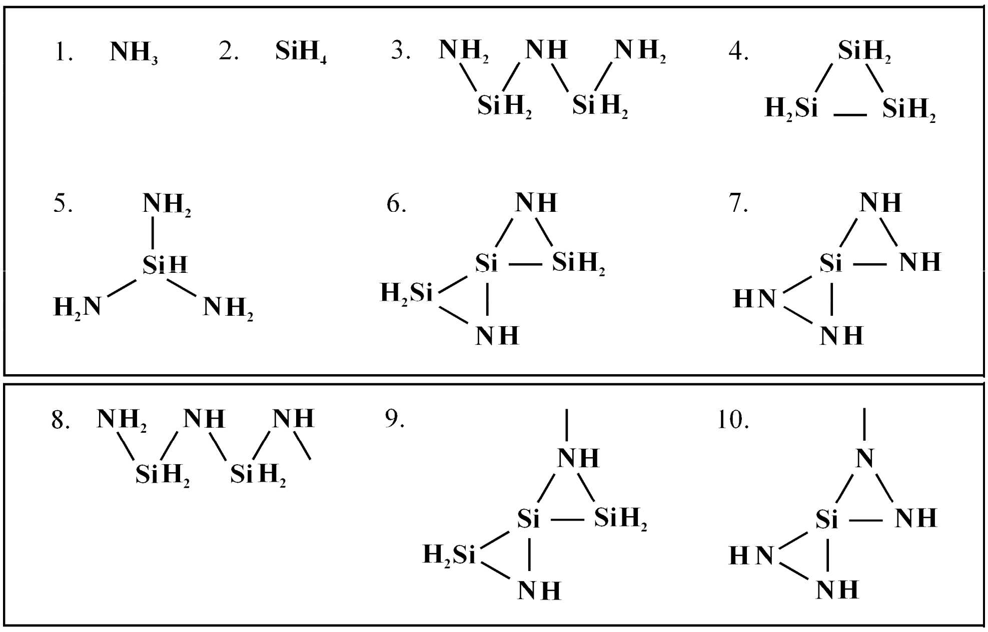

Figure 1. Low-molecular fragments C→ (1-7) and trailer groups –C→ (8-10).

diffusion between nano voids and by the turning diffusion of low-molecular fragments C containing bonded –H. Equation (5) represents the mechanism of the bimolecular reaction limited by the shifting diffusion inside nano voids and nano cracks of linear macromolecule fragments containing bonded –H. We assume that (1-5) mechanisms describe a low-temperature ($T < 1000$ K) and an initial stage of the $H_xSi_rN_zH_y$ annealing with high (more than 20 %) content of hydrogen. According to experimental data [9], at a long annealing time (more than 1 hour), allocation of H_2 is already appreciable at 700 K. With the time of annealing process an attenuation of this mechanism occurs because of the formation of new ≡Si–Si≡ and ≡Si–N= bonds, and, as a consequence, increases the activation energies of the diffusion processes. For the renewal of this mechanism it is necessary to increase annealing temperature again and again.

Finally, at $T \sim 1100$ K, the mechanism presented by equations (6-15) is operative. Obviously, the limiting stage of this mechanism is the extraction of the ·H from the ≡ Si–H or =N–H according to equation (6), and of the NH_2 from the ≡Si–NH_2 according to equation (9).

It is obvious that the feature of rapid thermal annealing at $T > 1100$ K is a cross-section of the mechanisms (1-5) and (6-16), and the diffusion controlled processes (1-5) are quickly "sewn up" by the process (15). As we can see, the process of a rapid thermal annealing has a very complex mechanism, hence, it is necessary to demand high quality experimental data and, obviously, the calibration of experimental techniques. In our work, some features were found in the application of integrated Fourier transform infrared spectra processing for calculation of C(Si–H) and C(N–H).

Table 1. Solid-phase in $H_xSi_rN_zH_y$ thermal annealing processes.

No.		equation			
(1)	VC + V	($k_1 \rightarrow \leftarrow k_1$)	V + VC		
(2)	VC + W	($^+k_2 \rightarrow \leftarrow {}^- k_2$)	V + WC		
(3)	WC + W	($k_3 \rightarrow \leftarrow k_3$)	W + WC		
(4)	WC	($^+k_4 \rightarrow \leftarrow {}^- k_4$)	*WC	($k_4 \rightarrow$)	$W_0 + H_2$
(5)	W	($^+k_5 \rightarrow \leftarrow {}^- k_5$)	*W	($k_5 \rightarrow$)	$W_0 + H_2$
(6)	QH	($^+k_6 \rightarrow \leftarrow {}^- k_6$)	Q· + ·H		
(7)	QH + ·H	($k_7 \rightarrow$)	Q· + H_2		
(8)	H· + ·H	($k_8 \rightarrow$)	H_2		
(9)	QNH_2	($^+k_9 \rightarrow \leftarrow {}^- k_9$)	Q· + ·NH_2		
(10)	QH + ·NH_2	($^+k_{10} \rightarrow \leftarrow {}^- k_{10}$)	Q· + NH_3		
(11)	QH + ·NH_2	($k_{11} \rightarrow$)	QHN· + H_2		
(12)	H_2N· + ·NH_2	($k_{12} \rightarrow$)	$N_2 + 2H_2$		
(13)	H· + ·NH_2	($^+k_{13} \rightarrow \leftarrow {}^- k_{13}$)	NH_3		
(14)	QSiH + NH_3	($k_{14} \rightarrow$)	$QSiNH_2 + H_2$		
(15)	Q· + ·Q	($k_{15} \rightarrow$)	Q-Q		
(16)	Diffusion	·H, H_2, N_2,	·NH_2, NH_3		

Where
C - concentration of low-molecular fragments containing hydrogen atoms,
V - concentration of inactive (without –H) nano voids,
W - concentration of active (with –H) nano voids,
VC - concentration of C in inactive nano voids,
WC - concentration of C in active nano voids,
*WC - transition state (–H—H–),
*W - transition state (–H—H–),
VC + WC total concentration of C,
W_0 - "sewed" nano voids (≡Si–Si≡, ≡Si–N=).
and
k_1, $^+k_2$, $^-k_2$, k_3 - jumping diffusion rate constants,
$^+k_4$, $^-k_4$ - turning diffusion rate constants,
$^+k_5$, $^-k_5$ - shifting diffusion rate constants.
and
Q·, ·Q - either ≡Si· or ·N=

3. Experimental details

Silicon nitride $H_xSi_rN_zH_y$ films $d = (100 \div 3000$ Å$)$ were deposited from monosilane SiH_4 diluted in argon (1/3) and nitrogen using an ECR plasma reactor. Silicon nitride films were deposited by varying substrate temperature $T = (20 \div 300°C)$, SiH_4/N_2 flow ratio $R = (0.75 \div 1.25)$, pressure $p = (1 \div 6$ mTorr$)$, microwave power $E = (200 \div 500$ W$)$. Initial (Si–H) and (N–H) bonds concentrations (x and y) in low-temperature silicon nitride can vary over a wide range, from $x_{min} \approx 2$ % and $y_{min} \approx 2$ % to $x_{max} \approx 36$ % and $y_{max} \approx 36$ %, depending on the ECR-plasma conditions. But, at a given temperature, only at a certain combination of ECR-plasma parameters (R, p, E) the minimum h_{min} of hydrogen bonds total concentration $h = (x + y)$ can be achieved. For example, at

$T = 200°\text{C}$ it was obtained $h_{min} \approx 16$ %. It is interesting to note that $x \approx y$ in the case of total concentration $(x + y)$ minimum. In the case when $x = x_{min}$ then $y = y_{max}$, and in case when $x = x_{max}$ then $y = y_{min}$.

In this publication we have discussed the influence of rapid thermal annealing on the parameters of one of our sample with silicon nitride film deposited on silicon substrate at $T = 100°\text{C}$ (initial $x = C(\text{Si–H}) \approx 5.0$ %, $y = C(\text{N–H}) \approx 26.4$ % and film thickness $d =$ 1400 Å). Four series of rapid thermal annealing experiments lasting $t = 15, 30, 60, 180$ s were carried out at six temperatures $T = 450, 600, 700, 800, 1000, 1200°\text{C}$ for each series.

FTIR-spectrometer PERKIN-ELMER 1720X was used for scanning of silicon nitride spectra. FTIRS were recorded at a resolution of 4 cm^{-1}, with 36-times accumulation of scans, and with a signal/noise ratio = 3000 for one scan.

4. Experimental results

Experimental results are shown in Figs. 2-7. Fig. 2 shows the basic bands of IR-vibrations in FTIRS of $H_xSi_rN_zH_y$ film deposited under ECR-plasma conditions and substrate temperature $T = 100°\text{C}$.

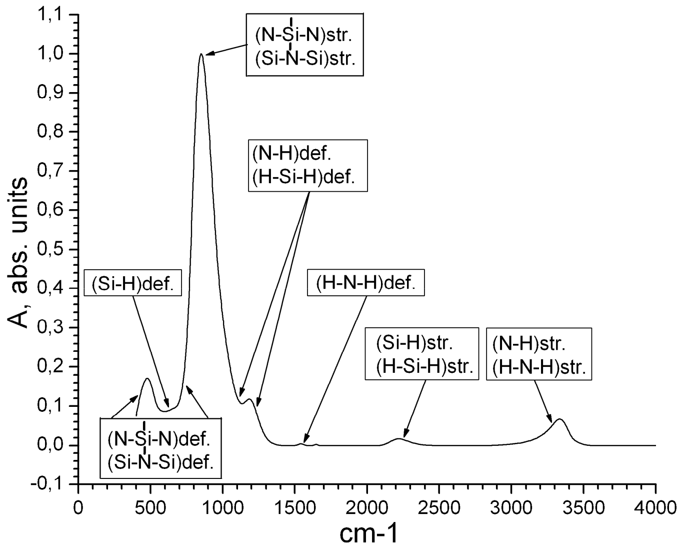

Figure 2. FTIRS of $H_xSi_rN_zH_y$ film deposited under ECR-plasma conditions and substrate temperature $T = 100°\text{C}$.

In Fig. 3, variations of the (Si–H) and (N–H) stretching vibrations during 60 s of annealing are presented. The C(Si–H) decreases with increase in temperature from $T =$ 100°C to $T = 1000°\text{C}$ and then increases from $T = 1000°\text{C}$ to $T = 1200°\text{C}$. FWHM (peak width on half of its amplitude) consistently decreases from 158 cm^{-1} to 107 cm^{-1}.

The center of (Si–H) band is consistently displaced from 2220 cm^{-1} to 2170 cm^{-1}. The C(N–H) decreases with increase in temperature from $T = 100°\text{C}$ to $T = 1000°\text{C}$, and to $T = 1200°\text{C}$. The FWHM consistently decreases from 166 cm^{-1} to 143 cm^{-1}. The maximum of the (N–H) band remains unchanged, close to 3330 cm^{-1}.

In Fig. 4, variations of the (Si–H) and (N–H) stretching bands during 180 s annealing are presented. The C(Si–H) decreases with increase of temperature from $T = 100°\text{C}$ to

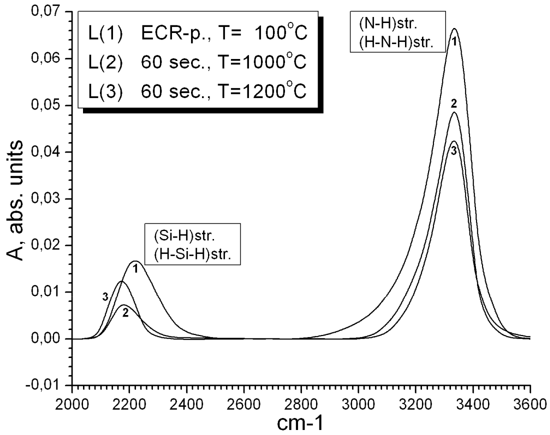

Figure 3. FTIRS of $H_xSi_rN_zH_y$ film deposited under ECR-plasma conditions at substrate temperature $T = 100°C$ after 60 s of rapid annealing.

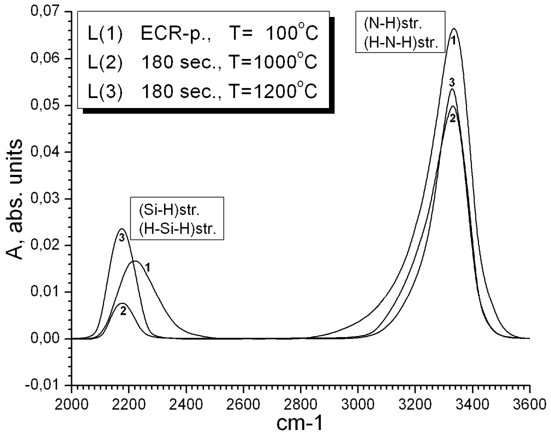

Figure 4. FTIRS of $H_xSi_rN_zH_y$ film deposited under ECR-plasma conditions at substrate temperature $T = 100°C$ after 180 s of rapid annealing .

$T = 1000°C$ and then increases from $T = 1000°C$ to $T = 1200°C$. FWHM decreases from 158 cm^{-1} at initial $T = 100°C$ to 103 cm^{-1} at $T = 1000°C$ and $T = 1200°C$.

The center of the (Si–H) band is displaced from 2220 cm^{-1} at initial $T = 100°C$ to 2170 cm^{-1} at $T = 1000°C$ and $T = 1200°C$. The C(N–H) decreases with increase of temperature from $T = 100°C$ to $T = 1000°C$ and then to $T = 1200°C$, and FWHM consistently decreases from 166 cm^{-1} to 130 cm^{-1}. The center of the (N–H) band remains at the same position, close to 3330 cm^{-1}.

In Fig. 5 is presented atomic concentration of the hydrogen connected to nitrogen (=NH and –NH_2 groups) in dependence on the temperature of rapid annealing. Integrated processing of FTIRS was used for calculation of C(N–H). The C(N–H) consistently decreased with increase in the annealing temperature.

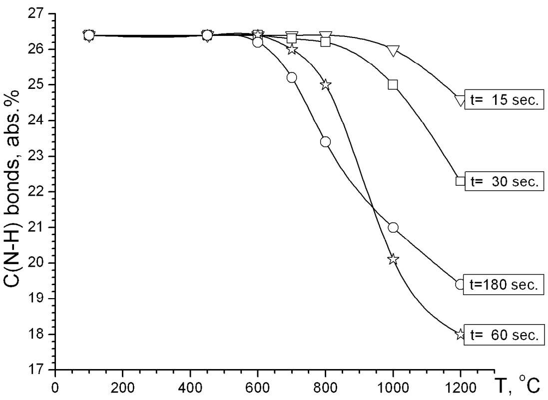

Figure 5. Atomic concentration of the hydrogen bonded to nitrogen as a function of temperature of rapid annealing of $H_xSi_rN_zH_y$ film (deposited in ECR-plasma, $T = 100°C$).

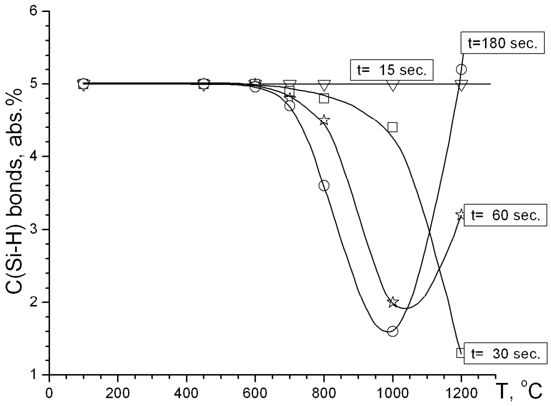

Figure 6. Atomic concentration of the hydrogen bonded to silicon as a function of temperature of rapid annealing of $H_xSi_rN_zH_y$ film (deposited in ECR-plasma, $T = 100°C$) .

In Fig. 6 is presented atomic concentration of the hydrogen connected to silicon ($\equiv$SiH and $=$SiH$_2$ groups) as a function of temperature of rapid annealing. Integrated processing of FTIRS was used to calculate C(Si–H). The C(Si–H) decreases from T = 700°C, and then shows paradoxically abrupt increase beginning from T = 1000°C.

We assume that this effect is determined by the complex kinetics of diffusion-controlled reactions in the solid phase. We also assume the existence of a large difference of the oscillator strengths constant between (Si–H) and (H–Si–H) stretching modes in the infrared spectra.

In Fig. 7 is presented FTIRS-area under the (Si–N–Si) + (N–Si–N) stretching bands (region from 700 cm^{-1} to 1100 cm^{-1}). Up to 1000°C, a weak increase from 31 units to 31.5 units is observed and then FTIRS-area decreases to 24.4 units at T = 1200°C in case of t = 180 s. We assume that after 1000°C under rapid thermal annealing of our low-temperature silicon nitrides destruction takes place according to equations (9) and (10).

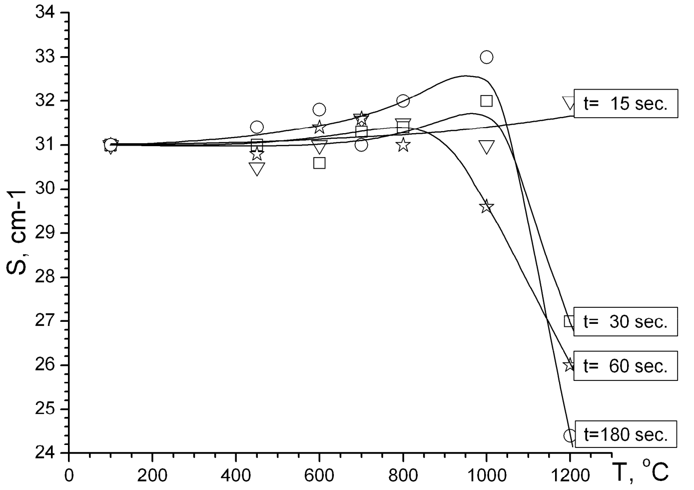

Figure 7. The area under the region from 700 cm^{-1} up to 1100 cm^{-1}.

5. Conclusion

Some theoretical aspects of the mechanism and kinetics of low-temperature silicon nitride thermal annealing were considered.

Four series of rapid thermal annealing experiments lasting $t = 15, 30, 60, 180$ s were carried out at six temperatures $T = 450, 600, 700, 800, 1000, 1200$°C for each series.

The observed reduction of the (Si–H) and (N–H) bonds under rapid annealing begins from the temperature T = 700°C, but then C(Si–H) shows a paradoxically sharp increase, beginning from T = 1000°C.

The results have shown good stability of (Si–N) bonds in $H_xSi_rN_zH_y$ film deposited under ECR-plasma conditions and substrate temperature T = 100°C. The observed reduction of the (Si–N) bonds under rapid annealing begins from the temperature T = 1000°C and then falls to 21 % at T = 1200°C and t = 180 s.

The electron cyclotron resonance (ECR) plasma method shares the advantages of the remote plasma system in view of low ion energy ($\sim$ 30 eV). Moreover, high plasma density ($\sim 10^{12}$ cm^{-3}) provides sufficient flows of the active species (i.e. :N., :N.$^+$, :SiH$_2$, :SiH$_2^+$,

:Si.H, :Si.H$^+$, :Si:, :SiP:$^+$) for deposition of high quality silicon nitrides at low or room temperatures, without performing a post-deposition processing.

More detailed calibration (with peak decomposition) of FTIRS integrated processing is necessary for calculation of C(Si–H) and C(N–H).

References

1. A. G. Aberle, Solar Energy Materials & Solar Cells **65**, 239 (2001).
2. A. G. Aberle, S. Glunz, W. Warta, J. Appl. Phys. **71**, 4422 (1996).
3. M. Wetter, Thin Solid Films **337**, 118 (1999).
4. Sanghoon Bae, David G. Farber, Stephen J. Fonash, Solid-State Electronics **44**, 1355 (2000).
5. Yu. Chetverov, S. Shapoval, Uncooled microbolometers based on microbridge structure technology, Lipki 2003.
6. G. Lucovsky, H. Niimi, Y. Wu, C. R. Parker, J. R. Hauser, J. Vac. Sci. Technol. A **16**, 1721 (1998).
7. G. Stubnya, I. C. Szep, G. Hoffmann, Rev. de Physique Appliquee, v. 13, 679 (1978).
8. M. Gupta, V. K. Rathi, R. Tangaraj, O. P. Agnihotri, Thin Solid Films **204**, 77 (1991).
9. T. P. Smirnova, L. V. Yakovkina, Thin Solid Films **293**, 6 (1997).
10. G. V. Gadiyak, V. G. Gadiyak, M. L. Kosinova, E. G. Salman, Thin Solid Films **335**, 19 (1998).

Journal of Research in Physics Vol. 31, No. 1, 47 - 53 (2007)

Looking for the Resonant States in High-temperature Superconductors with Impurities

K. Ivanović and Ž. Kovačević
Faculty of Natural Sciences and Mathematics, University of Montenegro,
P.O. Box 211, 81001 Podgorica, Montenegro
e-mail: krstoi@rc.pmf.cg.ac.yu, zarok@cg.ac.yu

Received: *March 8, 2007*

Abstract

A microscopic theory of resonant states for the Zn-doped CuO_2 plane in superconducting phase, formulated within the effective t-J model, was further applied to obtain local density of states (or differential conductance, measured by scanning tunneling microscopy) at the impurity site.

Key words: High temperature superconductivity, $t-J$ model, Zn-doped cuprates, scanning tunneling microscope

1. Introduction

There are a lot of experimental pieces of evidence indicating the increase of the local density of states (LDOS) near the Fermi level in Zn-doped cuprate superconductor, as $Bi_2Sr_2CaCu_2O_{8+\delta}$ (Bi-2212) compound [1, 2]. Using scanning tunneling microscopy (STM) in experimental research enabled the determination of local charge distribution on the atomic scale around the impurity site and study of the influence of impurities on superconducting state of cuprates.

In the [1] the authors studied the influence of Zn impurity on superconductivity in Bi-2212 crystal. Some very important conclusions can be made from their results. The samples used were Bi-2212 single crystals with 0.6 % partial substitution of Cu-atom with Zn-atom. They were characterized to have $T_c = 84$ K. In order to search for quasiparticle states, they measured differential conductance dI/dV for an area of approximately 50 nm × 50 nm at zero sample bias (i.e. near the Fermi level). Those measurements showed that there was large area of dark background, corresponding to low density of states (DOS) near the Fermi level, which was in accordance with the superconducting state. However, there were also observed some bright spots corresponding to high DOS. There exists a large discrepancy between STM spectra taken at those bright spots and at the superconducting area of the sample. There is a strong intra-gap peak near the Fermi level, whose magnitude can be up to six times greater than the normal-state conductance. The peak occurs not exactly at the Fermi energy, but at the energy of $-1,5 \pm 0,5$ meV. One of the main results was also that the first neighbours have no LDOS associated with them, while the second - and third - nearest neighbours coincide with LDOS maxima. It is also very important to notice the results concerning the spatial dependence of LDOS from the impurity site. LDOS does not decay monotonically, but rather decays with a distance r from the scattering centre.

In a search for the reason of the sharp resonance inside the superconducting gap, a lot of theoretical work has been done to find some model to explain how impurity affects the superconducting state [3-7].

In the recent papers [5, 6], an effective one-band t-J model in terms of the Hubbard operators for the $\mathrm{CuO_2}$ plane with Zn impurities has been derived. That Hamiltonian was further used to study s-, p- and d-wave contributions to the density of state (DOS) in the normal phase for the $\mathrm{CuO_2}$ plane with Zn impurities [6]. Generalizing the calculations for a superconducting phase of the proposed model, recently the s-, p- and d-wave contributions to the on-site LDOS $D(\omega, \mathbf{r})$ were calculated [7].

In this paper we present an analytical calculation of LDOS at the impurity (or vacancy, $i = 0$) site, which is proportional to the differential conductance measured in the STM experiments [1, 2].

The paper is organized as follows. In the Section 2 we introduce the model Hamiltonian and give the analytical solution for the contribution to the LDOS on Zn-atom. In Section 3 we present the results and propose three different paths for the numerical solution. Conclusions are given in Section 4.

2. Model and local density of states

In [7] an expression was derived for the additional contribution to the local density of states due to the presence of Zn-impurity. The influence of Zn-impurity on the superconducting state was investigated in the framework of the t-J model for $\mathrm{CuO_2}$ plane with vacant Cu-site [5, 6], i.e. $H = H_0 + V$, where

$$H_0 = H_{t-J} = \epsilon \sum_{i\sigma} X_i^{\sigma\sigma} + t \sum_{i\neq j,\sigma} X_i^{\sigma 0} X_j^{0\sigma} + \frac{1}{4} J \sum_{i\neq j,\sigma} (X_i^{\sigma\bar{\sigma}} X_j^{\bar{\sigma}\sigma} - X_i^{\sigma\sigma} X_j^{\bar{\sigma}\bar{\sigma}}), \tag{1}$$

with the vacancy contribution V_{vac} given by

$$V_{\mathrm{vac}} = -\epsilon \sum_{\sigma} X_0^{\sigma\sigma} - t \sum_{a\sigma} (X_0^{\sigma 0} X_a^{0\sigma} + \mathrm{H.c.}) - \frac{1}{4} J \sum_{a\sigma} (X_0^{\sigma\bar{\sigma}} X_a^{\bar{\sigma}\sigma} - X_0^{\sigma\sigma} X_a^{\bar{\sigma}\bar{\sigma}} + \mathrm{H.c.}). \tag{2}$$

Here $\epsilon = \epsilon_d - \mu$ is the energy of the hole, $t_{ij} = t$ is the hopping parameter for the nearest neighbours ($n.n.$) sites i, j in a square lattice and μ is the chemical potential. The summations in Eq. (2) are performed over the Cu-sites of the host square lattice, where the Zn-impurity is at the $i = 0$ site and $a = 1(a_x), 2(a_y), 3(-a_x), 4(-a_y)$ are the $n.n.$ sites.

Using the equation of motion method for Green's function (GF), one can calculate the DOS and LDOS [7]. As a consequence of the impurity scattering there appears the following additional contribution to the on-site local density of state (LDOS), which can be also separated in s-, p- and d-wave parts

$$\delta D^{(k)}(\omega, i) = -\frac{1}{\pi} \mathrm{Im}\{\delta G_{ii}^{(k)}(\omega + i\varepsilon)\}, \tag{3}$$

where δG is the additional GF contributions, i.e.

$$G_{ij} = G_{ij}^0 + \sum_{k=s,p,d} \delta G_{ij}^{(k)}, \tag{4}$$

explicit form is given in [7]. Here and in the sequel, the ω argument of GF will be omitted for shorteness.

3. Results and discussion

In the present paper we have focused on only one experimental result, i.e. the appearance of the differential conductance (dI/dV) sharp maximum for the energy (determined by bias voltage) near the Fermi level inside the superconducting gap [1] on the Zn-atom (or $i = 0$ lattice site). The differential conductance is proportional to the LDOS [3, 4], i.e.

$$\frac{dI}{dV} \propto \delta D^{(d)}(\omega, i=0) = -\frac{1}{\pi}\mathrm{Im}\,\delta G_{00}^{(d)}(\omega + i\varepsilon) \tag{5}$$

According to the symmetry analysis method of the irreducible representation (IR) group theory, it was obtained [7] that there is only d-wave nonzero contribution to the LDOS at the impurity site (denoted as $i = 0$) given as

$$\delta G_{00}^{(d)} = \frac{1}{D_d}\{\tilde{M}_d^{11}(G_{00}^0)^2 + 2(\tilde{M}_d^{12} + \tilde{M}_d^{21})G_{00}^0 G_{01}^0 + \frac{9}{2}\tilde{M}_d^{22}(G_{01}^0)^2\}, \tag{6}$$

where the zero order superconducting phase GF's, G_{ab}^0, are given in Appendix, and where the d-wave determinant D_d is given by

$$D_d = 1 - V'_{00}G_{00}^0 - V'_{11}\sum_a G_{a1}^0 - 4V'_{01}G_{01}^0 - 4V'_{10}G_{01}^0 + [V'_{00}V'_{11} - (2V'_{01})^2][d_{00}d_{11} - (d_{01})^2] \tag{7}$$

with the matrix elements of the square block diagonal zero order GF in the superconducting phase given as

$$d_{00} = G_{00}^0,\ d_{01} = 2G_{01}^0,\ d_{10} = 2G_{01}^0,\ d_{11} = \sum_a G_{a1}^0. \tag{8}$$

In the normal phase [6], the local static perturbation induced by vacancy, after applying T-matrix method, get the form of the square perturbation matrix, whose elements are not ω-independent denoted by V_{ab}, where $(a, b) = (0, 1)$. In the superconducting phase, as derived in [7], the perturbation matrix is denoted by V', which in addition to the static perturbation V, contains also dynamical ω-dependent parts $\Phi(\omega)$, i.e.

$$\begin{aligned} V'_{00} &= V_{00} + \Phi_d^{11}(\omega), \quad 2V'_{01} = 2V_{01} + \Phi_d^{12}(\omega), \\ 2V'_{10} &= 2V_{01} + \Phi_d^{21}(\omega), \quad V'_{11} = V_{11} + \Phi_d^{22}(\omega), \end{aligned} \tag{9}$$

with the explicit form given in Ref. [7]. Expanded form od D_d is given in Appendix.

The elements of the partial d-wave scattering matrix are

$$\begin{aligned} \tilde{M}_d^{11} &= V'_{00} - d_{00}V'^2_{00} - 2d_{01}V'_{10}V'_{00} + 2d_{01}V'_{01}V'_{00} + 4d_{11}V'_{01}V'_{10}, \\ \tilde{M}_d^{12} &= 2V'_{00}d_{00}V'^2_{01} + d_{01}V'_{11}V'_{00} + 2V'_{01} - (2V'_{01})^2 d_{10} - 2d_{11}V'_{01}V'_{11}, \\ \tilde{M}_d^{21} &= 2V'_{10} - 2d_{00}V'^2_{10}V'_{00} - (2V'_{10})^2 d_{01} + d_{10}V'_{11}V'_{00} + 2d_{11}V'_{11}V'_{10}, \\ \tilde{M}_d^{22} &= 2V'_{00}d_{10}V'^2_{10} + V'_{11} - 2d_{10}V'_{01}V'_{11} - d_{11}(V'_{11})^2. \end{aligned} \tag{10}$$

The expanded form of matrix elements $\tilde{M}_d^{11}, \tilde{M}_d^{12}, \tilde{M}_d^{21}$ and $\tilde{M}_d^{22}$ is given in Appendix.

Since we only need to show the existence of a peak inside the energy gap, we do not need to calculate numerically the complete expression. As can be seen from Eqs. (5) and (6), we must find the imaginary part of the complex number quotient, i.e.

$$\mathrm{Im}\frac{M}{D_d} = \frac{(\mathrm{Im}M)(\mathrm{Re}D_d) - (\mathrm{Re}M)(\mathrm{Im}D_d)}{(\mathrm{Im}D_d)^2 + (\mathrm{Re}D_d)^2} \tag{11}$$

and according to (6) we have $M = \{\tilde{M}_d^{11}(G_{00}^0)^2 + 2(\tilde{M}_d^{12} + \tilde{M}_d^{21})G_{00}^0 G_{01}^0 + \frac{9}{2}\tilde{M}_d^{22}(G_{01}^0)^2\}$.

In order to show that $\mathrm{Im}\,(M/D_d)$ goes to infinity, it is enough to show when $\omega \to V$ that $\mathrm{Im}\,M \to \infty$, and $\mathrm{Im}\,D_d$ are not singular or, as another way, that $\mathrm{Im}\,D_d = 0$ and $\mathrm{Im}\,M \neq 0$. The latter option seems more simple for numerical calculation.

4. Conclusion

In this paper we considered the microscopic model for the Zn-doped $\mathrm{CuO_2}$ plane, derived in the papers [5-7], in order to obtain local density of states. It is proportional to the differential conductivity dI/dV, measured by the scanning tunneling microscopy [1, 2]. We expressed the local density of states at the impurity (or vacancy) site, using the GF in normal and superconducting state. There appears also the renormalized hopping parameter and on-site energy which can be used as fitting parameters. Theory of impurity effect derived in [5-7] has advantage in comparison with recent semiphenomenological theories (as, for example [3, 4]). In the latter ones there was not included the fact that any disturbance of the strong electron correlation host lattice induces frequency (ω) dependent scattering potential contribution. We expect that it should be important to understand reason for such detrimental impurity influence to superconductivity. Numerical calculation should be performed in further work, and will be published elsewhere.

The experiments [1, 2] gave no LDOS contribution to the first neighbours ($n.n.$) to the Zn site. Using the results from [7], we can obtain the corresponding expanded form for LDOS on the first and second neighbours to impurity (or vacancy) site. It would be an interesting task to make a comparison with the experimental results.

5. Appendix

In this section we give some useful equations and expanded form of the expressions for the quantities needed for the numerical calculations.

5.1 Green's functions for the ideal lattice

Fourier transformation (F.T.) of the real space GF can be written in the following form

$$G_{ij}(\omega) = \frac{1}{N}\sum_{\mathbf{q}} G(\mathbf{q},\omega)\cos[\mathbf{q}(\mathbf{i}-\mathbf{j})]. \tag{12}$$

For the normal phase ideal-lattice F.T. of the GF is

$$G^{0,n}(\mathbf{q},\omega) = \frac{1}{\omega - \epsilon(\mathbf{q})}, \tag{13}$$

where the quasi-particle spectrum in the normal phase is given by $\epsilon(\mathbf{q}) = (1/2)(\cos q_x + \cos q_y)$, and the energy is measured in the units of half bandwith.

The corresponding ideal-lattice F.T. of the GF in the superconducting phase can be written as:

$$G^0(q,\omega) = \frac{\omega + \epsilon(\mathbf{q})}{\omega^2 - E_\sigma^2(\mathbf{q})} = u_\mathbf{q}^2 \frac{1}{\omega - E_\sigma(\mathbf{q})} + v_\mathbf{q}^2 \frac{1}{\omega + E_\sigma(\mathbf{q})} \tag{14}$$

where we introduce quasi-particle energy $E_\sigma(\mathbf{q}) = \sqrt{\epsilon(\mathbf{q})^2 + \Delta_\sigma(\mathbf{q})^2}$ and the Bogolubov's particle-hole parameters:

$$u_\mathbf{q}^2 = \frac{1}{2}\{1 + \frac{\epsilon(\mathbf{q})}{E_\sigma(\mathbf{q})}\}, \qquad v_\mathbf{q}^2 = \frac{1}{2}\{1 - \frac{\epsilon(\mathbf{q})}{E_\sigma(\mathbf{q})}\}.$$

5.2 Expanded form of the d-wave determinant D_d

Using Eqs. (7) and (9) and the corresponding Eqs. from Ref. [6, 7], one obtains the following expanded form of D_d :

$$\begin{aligned} D_d \;=\; & 1 - \frac{1}{4}(G_{11}^0 + G_{21}^0 + G_{31}^0 + G_{41}^0)\{3\delta\epsilon + [-32\tilde{t} + 8\omega\delta\epsilon]G_{00}^{0,n}(-\omega) + 4[\tilde{\epsilon} + \\ & \omega(-8\tilde{t} + \omega\delta\epsilon)][G_{00}^{0,n}(-\omega)]^2\} - \{-\tilde{\epsilon} + 4[\tilde{\epsilon} + \omega(-8\tilde{t} + \omega\delta\epsilon)]\{1 + \omega G_{00}^{0,n}(-\omega)\}^2\}G_{00}^0 \\ & -8G_{01}^0\{3\tilde{t} - \omega\delta\epsilon - [\tilde{\epsilon} + 2\omega(-6\tilde{t} + \omega\delta\epsilon)] \cdot [G_{00}^{0,n}(-\omega)] - \omega(\tilde{\epsilon} + \omega(-8\tilde{t} + \omega\delta\epsilon) \\ & [G_{00}^{0,n}(-\omega)]^2\} - \frac{1}{4}\{144\tilde{t}^2 + \delta\epsilon(-9\tilde{\epsilon} + 4\omega^2\delta\epsilon) + 8\omega[16\tilde{t}^2 + \delta\epsilon(-2\tilde{\epsilon} + \omega^2\delta\epsilon)]G_{00}^{0,n}(-\omega) \\ & +4(\tilde{\epsilon} - \omega^2\delta\epsilon)^2[G_{00}^{0,n}(-\omega)]^2\}\{G_{11}^0 G_{00}^0 + G_{21}^0 G_{00}^0 + G_{31}^0 G_{00}^0 + G_{41}^0 G_{00}^0 - 4(G_{01}^0)^2\} \end{aligned} \tag{15}$$

where the argument for each of the normal phase GF is $(-\omega)$ is explicitly written, i.e. $G_{ij}^{0,n}(-\omega)$ and the argument for each of the superconducting phase GF is ω, and is omitted because of shorteness. As was derived in Ref. [6], normal phase ideal lattice GF can be expessed in the form of the complete elliptic integrals of the first and second kind. Namely, for the $\omega > 1$ in the units of the half bandwidth, one has

$$G_{00}^{0,n}(-\omega) = J_{00}(-\omega) = \frac{1}{-\omega}\tilde{K}(\frac{1}{-\omega}) = \tilde{K}(-\omega) + i\tilde{K}(\sqrt{1-\omega^2}), \tag{16}$$

where the complete elliptic integral of the first kind is

$$\tilde{K}(k) \equiv F(\pi/2, k) = \int_0^1 \frac{d\omega}{\sqrt{(1-x^2)(1-k^2x^2)}}.$$

As a consequence of the strong electron correlation, i.e. the kinematic and exchange interactions, the hopping energy $\tilde{t}$ and the on-site energy $\tilde{\epsilon} = \epsilon + \delta\epsilon$ are renormalized in the generalized mean field approximation. The explicit form of $\tilde{t}$ and $\delta\epsilon$ is given in Ref. [6] and here will be used as the fitting parameters.

5.3 Expanded form of the V' matrix elements

Using (9) and the corresponding Eqs. from Ref. [6, 7], one obtains the following expanded form of the V' matrix elements

$$\begin{aligned} V'_{00} &= -\tilde{\epsilon} - (32\tilde{t}\omega - 4\tilde{\epsilon} - 4\delta\epsilon\omega^2)((\omega G_{00}^{0,n}(-\omega) + 1)^2) \\ V'_{01} &= (-\tilde{t} - \omega\delta\epsilon + 4\tilde{t}) - (-12\omega\tilde{t} + 2\delta\epsilon\omega^2 + \tilde{\epsilon})G_{00}^{0,n}(-\omega) - (\epsilon\omega - 8\tilde{t}\omega^2 + \delta\epsilon\omega^3)G_{00}^{0,n}(-\omega)^2 \\ V'_{10} &= (-\tilde{t} - \omega\delta\epsilon + 4\tilde{t}) - (-12\omega\tilde{t} + 2\delta\epsilon\omega^2 + \tilde{\epsilon})G_{00}^{0,n}(-\omega) - (\epsilon\omega - 8\tilde{t}\omega^2 + \delta\epsilon\omega^3)G_{00}^{0,n}(-\omega)^2 \\ V'_{11} &= \frac{3\delta\epsilon}{4} - (8\tilde{t} - 2\omega\delta\epsilon)G_{00}^{0,n}(-\omega) - (8\omega\tilde{t} - \tilde{\epsilon} - \omega^2\delta\epsilon)G_{00}^{0,n}(-\omega)^2 \end{aligned} \tag{17}$$

5.4 Expanded form of matrix elements $\tilde{M}_d^{ab}$

Using (10) and the corresponding Eqs. from Ref. [6, 7], one obtains the following expanded form of the matrix elements $\tilde{M}_d^{ab}, \tilde{M}_d^{12}, \tilde{M}_d^{21}$ and $\tilde{M}_d^{22}$ as follows

$$
\begin{aligned}
\tilde{M}_d^{11} \; = \; & -\tilde{\epsilon} + 4[\tilde{\epsilon} + \omega(-8\tilde{t} + \omega\delta\epsilon)](1 + \omega G_{00}^{0,n}(-\omega))^2 + 4[G_{11}^0 + G_{21}^0 + G_{31}^0 + G_{41}^0][-3\tilde{t} \\
& +\omega\delta\epsilon + (\tilde{\epsilon} + 2\omega(\omega\delta\epsilon - 6\tilde{t}))G_{00}^{0,n}(-\omega) + \omega(\tilde{\epsilon} + \omega(\omega\delta\epsilon - 8\tilde{t}))G_{00}^{0,n}(-\omega)^2]^2 - \\
& [\tilde{\epsilon} - 4(\tilde{\epsilon} + \omega(\omega\delta\epsilon - 8\tilde{t}))(1 + \omega G_{00}^{0,n}(-\omega))^2]^2 G_{00}^0 \\
\\
\tilde{M}_d^{12} \; = \; & 2\{3\tilde{t} - \omega\delta\epsilon - [\tilde{\epsilon} + 2\omega(\omega\delta\epsilon - 6\tilde{t})]G_{00}^{0,n}(-\omega) - \omega[\tilde{\epsilon} + \omega(\omega\delta\epsilon - 8\tilde{t})]G_{00}^{0,n}(-\omega)^2 + \\
& \frac{1}{4}[G_{11}^0 + G_{21}^0 + G_{31}^0 + G_{41}^0][3\delta\epsilon + (-32\tilde{t} + 8\omega\delta\epsilon)G_{00}^{0,n}(-\omega) + 4(\tilde{\epsilon} + \omega(\omega\delta\epsilon - 8\tilde{t})) \\
& G_{00}^{0,n}(-\omega)^2][-3\tilde{t} + \omega\delta\epsilon + [\tilde{\epsilon} + 2\omega(\omega\delta\epsilon - 6\tilde{t})]G_{00}^{0,n}(-\omega) + \omega[\tilde{\epsilon} + \omega(\omega\delta\epsilon - 8\tilde{t})]G_{00}^{0,n} \\
& (-\omega)^2] + [-3\tilde{t} + \omega\delta\epsilon + [\tilde{\epsilon} + 2\omega(\omega\delta\epsilon - 6\tilde{t})]G_{00}^{0,n}(-\omega) + \omega[\tilde{\epsilon} + \omega(\omega\delta\epsilon - 8\tilde{t})]G_{00}^{0,n} \\
& (-\omega)^2]^2[-\tilde{\epsilon} + 4(\tilde{\epsilon} + \omega(\omega\delta\epsilon - 8\tilde{t}))(1 + \omega G_{00}^0(-\omega))^2]G_{00}^0 - 4[-3\tilde{t} + \omega\delta\epsilon + [\tilde{\epsilon} + \\
& 2\omega(\omega\delta\epsilon - 6\tilde{t})]G_{00}^{0,n}(-\omega) + \omega[\tilde{\epsilon} + \omega(\omega\delta\epsilon - 8\tilde{t})]G_{00}^{0,n}(-\omega)^2]^2 G_{01}^0 + [\frac{3\delta\epsilon}{4} + (-8\tilde{t} \\
& +2\omega\delta\epsilon)G_{00}^{0,n}(-\omega) + (\tilde{\epsilon} + \omega(\omega\delta\epsilon - 8\tilde{t}))G_{00}^{0,n}(-\omega)^2][-\tilde{\epsilon} + 4(\tilde{\epsilon} + \omega(\omega\delta\epsilon - 8\tilde{t}))(1 \\
& +\omega G_{00}^{0,n}(-\omega))^2]G_{01}^0\} \\
\\
\tilde{M}_d^{21} \; = \; & 2\{3\tilde{t} - \omega\delta\epsilon - [\tilde{\epsilon} + 2\omega(\omega\delta\epsilon - 6\tilde{t})]G_{00}^{0,n}(-\omega) - \omega[\tilde{\epsilon} + \omega(\omega\delta\epsilon - 8\tilde{t})]G_{00}^{0,n}(-\omega)^2 \\
& -\frac{1}{4}[G_{11}^0 + G_{21}^0 + G_{31}^0 + G_{41}^0][3\delta\epsilon + (-32\tilde{t} + 8\omega\delta\epsilon)G_{00}^{0,n}(-\omega) + 4(\tilde{\epsilon} + \omega(\omega\delta\epsilon - 8\tilde{t})) \\
& G_{00}^{0,n}(-\omega)^2][-3\tilde{t} + \omega\delta\epsilon + [\tilde{\epsilon} + 2\omega(\omega\delta\epsilon - 6\tilde{t})]G_{00}^{0,n}(-\omega) + \omega[\tilde{\epsilon} + \omega(\omega\delta\epsilon - 8\tilde{t})]G_{00}^{0,n} \\
& (-\omega)^2] - [-3\tilde{t} + \omega\delta\epsilon + [\tilde{\epsilon} + 2\omega(\omega\delta\epsilon - 6\tilde{t})]G_{00}^{0,n}(-\omega) + \omega[\tilde{\epsilon} + \omega(\omega\delta\epsilon - 8\tilde{t})]G_{00}^{0,n} \\
& (-\omega)^2]^2[-\tilde{\epsilon} + 4(\tilde{\epsilon} + \omega(\omega\delta\epsilon - 8\tilde{t}))(1 + \omega G_{00}^0(-\omega))^2]G_{00}^{0,n} - 4[-3\tilde{t} + \omega\delta\epsilon + [\tilde{\epsilon} + \\
& 2\omega(\omega\delta\epsilon - 6\tilde{t})]G_{00}^{0,n}(-\omega) + \omega[\tilde{\epsilon} + \omega(\omega\delta\epsilon - 8\tilde{t})]G_{00}^{0,n}(-\omega)^2]^2 G_{01}^0 + [\frac{3\delta\epsilon}{4} + (-8\tilde{t} + \\
& 2\omega\delta\epsilon)G_{00}^{0,n}(-\omega) + (\tilde{\epsilon} + \omega(\omega\delta\epsilon - 8\tilde{t}))G_{00}^{0,n}(-\omega)^2][-\tilde{\epsilon} + 4(\tilde{\epsilon} + \omega(\omega\delta\epsilon - 8\tilde{t}))(1 + \\
& \omega G_{00}^{0,n}(-\omega))^2]G_{01}^0\} \\
\\
\tilde{M}_d^{22} \; = \; & \frac{3\delta\epsilon}{4} - 2[4\tilde{t} - \omega\delta\epsilon]G_{00}^{0,n}(-\omega) + [\tilde{\epsilon} + \omega(\omega\delta\epsilon - 8\tilde{t})]G_{00}^{0,n}(-\omega)^2 - \frac{1}{16}[G_{11}^0 + G_{21}^0 + G_{31}^0 \\
& +G_{41}^0]\{3\delta\epsilon + [-32\tilde{t} + 8\omega\delta\epsilon]G_{00}^{0,n}(-\omega) + 4[\tilde{\epsilon} + \omega(\omega\delta\epsilon - 8\tilde{t})]G_{00}^{0,n}(-\omega)^2\}^2 + 4\{\frac{3\delta\epsilon}{4} \\
& +[-8\tilde{t} + 2\omega\delta\epsilon]G_{00}^{0,n}(-\omega) + [\tilde{\epsilon} + \omega(\omega\delta\epsilon - 8\tilde{t})]G_{00}^{0,n}(-\omega)^2\}\{3\tilde{t} - \omega\delta\epsilon - [\tilde{\epsilon} + 2\omega(\omega\delta\epsilon \\
& -6\tilde{t})]G_{00}^{0,n}(-\omega) - \omega[\tilde{\epsilon} + \omega(\omega\delta\epsilon - 8\tilde{t})]G_{00}^{0,n}(-\omega)^2\}G_{01}^0 + 4\{-3\tilde{t} + \omega\delta\epsilon + [\tilde{\epsilon} + 2\omega \\
& (\omega\delta\epsilon - 6\tilde{t})]G_{00}^{0,n}(-\omega) + \omega[\tilde{\epsilon} + \omega(\omega\delta\epsilon - 8\tilde{t})]G_{00}^{0,n}(-\omega)^2\}^2\{-\tilde{\epsilon} + 4[\tilde{\epsilon} + \omega(\omega\delta\epsilon - 8\tilde{t})] \\
& [1 + \omega G_{00}^{0,n}(-\omega)]^2\}G_{01}^0
\end{aligned}
\tag{18}
$$

Acknowledgments

Authors thank the Faculty of Natural Sciences, University of Montenegro for support. Partial financial support by the 'Superconductors: theoretical and experimental investigations of the thermodinamical and transport behaviour' project program is acknowledged.

References

1. S. H. Pan, E. W. Hudson, K. M. Lang, H. Eisaki, S. Uchida and J. C. Davis, Nature **403**, 746 (2000).
2. E. W. Hudson, K. M. Lang, V. Madhavan, S. H. Pan, H. Eisaki, S. Uchida and J. C. Davis, Nature **411**, 920 (2001).
3. J. M. Tang and M. E. Flatté, Phys. Rev. B **70**, 140510(R) (2004).
4. S. Haas and K. Maki, Phys. Rev. Lett. **85**, 2172 (2000).
5. Ž. Kovačević, R. Hayn and N. M. Plakida, Eur. Phys. J. B **10**, 487 (1999).
6. Ž. Kovačević, I. Chaplygin, R. Hayn and N. M. Plakida, Eur. Phys. J. B **18**, 377 (2000).
7. Ž. Kovačević, N. M. Plakida and R. Hayn, Theor. Math. Phys. **136**, 1155 (2003).

Journal of Research in Physics Vol. 31, No. 1, 55 - 60 (2007)

Study of the Composition Homogeneity of Amorphous Thin Films from the System Cu-As-S-Se by Scanning Electron Microscopy

D. D. Štrbac[1], S. R. Lukić[2], D. M. Petrović[2], G. R. Štrbac[2],
J. M. Gonzalez-Leal[3], A. Srinivasan[4]
[1]*Faculty of Technical Sciences, University of Novi Sad, Novi Sad, Serbia*
[2]*Faculty of Sciences, University of Novi Sad, Novi Sad, Serbia*
[3]*Departamento de Fisica de la Materia Condensada, Facultat de Ciencias, Cadiz, Spain*
[4]*Department of Physics, Indian Institute of Technology, Guwahati, India*
e-mail: gaca@uns.ns.ac.yu

Received: *May 10, 2007*

Abstract

The paper describes the analysis of the composition homogeneity and thickness uniformity of samples of thin amorphous chalcogenide films from the system $\mathrm{Cu}_x[\mathrm{As}_2(\mathrm{S}_{0.5}\mathrm{Se}_{0.5})_3]_x$ for $x = 0$ at% and 0.5 at% using scanning electron microscopy method. Besides, a quantitative analysis was carried out of the obtained spectrum, that is the calculation of mass and atomic fractions of the identified components in the spectrum of the investigated system thin film plus glass substrate. It was found that the investigated samples are of homogeneous composition, uniform thickness and devoid of surface irregularaties.

Key words: Thin films, chalcogenides, SEM

1. Introduction

Thin amorphous chalcogenide films represent a type of materials that have attracted great attention of researchers in the recent decades, primarily because of their various applications related to optical memory, sensors, optical communication systems, and the like [1]. A main shortcoming of these systems is the difficulty of ensuring the reproducibility of their properties. Namely, the critical issues are the preparation of thin films of the same composition as the starting bulk glass, the inhomogeneity of the films, the nonuniformity of their thickness, and the presence of surface irregularaties. In order to overcome these shortcomings, intensive studies have been made with the aim of finding new and better film preparation techniques [2]. Still, for any practical application, it is necessary to check out the composition, homogeneity and uniformity of each particular sample.

2. Methodology

Thin amorphous chalcogenide films of the type $\mathrm{Cu}_x[\mathrm{As}_2(\mathrm{S}_{0.5}\mathrm{Se}_{0.5})_3]_{100-x}$ were prepared by thermal evaporation in vacuum of the previously synthesized bulk samples. Films were deposited on the glass substrates, standard microscopic glass slides, 0.14 mm thick.

The synthesis of the glasses from this series was carried out by employing the regime of cascade heating of high-purity (99.998 %) elementary components and cooling in the air. Detailed time-temperature diagrams have been presented in previous article [3]. The bulk samples were powdered and thermal evaporation under a pressure of 10^{-5} Torr was employed to prepare the samples in the form of thin films. During the evaporation, the glass substrate was cooled with liquid nitrogen, to prevent formation of crystalline centers in the film [4]. The substrate temperature was controlled with the aid of a calibrated PT100 sensor.

The analysis of sample homogeneity and quantitative analysis of the samples (for $x = 0$ at% and 0.5 at% Cu) was performed by scanning electron microscopy (SEM) method on a Quanta 200 instrument of FEI Company, which works on the principles of EDAX technique.

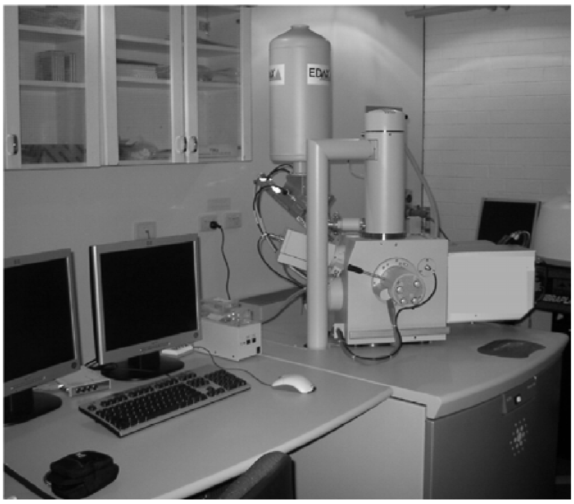

Figure 1. Quanta 200 SEM.

The Quanta 200 is a scanning electron microscope which works under high-vacuum conditions. It enables scanning of the sample and obtaining data without any previous preparation, while diminishing no the resolution (Figure 1). The controlled conditions provided by the Quanta 200 instrument include variations of pressure and temperature of taking recordings. For controlling the working conditions and automatic treatment of signals from Quanta 200 use was made of the software "Genesis Spectrum", which enabled the adjustment of the working voltage, identification of peaks, selection of peak positions that will be marked in advance for an easier identification of the expected elements, noise elimination, etc. This software also enabled a quantitative analysis of the obtained spectrum, that is the calculation of the mass and atomic fractions of the particular components in the spectrum of the investigated sample.

In Figure 2 is presented a typical screen display obtained in the quantitative analysis using the "Genesis Spectrum" software for treatment of data from the scanning electron microscope.

The same software served to perform a qualitative analysis of the composition of the investigated system film + substrate, as well as its quantitative evaluation (Figure 3).

3. Results and discussion

In Figure 4 are shown results of the SEM recording for the chalcogenide thin film without copper, prepared on a thin glass substrate (standard microscopic glass slides). The selected samples were prepared this way in order to minimize the effect of the substrate on the obtained results. Namely, the lower limit of detection of the system is 1 at% in the overall investigated system thin film + substrate, so that for those elements whose content in the film composition is low, the possibility of detection/determination is determined by

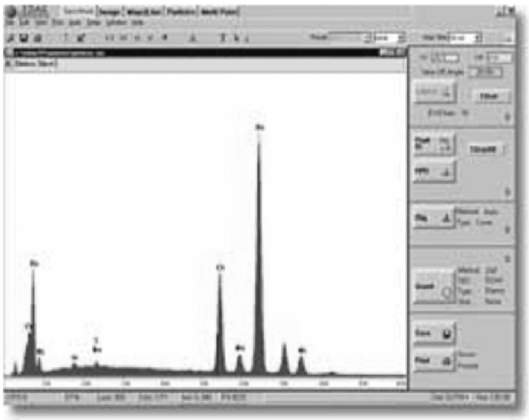

Figure 2. Tipical screen display obtained in the qualitative analysis using the "Genesis Spectrum" software for treatment of data from the SEM instrument.

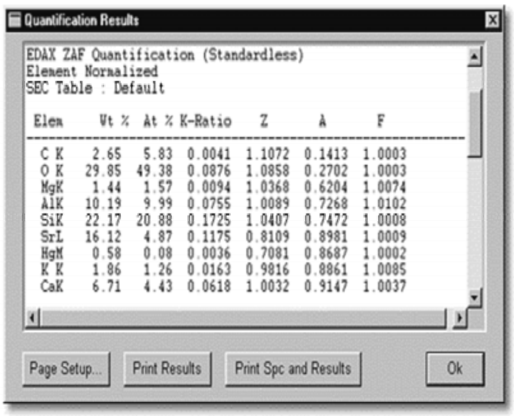

```
EDAX ZAF Quantification (Standardless)
Element Normalized
SEC Table : Default

 Elem     Wt %   At % K-Ratio    Z       A       F
------------------------------------------------------------
  C K     2.65   5.83  0.0041  1.1072  0.1413  1.0003
  O K    29.85  49.38  0.0876  1.0858  0.2702  1.0003
  MgK     1.44   1.57  0.0094  1.0368  0.6204  1.0074
  AlK    10.19   9.99  0.0755  1.0089  0.7268  1.0102
  SiK    22.17  20.88  0.1725  1.0407  0.7472  1.0008
  SrL    16.12   4.87  0.1175  0.8109  0.8981  1.0009
  HgM     0.58   0.08  0.0036  0.7081  0.8687  1.0002
  K K     1.86   1.26  0.0163  0.9816  0.8861  1.0085
  CaK     6.71   4.43  0.0618  1.0032  0.9147  1.0037
```

Figure 3. Software screen presenting quantification of the results of SEM analysis.

the thickness of the substrate.

As can be seen, the SEM analysis confirmed the presence of arsenic, sulfur an selenium in the investigated samples. Apart from these elements it was also possible to detect silicium, oxygen, sodium, potassium and titanium, which are common components of the standard microscopic slides, so that the identification of these elements is related to the substrate material.

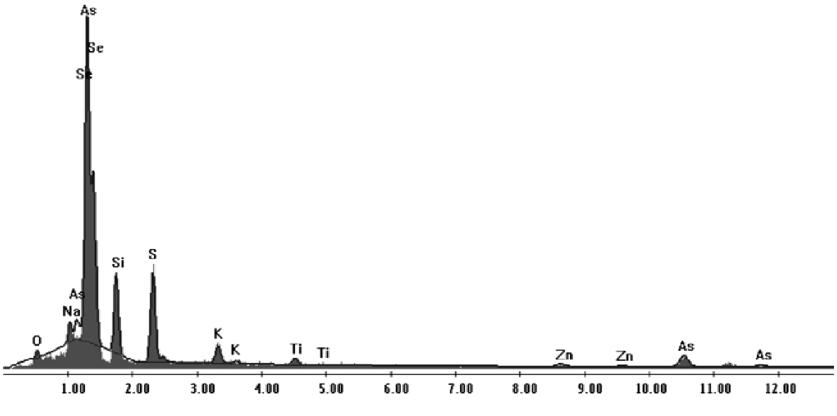

Figure 4. Results of SEM measurements for the sample with 0 at% Cu.

In Table 1 are presented results of the quantiative SEM analysis of the sample with 0 at% Cu. The results are expressed as weight percentages (*wt%*) and atomic percentages (*at%*). The fractions are given with respect to the composition of the overall system sample + glass.

Table 1. Results of the quantitative SEM analysis of the sample with 0 at% Cu.

$As_2(S_{0.5}Se_{0.5})_3$		
Chemical element [*line*]	wt (%)	at (%)
O [*K*]	2.41	7.32
Na [*K*]	1.91	4.03
Se [*L*]	38.12	23.42
Si [*K*]	13.30	22.97
S [*K*]	12.98	19.63
K [*K*]	2.73	3.38
Ti [*K*]	1.34	1.36
Zn [*K*]	3.01	2.23
As [*K*]	24.18	15.65
total	100.00	100.00

As can be seen from the tables, the calculation of the ratios of a particular component was based on the K and L lines in the spectrum, that is the lines that could be discerned for the given element. However, it should be pointed out that the technique itself and the appearance of the obtained spectra were limiting factors that partly hindered taking into account all the lines from the spectrum in the calculation of atomic fractions. Namely, it was possible that in some cases there occurred overlapping of the lines that belonged to the different elements. The deviations from the expected atomic fractions may be in fact a consequence of these overlappings.

Results of the SEM analysis for the sample with 0.5 at% Cu are shown in Figure 5. As with the previous sample, it was possible to confirm the presence of As, S and Se, as well as of the elements from the substrate.

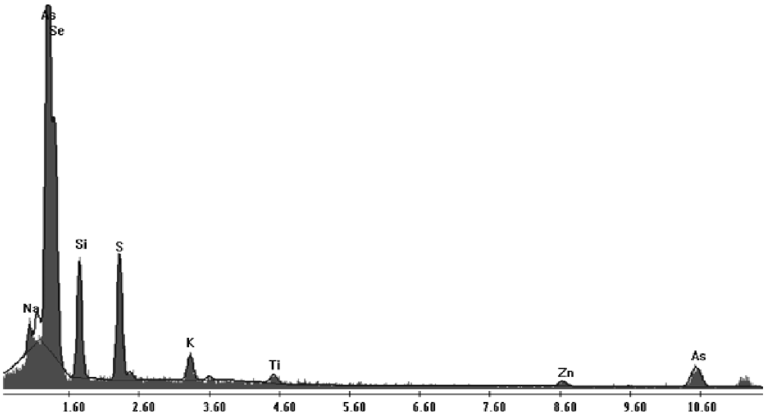

Figure 5. Results of SEM measurements for the sample with 0.5 at% Cu.

Results of the quantitative SEM measurements for the sample with 0.5 at% Cu are presented in Table 2.

Table 2. Results of the quantitative SEM analysis of the sample with 0.5 at% Cu.

$Cu_{0.5}[As_2(S_{0.5}Se_{0.5})_3]_{99.5}$		
Chemical element [*line*]	wt (%)	at (%)
O [*K*]	2.78	8.50
Na [*K*]	1.58	3.35
Se [*L*]	36.21	22.39
Si [*K*]	13.23	23.00
S [*K*]	12.03	18.32
K [*K*]	2.46	3.07
Ti [*K*]	1.25	1.27
Zn [*K*]	2.69	2.01
As [*K*]	27.77	18.10
total	100.00	100.00

Atomic fractions of As, S an Se in the samples with 0 at% Cu and 0.5 at% Cu are approximately close to the atomic fractions in the starting bulk samples from which the films were prepared. As can be seen from Table 3, for both investigated samples, the expected ratios of the components in the thin film are approximately:

$$(\text{at\% (As)}) : (\text{at\% (S)}) : (\text{at\% (Se)}) = 2 : 1.5 : 1.5.$$

Evidently, the mass fractions, based on the determined atomic ratios and relative atomic masses of the elements, follow the expected ratios.

It can also be seen from Table 3 that the atomic fraction of copper in the thin film, and especially its relative ratio in the system film + substrate, is below the detection limit of the system, so that the copper presence could not be detected.

Table 3. Atomic fractions of the components in the bulk samples.

Sample	at% (As)	at% (S)	at% (Se)	at% (Cu)
$As_2(S_{0.5}Se_{0.5})_3$	40	30	30	0
$Cu_{0.5}[As_2(S_{0.5}Se_{0.5})_3]_{99.5}$	39.96	29.97	29.97	0.10

4. Conclusion

The method of scanning electron microscopy was used to test the composition homogeneity and thickness uniformity of thin-film samples of chalcogenide glasses from the system $Cu_x[As_2(S_{0.5}Se_{0.5})_3]_x$ for $x = 0$ at% and 0.5 at%. Scanning of the surfaces of investigated samples showed no presence of inhomogeneity or thickness variation. The analysis of sample composition at different points on the surface gave the same results. Thus, it was established that the samples were of homogeneous composition and uniform thickness, with no surface irregularities. Quantitative analysis of the obtained spectra, that is the calculation of mass and atomic fractions of the identified components in the spectrum of the investigated system film + glass substrate, was also carried out. It appeared that the ratios of the components in a thin-film sample deviated slightly from the ratios of components in the bulk sample from which the film was prepared. The method allowed the determination in relation to the overall composition of the system sample + substrate and hence it cannot be used for the evaluation of absolute fractions in the film itself, but can only be useful in the sense of confirming the presence of expected elements in the thin-film composition. SEM showed that the investigated films were of good quality from the aspect of their practical application, as they are uniformly thick, homogeneous, and devoid of surface irregularaties. The deviations from the expected film composition with respect to the composition of the starting bulk samples from which films were prepared can be ascribed to the shortcomings of the technique of vacuum thermal evaporation.

Acknowledgments

This work was partly financed by the Ministry for Science and Environmental Protection of the Republic of Serbia, within the project "Amorphous and Nanostructural Chalcogenides"

References

1. A. Zackery, S. R. Eliot, J. Non-Cryst. Solids **330**, 1 (2003).
2. J. M. Gonzalez-Leal, M. Stuchlik, M. Vlcek, R. Jimenez-Garay, E. Marquez, App. Surf. Sci. **246**, 348 (2005).
3. Ž. N. Popović, D. M. Petrović, S. R. Lukić, M. M. Garić, S. J. Skuban, J. Optoel. Adv. Mat. **2**(3), 255 (2000).
4. A. K. Pattanaik, A. Srinivasan, J. Optoel. Adv. Mat. **5**(5), 1161 (2003).

Journal of Research in Physics Vol. 31, No. 1, 61 - 67 (2007)

Influence of Electrical Contacts on Measurement of Electrical Conductivity of Amorphous Semiconductors from the System Cu-As-Se-I

Miloš P. Slankamenac[1], Svetlana R. Lukić[2], Fedor Skuban[2],
Imre O. Gut[2], Miloš Živanov[1]
[1]*Faculty of Technical Sciences, University of Novi Sad, Novi Sad, Serbia*
[2]*Faculty of Sciences, University of Novi Sad, Novi Sad, Serbia*
e-mail: svetdrag@im.ns.ac.yu

Received: *May 10, 2007*

Abstract

The DC electrical conductivity of Cu-As-Se-I amorphous semiconductor glasses have been measured in the temperature range $300 - 410$ K. The paper describes results of the study of the influence of copper content and electrical contacts on measurement of electrical conductivity of glasses from the system $Cu_x(AsSe_{1.4}I_{0.2})_{100-x}$.

Key words: Chalcogenide glasses, electrical conductivity, conduction activation energy

1. Introduction

In the group of non-crystalline semiconducting materials a special place is occupied by chalcogenide amorphous semiconductors, i.e. the materials that contain one or more chalcogen elements: sulphur, selenium and tellurium [1].

They can be obtained in the form of glasses either as bulk amorphous samples, or in the form of thin films. The possibility of obtaining a large number of amorphous semiconductors of different composition, including also non-stoichiometric compounds and mixtures, have opened wide perspectives for the application of these materials.

Scientists have discovered a lot of new chalcogenide materials, phenomena and applications. Following the development of the glassy chalcogenide field, new optoelectronic materials based on halides have been discovered. Complex oxide and non-oxide glasses have been prepared and investigated in the last several decades, thus widening the groups of materials used in various optical, electronic and optoelectronic semiconductor glasses. The great advantages of the disordered materials are: simple preparation procedures, low sensitivity to impurities, high stability to the action of ionizing radiation, chemical stability towards the majority of aggressive chemical substances, low cost, and, the possibility to produce large area films of various thickness in classical systems for deposition: systems for evaporation in vacuum, magnetron systems, flash, spin-coating systems, sol-gel systems, etc [2].

Chalcogenide glassy semiconductors have a number of properties important for device application. They show continuous change of physical properties with change in chemical composition. A lot of work has been done on the impurity effect on conductivity and optical properties.

Electrical conductivity of semiconductor chalcogenide glasses is of a dominant electron nature and depends on the composition. It varies in a huge interval from 10^{-3} to 10^{-17} $\Omega^{-1}\text{cm}^{-1}$ in normal conditions. Glasses have electrical conductivity some orders of magnitude less than these crystal analogues. Optical energy gap has values in the interval from 0.8 to 3 eV and refractive index $1.8 - 3.5$ (for $\lambda = 1.06$ μm) [3]. A very important feature of semiconductor chalcogenide glasses is the specific influence of dopants on values and a type of electrical conductivity.

In view of the fact that the electrical conductivity of amorphous materials can be affected by the presence of defects in the structural network of semiconductor chalcogenide glasses and inserted transition metals, it is very interesting to investigate chalcogenide glassy semiconductors with Cu and Fe. It has been shown that obtaining of homogenous glassy semiconductors with transition metals is limited to relatively low density of metals [1]. Increasing the density of metals, thermal and mechanical properties do not change significantly, whereas electrical conductivity evinces high transition from semiconducting to metal type.

Based on numerous analysis and experimental data, it is concluded that chalcogenide glasses have intrinsic electrical conductivity and Fermi level is located near the middle of the energy gap [3].

Electrical conductivity of amorphous semiconductors depends on the synthesis, melt cooling rate, purity of the starting components, thermal treatment, and other factors [4]. With the chalcogenide amorphous semiconductors, the energy of chemical bonds between glass component atoms is relatively small (1.5−2.0 eV) [5], implying electron-hole character of conductivity.

Copper belongs to a small group of metals (Tl, K, Cu, Ag) [5, 6] which can enter the chalcogenide amorphous semiconductors to a significant ratio ($20 - 30$ at.%). It is known [5, 7, 8] that copper chalcogenide glasses possess dominant hole conductivity; although, in some copper-rich glass compositions, ionic conductivity was also detected [9].

In order to investigate the effect of copper content and electrical contacts on DC electrical conductivity of AsSe_yI_z glasses, measurements were made on $\text{Cu}_x(\text{AsSe}_{1.4}\text{I}_{0.2})_{100-x}$, for two different electrical contacts (silver and graphite).

2. Experimental details

Samples used for electrical conductivity measurements were prepared in a sandwich structure of electrodes. Polished plate samples with thickness of $2.01 - 3.84$ mm and areas of $12 - 47$ mm^2 (Table 1) have electrical contacts made of silver and graphite (Fig. 1).

A sophisticated temperature-controlled system (BECKMAN temperature controller model CTC 250 with an electric heater in isolated chamber and high resistance meter HP 4329A, Hewlett-Packard Japan, Ltd.) was used for the measurements (Fig. 2). The temperature was regulated by copper-constantan thermocouple with accuracy of ±0.5 K. All measurements of electrical resistance of the samples were made at twelve different temperatures in the range of $300 - 410$ K.

Table 1. Dimensions of samples.

	Sample	Dimensions $a \cdot b \cdot l$ (mm)
silver contacts	$AsSe_{1.4}I_{0.2}$	$4.15 \cdot 3.68 \cdot 2.02$
	$Cu_1(AsSe_{1.4}I_{0.2})_{99}$	$4.48 \cdot 4.39 \cdot 3.00$
	$Cu_5(AsSe_{1.4}I_{0.2})_{95}$	$4.52 \cdot 4.77 \cdot 2.77$
	$Cu_{15}(AsSe_{1.4}I_{0.2})_{85}$	$6.11 \cdot 5.55 \cdot 3.20$
	$Cu_{25}(AsSe_{1.4}I_{0.2})_{75}$	$3.50 \cdot 3.50 \cdot 3.36$
graphite contacts	$Cu_1(AsSe_{1.4}I_{0.2})_{99}$	$2.32 \cdot 2.25 \cdot 2.54$
	$Cu_5(AsSe_{1.4}I_{0.2})_{95}$	$6.20 \cdot 3.72 \cdot 2.65$
	$Cu_{10}(AsSe_{1.4}I_{0.2})_{90}$	$7.99 \cdot 5.87 \cdot 3.16$
	$Cu_{20}(AsSe_{1.4}I_{0.2})_{80}$	$6.61 \cdot 4.77 \cdot 3.84$
	$Cu_{25}(AsSe_{1.4}I_{0.2})_{75}$	$5.44 \cdot 3.72 \cdot 3.69$

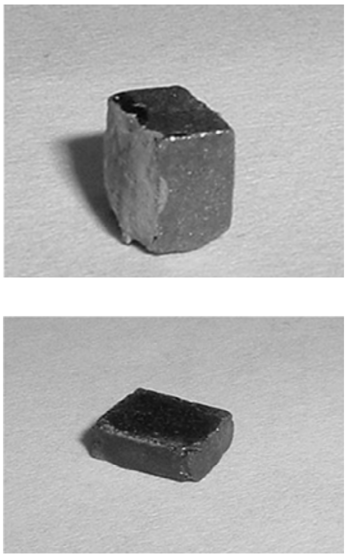

Figure 1. Samples with electrical contacts made of silver (a) and graphite (b).

Figure 2. A sophisticated temperature-controlled system.

3. Results and discussion

Figs. 3 and 4 refer to the samples with graphite and silver electrical contacts, giving the dependence of the logarithms of the specific electric conductivities on the reciprocal temperature values from 300 to 410 K. It is evident from the figures that the conductivity varies according to the well-known relation

$$\sigma = \sigma_0 \exp\left(\frac{-\Delta E_\sigma}{kT}\right) \tag{1}$$

where σ_0 is the constant of the specific conductivity, characteristic for the given material and ΔE_σ is the unique activation energy (width of the energy gap) [3]. It is also possible to determine the ΔE_σ and σ_0 from these measurements. ΔE_σ is determined from the

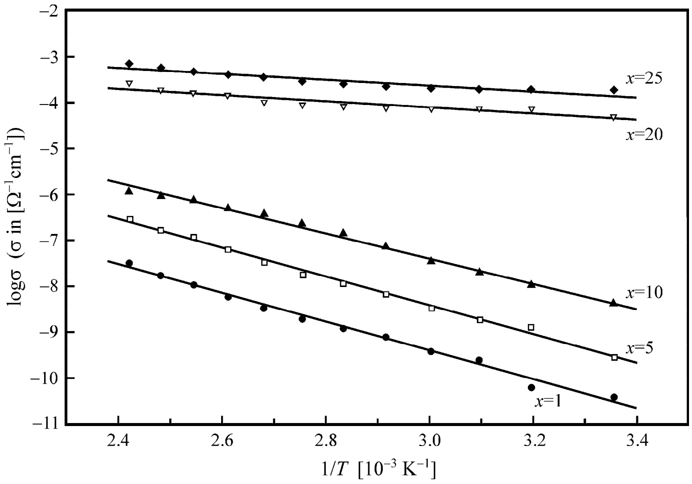

Figure 3. The measured temperature dependence of specific electrical conductivity for $\mathrm{Cu}_x(\mathrm{AsSe}_{1.4}\mathrm{I}_{0.2})_{100-x}$ glasses, $x = 1, 5, 10, 20$ and 25 with graphite electrical contacts.

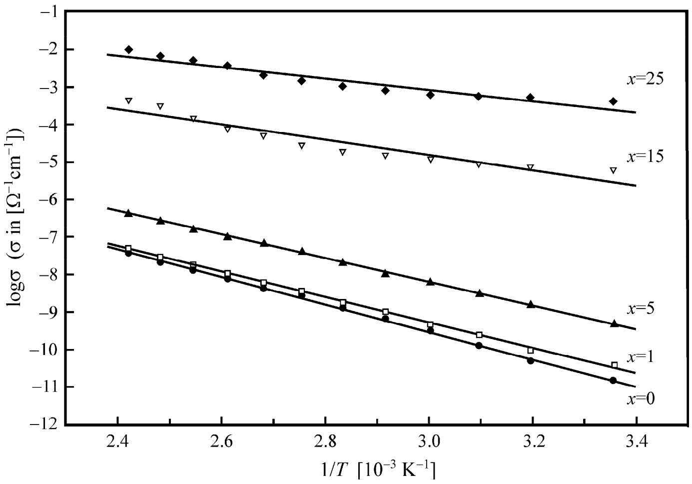

Figure 4. The measured temperature dependence of specific electrical conductivity for $\mathrm{Cu}_x(\mathrm{AsSe}_{1.4}\mathrm{I}_{0.2})_{100-x}$ glasses, $x = 0, 1, 5, 15$ and 25 with silver electrical contacts.

slopes of the curves, whereas σ_0 is determined by extrapolation of the linear portion of the curves to $1/T \to 0$. The values given in Tables 2 and 3 are obtained in this way. The values of specific electrical conductivity of investigated samples at room temperature are also given.

Table 2. Electrical properties of the samples with graphite electrical contacts.

x [at.%]	E_σ [eV]	σ_0 [$\Omega^{-1}\mathrm{cm}^{-1}$]	σ_{300K} [$\Omega^{-1}\mathrm{cm}^{-1}$]
1	0.62 ± 0.02	1.0	$3.6 \cdot 10^{-11}$
5	0.62 ± 0.01	9.7	$3.5 \cdot 10^{-10}$
10	0.54 ± 0.02	6.6	$4.8 \cdot 10^{-9}$
20	0.13 ± 0.02	$7.6 \cdot 10^{-3}$	$4.7 \cdot 10^{-5}$
25	0.13 ± 0.01	$1.9 \cdot 10^{-2}$	$1.4 \cdot 10^{-4}$

Table 3. Electrical properties of the samples with silver electrical contacts.

x [at.%]	E_σ [eV]	σ_0 [Ω^{-1}cm^{-1}]	σ_{300K} [Ω^{-1}cm^{-1}]
0	0.72 ± 0.01	24.6	$1.9 \cdot 10^{-11}$
1	0.67 ± 0.01	7.1	$4.1 \cdot 10^{-11}$
5	0.62 ± 0.01	15.5	$6.0 \cdot 10^{-10}$
15	0.41 ± 0.04	20.2	$3.1 \cdot 10^{-6}$
25	0.30 ± 0.03	26.9	$2.6 \cdot 10^{-4}$

It can be seen from Figures 3 and 4 that the specific electrical conductivity increases with rise of temperature and copper content in $AsSe_{1.4}I_{0.2}$. The curve slopes for the samples with lower percent of Cu in the glass composition are larger than the samples with a higher percent of Cu. According to the fact that the activation energy is proportional to the value of curve slope of specific electrical conductivity, this important parameter for semiconductor characterization shows the same dependence on copper content. The specific electrical conductivity has very low dependence on temperature for samples with high percent of Cu. There is a high probability for transition from semiconducting to metal character of electrical conductivity when samples have copper content more than 15 %.

On the other hand, it is shown that there is a significant impact of the experimental configuration on the achieved results. It is known that amorphous semiconductors are characterized by an electrical conductivity which depends on composition of starting components, condition of synthesis, melt cooling rate, purity of the starting components, thermal treatment, and other factors. The impact of electrical contacts can be very important for high resistance materials, and it was one of the main reasons for doing measurements presented in this paper. The results obtained for the samples with silver contacts show some higher specific electrical conductivity at room temperature than samples with graphite electrical contacts. It could be the effect of better overlaying of the samples surface with silver paste than graphite, and even a small diffusion of silver into the samples.

It can be also noticed that there are different impacts of the electrical contacts in dependence of measuring temperature and copper content in the samples. The impact of the electrical contacts on measurement of electrical conductivity for the samples with low copper content (up to 5 %) is negligible in the whole temperature range. The samples with high copper content (above 10 %) with silver contacts show respectable growth of electrical conductivity with rising temperature, in contrast to the samples with graphite contacts. For example, the sample with 25 % of copper with the silver electrical contacts at 410 K has an order of magnitude higher conductivity than the same sample with the graphite electrical contacts. This result could be the outcome of the interaction of silver and copper at higher temperatures.

It should be emphasized that the process of electrical transport in noncrystalline materials is considered in the light of three mechanisms: transport of charge carriers between delocalized states in the conduction ($E > E_C$) and valence band ($E < E_V$); removal of charge carriers in tail states; hopping of carriers between localized states which are close to the Fermi level (E_F). Since electrical conductivity of chalcogenide glasses is intrisic and conditioned by stimulation of electrons from the states near the peak of valence band in the localized states near the Fermi level or from the states near the Fermi level to conduction band, complicated structural form of glasses with enhanced content of particular elements in the composition might cause significant difference in localized states near E_F, and activation by some other transport mechanisms. These facts point to the necessity of very careful selection of an experimental configuration and sensitivity of measurement instruments to get correct results which represent the investigated material and not the measurement technique employed.

4. Conclusions

In this paper, electrical conductivity of Cu-As-Se-I amorphous semiconductor glasses has been investigated in the temperature range $300-410$ K. The samples with low percent of copper ($x = 0, 1$ and 5) have high resistance and expected small specific electrical conductivity $(10^{-11}-10^{-9})\ \Omega^{-1}\mathrm{cm}^{-1}$. The logarithm values of specific electrical conductivity increase almost linearly with increasing copper content in the $\mathrm{AsSe}_{1.4}\mathrm{I}_{0.2}$ composition. The samples with higher percent of copper ($x = 15, 20$ and 25) have relatively low resistance and electrical conductivity in an interval of $(10^{-5} - 10^{-3})\ \Omega^{-1}\mathrm{cm}^{-1}$. Logarithm values of specific electrical conductivity have very slow progress for samples with high percent of Cu. The samples with this amount of copper in the $\mathrm{AsSe}_{1.4}\mathrm{I}_{0.2}$ composition manifest transition from semiconducting to metal character of electric conductivity. The impact of the type of electrodes is only important for the samples with high percent of Cu and it is manifested as an increase of conductivity for silver electrodes. These results point to the necessity of very careful selection of an experimental configuration and sensitivity of measurement instruments to get correct results which represent the investigated material and not the measurement technique employed.

Acknowledgments

This work has been carried out with the financial support of the Ministry of Science of the Republic of Serbia (project ”Amorphous and Nanostructural Chalcogenides”) and the Provincial Secretariat of Science and Technological Development, Autonomous Province of Vojvodina (project ”Technology of obtaining and characterization of disordered semiconductors”).

References

1. S. Lukić, D. Petrović, *Complex noncrystalline chalcogenides*, (University of Novi Sad, Faculty of Sciences, Novi Sad, 2002).
2. M. Popescu, J. Optoelectron. Adv. Mater. **7**(4), 2189 (2005).
3. N. F. Mott, E. A. Davis, *Electronic processes in Non-crystalline materials*, (Clarendon Press, Oxford, 1971).
4. S. R. Lukić, D. M. Petrović, A. F. Petrović, J. Non-Cryst. Solids **241**, 75 (1998).
5. Z. U. Borisova, E. A. Bychkov, Yu. S. Tver’yanovich, *Interaction of Metals and Chalcogenide Glasses*, (Leningr. Gos. Univ., Leningrad, 1991).
6. Z. U. Borisova, *Chalcogenide Semiconducting Glasses*, (Leningr.Gos.Univ., Leningrad, 1983).

7. I. A. Sokolov, Z. U. Borisova, Fiz. Khim. Stekla **10**(1), 80 (1984).
8. I. A. Sokolov, Z. U. Borisova, Fiz. Khim. Stekla **11**(3), 304 (1985).
9. A. Feltz, *Amorphe und Glassartige Anorganische Festkorper*, (Akademie-Verlag, Berlin, 1983).

Journal of Research in Physics Vol. 31, No. 1, 69 - 78 (2007)

Particle Collision in Amorphous Medium at Equilibrium

Nikolay Peev
"Acad. G. Nadjakov" Institute of Solid State Physics, Bulgarian Academy of Sciences,
72 Tzarigradsko chaussee blvrd., 1784 Sofia, Bulgaria
e-mail: nasta@issp.bas.bg

Received: *June 19, 2007*

Abstract

The evaluation of the particle collision frequency in an amorphous medium at equilibrium is the subject of the present paper. The frequency of collisions was determined by the calculation of the collision probability of two arbitrary particles during their free path. This allows the evaluation of the number of particle collisions in a unit volume of the medium per unit time, which characterizes exactly the interaction intensity between the particles.
The possibility of growth or dissociation of a two-atomic particle with time was evaluated.

Key words: Nanoparticle, probability for collision, collision frequency

1. Introduction

Both, the physical and chemical processes are concerned with the frequency of particle collisions. It determines the rate of chemical interaction and the rate of nanoparticle nucleation, now very intensively investigated [8-11]. During the phase transition process it influences directly the heterogeneous nucleation of the new phase. The main requirement for the occurrence of all of these processes is for the particles to come into contact with each other during their collision. The rate of these processes increases with increasing collision frequency. As a rule, each of the processes occurs in an amorphous medium, and this is preciseley the case considered here. The present paper is a more detailed continuation of the previous paper [7].

2. Theory

2.1. Assumptions

The kinetics of the processes occurring in an amorphous medium have been for a long time the subject of many investigations [1-6]. In the present paper we will adhere to the already established view of these processes. The amorphous medium considered here consists of particles with different sizes - from single atoms to multiatomic particles. The medium is at equilibrium. There are no concentration gradient and/or temperature gradient - any oriented mass transport and/or heat transport are not present in the medium. There are no phase boundaries, and all processes occur in the medium volume. Only the processes of particle nucleation, their growth or dissociation take place in the medium.

A chemical interaction in the medium is possible only under equilibrium conditions. In this case, as a result of the collisions between the particles, there will arise the molecules that are being a product of the chemical interaction.

The particles of the medium do not interact with each other and, therefore, their collisions are fully probable. The movement of the particles in the medium is chaotic and there are no preferable directions of movement, which fully corresponds to the isotropic properties of the amorphous medium.

The particle, consisting of i atoms, will be denoted by a_i and the set of all particles, having the same size i, will be denoted by $[a_i]$ (the index i shows the number of the atoms in the particle and it corresponds directly to their radius r_i). The collision process will be considered within the limits of the time interval τ_i - the free path time. During the free path, the movement of the particle is straight and with a constant velocity v_i. We assume that during the free path the particles, having the same size, have equal velocity v_i and the same free path L_i. This assumption allows to simplify the calculations and generalize the results.

Two particles A and B are taken into consideration: $A \in [a_i]$ and $B \in [a_j]$. The particle A with a radius r_i is assumed to be immobile. The particle B with the radius r_j is mobile, with a migration velocity v_j and a free path L_j. The free path L_j is the longest way covered by the particle B between two consecutive collisions - at the end of this distance the particle undergoes scattering and changes the direction of its movement. The distance L_j is covered by the particle within the limits of the time interval τ_j: $\tau_j = L_j/v_j$.

As a consequence of the collision both particles may unite into a larger particle, as well as they may scatter, changing their directions. The problem concerning the consequences of the collisions is not discussed in the present paper.

At the initial moment, the particle B just undergoes scattering with an arbitrary particle of the medium. This scattering occurs at a distance r from the particle A and all directions of movement after the scattering are equally probable. This allows one to solve the problem: how great is the probability of collision between two particles with the radii r_i and r_j at a distance r?

2.2. Probability of collision

The medium is isotropic, and all directions of movement are equally probable. For the collision of the two particles it is necessary that the trajectory of the mobile particle B falls into the limits of the cone of "observation" (generally speaking) of particle A, viewed from the position of particle B (Figs. 1 and 2). This cone is defined solely by the distance r and by the particle sizes r_i and r_j. The radius r_i of the particle A is enlarged by the radius r_j of the particle B - for the collision of both particles it is necessary the particle B to hit the sphere with radius $(r_i + r_j)$, situated in the position of particle A. The space angle α on the top of the cone is, in fact, the space angle of "observation" (generally speaking) of the sphere with the radius $(r_i + r_j)$, viewed from the position of particle B (Figs. 1 and 2). The ratio of the space angle α to the space angle of the whole sphere, which is 4π and which consists of all possible directions of movement of the particle B,

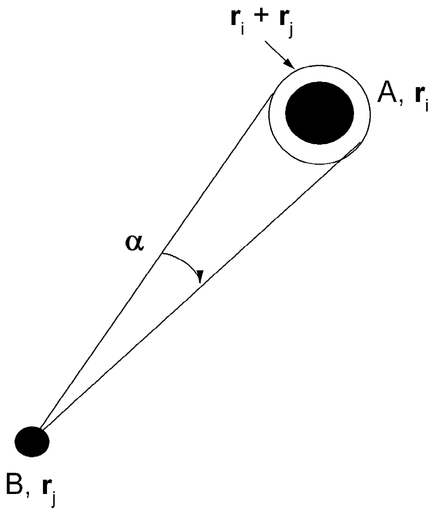

Figure 1. The initial position of the particles A and B and the space angle α.

gives the probability of collision ω of the two particles:

$$\omega = \frac{\alpha}{4\pi} \tag{1}$$

In order to collide within the limits of the time interval τ_j, it is necessary the distance r between the particles not to be longer than L_j - after passing this distance the particle B undergoes scattering and within the time interval τ_j will not collide with particle A.

The greater the distance r the smaller is the probability of the collision of the two particles, because the space angle α decreases with increasing the distance. When the value of the distance r becomes greater than $r^* = (L_j^2 + r_{ij}^2)^{1/2} - r_{ij}$, then the space angle α decreases sharper because not only the distance r but also the free path L_j will restrict the process of particle scattering: $(r_{ij} = r_i + r_j)$.

Within the limits of the above assumptions and using the definition of the space angle [12] the following expressions for the probability of collision of the particles A and B are obtained:

$$\omega_1(r) = \frac{(r + r_{ij}) - [r^2 + 2rr_{ij}]^{1/2}}{2(r + r_{ij})} \qquad \text{for} \quad 0 \leq r \leq r^* \tag{2}$$

$$\omega_2(r) = \frac{r_{ij}^2 - [r + r_{ij} - L_j]^2}{4L_j(r + r_{ij})} \qquad \text{for} \quad r^* \leq r \leq L_j \tag{3}$$

The point $r = r^*$ is common for both equations, and it is not difficult to prove that at this point the following equalities are fulfilled: $\omega_1(r^*) = \omega_2(r^*)$ and $\frac{d\omega_1}{dr}|_{r^*} = \frac{d\omega_2}{dr}|_{r^*}$. This means that the probability ω is a smooth and continuous function of the distance r between the particles over the whole interval of definition $(0, L_j)$. The second derivatives of ω_1 and ω_2 at the point r^* are not equal: $\frac{d^2\omega_1}{dr^2}|_{r^*} \neq \frac{d^2\omega_2}{dr^2}|_{r^*}$. For the values of r equal to or greater than L_j the probability of collision becomes zero and this may be seen from equation (3): for $r = L_j$ the probability is equal to zero and for $r > L_j$ it is negative, which is devoid of sense.

2.3. Frequency of collision

Two spheres around the particle A with the radii $(r+r_{ij})$ and $(r+r_{ij}+dr)$ respectively are taken into consideration (Fig. 2). The volume of the space enclosed between these spheres is $dV = 4\pi(r + r_{ij})^2 dr$. The density of the particles a_j in the medium is n_j and the number of these particles in the volume dV is:

$$dn_j = n_j dV = 4\pi n_j (r + r_{ij})^2 dr \tag{4}$$

where dr is a very small quantity and all particles a_j from equation (4) will have the same space angle α (equation (1)) and the same probability ω for the collision with the particle

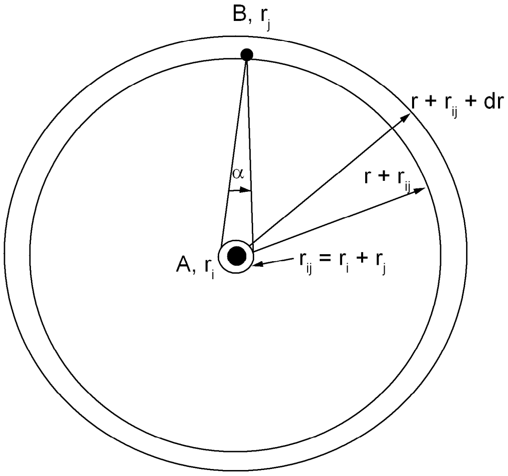

Figure 2. Determination of the frequency of collisions.

A. dN_j is the number of the particles a_j enclosed between the surfaces of the two spheres, which will collide with particle A within the time interval τ_j:

$$dN_j = \omega dn_j = 4\pi\omega n_j (r + r_{ij})^2 dr \tag{5}$$

The probability ω is respectively ω_1 or ω_2, depending on the value of r. Integrating equation (5) over all values of $r \in (0, L_j)$ one obtains the number of the particles a_j that will collide with particle A within the limits of the following time interval τ_j:

$$\begin{aligned} N_j &= 4\pi n_j \textstyle\int_0^{L_j} \omega (r + r_{ij})^2 dr = \\ &= 4\pi n_j \left(\textstyle\int_0^{r^*} \omega_1 (r + r_{ij})^2 dr + \int_{r^*}^{L_j} \omega_2 (r + r_{ij})^2 dr \right) = \pi n_j L_j r_{ij}^2 \end{aligned} \tag{6}$$

The particles N_j, situated very close to the particle A, will collide with it in a very short time interval - almost immediately. Other particles, situated far away from particle A, close to the periphery of the sphere with radius L_j, will collide after the time τ_j: $\tau_j = L_j / v_j$. Hence, during the time interval τ_j the particle A will have N_j collisions with the particles a_j, which allows the determination of the collision frequency ν_{Aj} of the particle A with the set of the particles $[a_j]$:

$$\nu_{Aj} = \frac{N_j}{\tau_j} = \pi n_j v_j r_{ij}^2 \tag{7}$$

Equation (7) divided by the surface area of the particle A gives the number of the collisions per unit area of this particle per unit time. This may be important in the case of particles with large dimensions:

$$\nu_{Aj}^* = \frac{n_j}{4} v_j (\frac{r_{ij}}{r_i})^2 \tag{8}$$

The particle A is an arbitrary particle from the medium and each particle a_i ($A \in [a_i]$) will experience the same number of collisions with the particles a_j per unit time. The density of the particles a_i in the medium is n_i. Then the number of collisions of the particles a_i with the particles a_j in a unit volume per unit time, following equation (7), will be:

$$\nu_{ij} = \pi n_i n_j v_j r_{ij}^2 \tag{9}$$

In an amorphous medium, as a result of the permanent collisions between the particles, there are particles of different sizes. We assume that the different kinds of collisions do not influence each other. In other words, the accomplishment of the given type of collisions occurs independently and does not influence the accomplishment of the other ones. Then the equation (6) may be written for all values of $j = (1, n^*)$, where n^* is the maximum size of the particles in the medium under the given conditions. Each of these equations will be written with the quantities v_j, τ_j, n_j, L_j, which characterize the corresponding set of particles $[a_j]$, $j \in (1, n^*)$. Each of these expressions will give the number of collisions that the particle A will experience with the corresponding set of particles during the time τ_j, $j \in (1, n^*)$. All these expressions allow the determination of the total frequency of collisions of particle A with all possible particles of the medium. The sum of all these frequencies gives the total number of the collisions of particle A with all other particles of the medium per unit time.

$$\nu_{Aj} = \pi \sum_{j=1}^{n^*} n_j v_j r_{ij}^2 \tag{10}$$

The particle A is an arbitrary particle of the medium. In its surroundings there will be n_i particles in the unit volume of the medium. In other words, each a_i particle of the medium (there are n_i of them in the unit volume) will experience the same number of collisions per unit time. In this way one obtains the total number of collisions in the unit volume per unit time between the set of the particles $[a_i]$, consisting of i atoms and all other particles of the medium.

$$\nu_i^* = \pi \sum_{j=1}^{n^*} n_i n_j v_j r_{ij}^2 \tag{11}$$

The total number of all possible collisions in the unit volume of the medium per unit time will be:

$$\nu^* = \pi \sum_{i=1}^{n^*} n_i \sum_{j=i}^{n^*} n_j v_j r_{ij}^2 \tag{12}$$

The aim of the present paper is the determination of the collision frequency of the particles in an amorphous medium at equilibrium. As already has been mentioned, the problem concerning the consequences of these collisions will not be discussed here. In other words, we do not consider the case when the particles bind in a larger particle as a consequence of the collision or when they only scatter.

3. Discussion

In the present paper, for an amorphous medium at equilibrium, by means of the probability of collision ω (equations (2) and (3)), within the frame of the made assumptions, the collision frequency of the particles was determined. The type of dependence $\omega(r)$ (equations (2) and (3)) is shown in Fig. 3. If the initial distance between the two particles

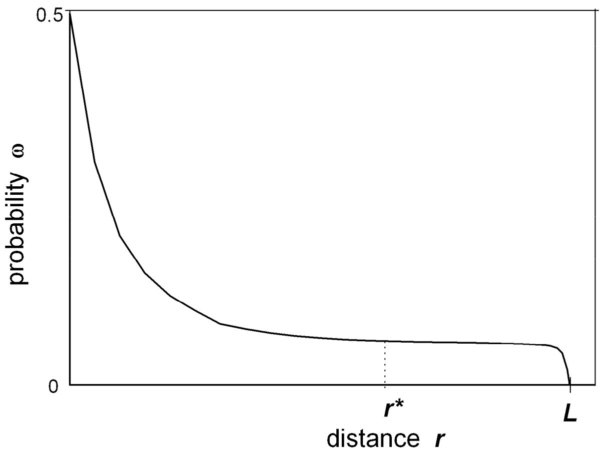

Figure 3. The probability of the particles collision.

is very small and tends to zero ($r \to 0$) then the probability of collision is 0.5 and it is so because the particles do not interact with each other. For very small initial distances the different directions of movement remain equally probable, therefore the space angle α never becomes greater than 2π and the probability of collision never becomes greater than 0.5 (equation (1)).

With increasing distance between the particles, the probability of collision decreases sharply and for the distances close to the value of the free path length ($r = L_j$) it becomes zero.

The probability of collision is, in fact, the probability for the trajectory of the mobile particle B to fall within the limits of the space angle α. We have assumed here that the collision of the two particles will take place exactly at the moment when this requirement is fulfilled. However, in practice, there are situations in which the fulfillment of this requirement will not lead inevitably to a collision between the particles - the trajectory of the mobile particle B may fall within the space angle α and nevertheless the collision with the immobile particle A may not take place. Besides this, in other situations, in which the trajectory does not fall into the space angle α and it is quite possible for both particles to collide. These situations are shown in Fig. 4. The trajectory I shows the situation in which particle B moves within the limits of the space angle α and, as a consequence of the collision with another particle C_1, it leaves this trajectory and does not collide with particle A (position B'). Such situations are quite possible. They will reduce the actual number of the particles which will collide with particle A - as a consequence of such situations the actual number will be smaller than the number N_j, determined by equation (6).

The trajectory II shows the case when particle B does not fall within the frame of the space angle α and, following the assumed model, it will not collide with particle A - it will not be among the particles N_j from equation (6) which will collide with particle A. However, it is possible, as a consequence of the collision with another particle C_2, for particle B to be deflected and to collide with particle A (position B''). This may occur under the following requirement - the scattering with particle C_2 must occur very close to

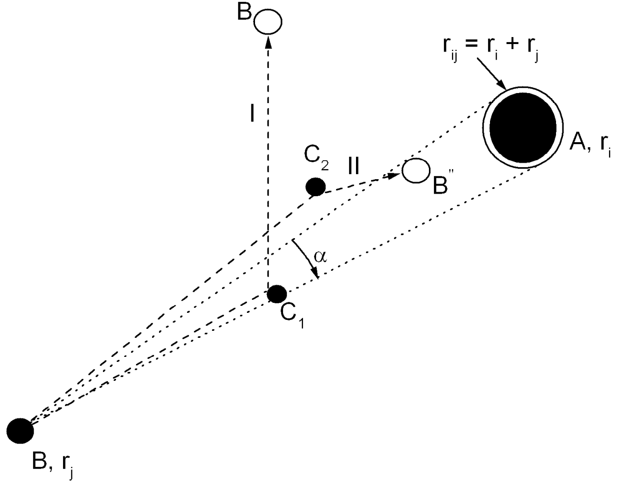

Figure 4. Situations *I* and *II*.

the space limited by the space angle α. Only then the particle B will collide with particle A within the limits of the following time interval τ_j - this requirement restricts considerably the number of these situations. The situations like II will lead to an increase of the actual number of collisions which particle A experiences for a time τ_j with particles a_j - the actual number will be greater than the number N_j calculated by equation (6), where these situations are not taken into account.

For taking into account these processes there are some difficulties concerning the final result of the collision of particle B with particle C_1 or C_2. Discussing these situations we have always assumed that the final result of the above collision is the scattering of both participating particles (see Fig. 4). However, it is quite possible that, as a consequence of the collision, the two particles unite in a larger particle - then the character of the process changes significantly and the considerations made here are not valid.

If, however, as a consequence of the collision, scattering of the particles takes place, then both considered processes have an opposite effect on the number of collisions per time τ_j - the first process leads to a decrease of this number while the second one leads to its increase. This circumstance allows the assumption that both processes will compensate each other, so that the actual number of the collisions per time τ_j will be very close to the value N_j, calculated by equation (6).

There are two possible ways of the behavior of a particle consisting of i atoms - either the particle grows further, becoming larger by joining other atoms of the medium, or it dissociates, becoming smaller and losing its atoms. The change of the number of the atoms in an a_i particle for a time Δt will be denoted by Δ_i. Then, the following expression is valid:

$$\Delta_i = \left(\frac{1}{\tau_i^+} - \frac{1}{\tau_i^-} \right) \Delta t \tag{13}$$

We assume that the process of growth of the particles or of their dissociation occurs only by joining or disjoining of single atoms. The τ_i^+ is the time interval which shows how often the surface of an a_i particle will be attacked by single atoms of the medium - this is the mean time between two consecutive collisions of the a_i particle with the single atoms of the medium. This time gives the rate of the growth process of the a_i particle by joining a part of these atoms. The τ_i^- is the time interval which shows how often single atoms from the surface of the a_i particle abandon it - it is the mean time between two consecutive abandoning of single atoms from the particle a_i. This time gives the rate of dissociation of this particle. It is obvious that in the case of negative values of Δ_i the atoms abandoning process occurs faster and the particle will dissociate and become smaller with time. On the contrary, if Δ_i is positive, then the particle will grow with time and become larger.

We will consider now a gas medium with equally large atoms of a radius $1 \cdot 10^{-8}$ cm, $(i = j = 1,\ r_1 = 1\ \text{Å},\ r_{11} = r_1 + r_1 = 2\ \text{Å})$. At room temperature, the migration velocity of the atoms in the gas medium is typically $v = 10^5$ cm/s [3, 5] and for the collision frequency of an atom with the other atoms one obtains:

$$\nu \cong 1.25 \cdot 10^{-10} n \qquad [\mathrm{s}^{-1}] \tag{14}$$

The coefficient before n shows that the number of the collisions per unit time is very strongly reduced with respect to the particle density. For a concentration of the particles of about $n = 10^{10}$ cm^{-3} (this is a very high vacuum about 10^{-15} bar) an atom of the medium will get only one collision per second. Therefore, under these conditions a formation of two-atomic particles in this medium will be very difficult - their concentration in the medium will be very low taking into account the very short lifetime of these particles. At higher pressures, in the range of $p = (10^{-3} \div 10^{-6})$ bar, where the concentration of the atoms is $n \cong (10^{19} \div 10^{22})$ cm^{-1}, the collision frequency of an atom with the other atoms of the medium increases to the values $\nu \cong (10^9 \div 10^{12})$ s^{-1}. It means that each ns (at the pressure 10^{-6} bar) an arbitrary atom of the medium will have a collision with another atom. For the pressure 10^{-3} bar the period of these collisions is approximately 1 ps. At these pressure values, the free path length [3, 5] is in the range $L = (10^{-2} \div 10)$ cm and the free path time is respectively $\tau \cong (10^{-7} \div 10^{-4})$ s.

In a sphere with radius L around an arbitrary atom of the medium the number of the atoms is $N_j^0 = 4/3\pi n L^3$. For $L = 10^{-2}$ cm (at a pressure of 10^{-3} bar and $n \cong 10^{22}$ cm^{-3}) this number is $N_j^0 \approx 10^{17}$. Following equation (6), only N_j from the N_j^0 atoms will collide with the considered atom: $N_j = \pi n L r_{ij}^2 \approx 3 \cdot 10^5$. The other atoms will not collide with this atom, but this does not mean that they will not collide with another atom of the medium.

We will consider now the behavior of a two-atomic particle following equation (13) - for this case the equation may be rewritten as follows:

$$\Delta_2 = \left(\frac{1}{\tau_2^+} + \frac{1}{\tau_2^-} \right) \Delta t \tag{15}$$

During each collision, there is a possibility for the two atoms to unite and thus form a new two-atomic particle. This particle may further grow with time and this possibility is characterized by the time $\tau_2^+ = 1/\beta^+ \nu_2$. The τ_2^+ is the time period in which two consecutive collisions of the two-atomic particle with the atoms of the medium occur. The ν_2 is the frequency of collisions, given by equations (7), in which one must take into account the collision frequency of a two-atomic particle with the single atoms of the medium. Taking into account the volume of the two particles and the inter-atomic distance between them and approximating the two-atomic particle by a sphere, we chose for its effective radius the value $r_2 = 2r_1 \approx 2$ Å and consequently $r_{21} = r_1 + r_2 \approx 3$ Å. At a pressure of 10^{-3} bar for the frequency ν_2 one obtains the value $\nu_2 \approx 3 \cdot 10^{12}$ s^{-1} and at a pressure of 10^{-6} bar the value is $\nu_2 \approx 3 \cdot 10^{9}$ s^{-1}. The β^+ is the probability of binding the two-atomic particle with the single atom into a larger three-atomic particle as a result of the collision. In other words, it gives that part of the total number of collisions which end up by binding of the two-atomic particle with a single atom, forming thus a tree-atomic particle.

Along with the growth process, occurring by joining of the single atoms of the medium with the corresponding particle, simultaneously occurs the process of dissociation of the same particle - in this process the particle loses its atoms and becomes smaller with time. This process is characterized (in the case of a two-atomic particle) by the time τ_2^- - after passing of this time the particle dissociates producing two single atoms. This lifetime depends on the binding energy of the two atoms in the particle. A similar problem is solved in [6], where considering the crystal growth process from the vapor the mean desorbtion time of an atom adsorbed onto the crystal surface was determined. This time was determined by the relation: $\tau^- = \tau_0 \exp(\varepsilon/kT)$, where ε is the binding energy of that adatom to the crystal surface and $\tau_0 \approx 10^{-13}$ s [6]. A rough and very approximate evaluation gives an average value of the energy $\varepsilon = 0.12$ eV. In that case the lifetime of a two-atomic particle would be about 10 ps. This evaluation is very approximate and the real value of the energy ε may be several times lower - therefore, the value of the lifetime τ_2^- might be one or two orders of magnitude lower as well. We have chosen the value $\tau_2^- = 10$ ps, stipulating that the accepted value may be significantly exceeded.

We have assumed that the probability for binding of the particles as a result of the collision is maximal in the case of a "frontal" collision (generally speaking) - the arising interaction during the collision between the particles in this case must be at a maximum. We have assumed that a reasonable value for the coefficient β^+ must be in the range of $0.1 - 0.3$, and we accepted the value $\beta^+ = 0.1$.

As already calculated, at the pressure of 10^{-6} bar the two-atomic particle in unit time will undergo ν_2 collisions with the single atoms of the medium: $\nu_2 \approx 3 \cdot 10^{9}$ s^{-1}. This means that: $\tau_2^+ = 1/\beta^+\nu_2 \approx 3$ ns, $\tau_2^- \approx 10$ ps $\ll \tau_2^+ = 3$ ns. The two-atomic particle will dissociate because the rate of the process of the abandoning of atoms from the particle exceeds significantly the rate of the process of particle growth. At a pressure of 10^{-3} bar, and under the same conditions one obtains: $\tau_2^+ = 1/0.1 \cdot 3 \cdot 10^{12} = 3$ ps ($\nu_2 \approx 3 \cdot 10^{12}$ s^{-1}). The both times τ_2^- and τ_2^+ are very close in magnitude - which means that the minimum deviation from this "fragile" equilibrium may be very crucial for the "future" of this particle. One may conclude that around this pressure value (within the frame of the approximations and assumptions made here) in the medium will arise conditions for the particle growth and formation of multi-atomic particles. At a lower pressure the particle dissociation process occurs faster than its growth. The appearance of multi-atomic particles in the medium under these conditions will be a process with a very low probability.

4. Conclusions

The paper defines the probability of collisions (ω) for an isotropic medium under equilibrium conditions. In the case of equally probable directions of movement the probability of collision is equal to the probability of the trajectory of the mobile particle to fall within the limits of the cone of "observation" (generally speaking) of the immobile particle, viewed from the position of the mobile one. This probability depends on the distance between the particles (r) , on their sizes (r_{ij}) and on the free path length (L).

With the aid of the probability of collisions (ω) the number of collisions (ν_{ij}) between the particles $[a_i]$ and $[a_j]$ in the unit volume of the medium per unit time was determined. Precisely, this quantity characterizes the interaction process between these kinds of particles. The intensity of this interaction depends on the temperature of the medium (T, v), on the densities of the particles (n_i, n_j), on their free path length (L) and on the size of the particles (r_{ij}).

By a rough approximation, the collision process of the particles in a gas medium at low pressures was evaluated. This evaluation shows that at the pressure values above 10^{-3} bar the conditions will arise for both the particle growth and formation of multiatomic particles. At lower pressures the dissociation process of the particles occurs faster than their growth, and the formed particle dissociates to single atoms before having enough time to grow.

References

1. J. I. Frenkel, *Kinetic Theory of Liquids*, (Publishing House of Acad. of Sci. of USSR, 1945).
2. J. I. Frenkel, Journal of Physics **9**, 385 (1945).
3. L. I. Maissel, R. Glang (editors), *Handbook of Thin Film Technology*, Parts 1 and 2, (Mc Graw Hill Hook Comp., 1970).
4. B. F. Ormont, *Introduction into the Chemical Physics and Crystal Physics of Semiconductors*, (Visshaya Shkola, Moscow, 1982).
5. S. Dushman, *Scientific foundations of vacuum technique*, (John Wiley & Sons, New York London, 1962).
6. B. Pamplin, *Crystal Growth*, (Pergamon press, Oxford - New York - Toronto - Sidney - Frankfurt, 1980).
7. N. S. Peev, "Comptes rendus de l'Acadmie Bulgare des Sciences", V. 60, No. 2, p. 121 (2007).
8. Y. Singh et al., J. Aerosols Science **33**, 1309 (2002).
9. J. R. Creighton et al., Appl. Phys. Letters **81**, 2626 (2002).
10. J. R. Creichton et al., J. Crystal Growth **261**, 204 (2004).
11. K. De Breacker et al., Phys. Review E **73**, 0262405-1 (2006).
12. G. A. Korn, Th. M. Korn, *Mathematical Handbook for Scientists and Engineers*, (McGraw-Hill Book Company, New York - San Francisco - Toronto - London - Sidney, 1968).

Journal of Research in Physics Vol. 31, No. 1, 79 - 86 (2007)

Magnetic Contribution to Specific Heat of a Series of Quasi Two-dimensional Antiferromagnetics

S. Radošević, M. Rutonjski, M. Pantić, D. Kapor
Department of Physics, Faculty of Sciences, Trg Dositeja Obradovića 4,
21000 Novi Sad, Serbia
e-mail: slobodan@if.ns.ac.yu

Received: *June 20, 2007*

Abstract

Quasi two-dimensional antiferromagnet is studied within the framework of the Heisenberg model, using Green's function method and Callen's expression for magnetization. Explicit expressions for the energy of the system and for the specific heat below critical temperature are derived. Finally, all results were applied to the special case of $Mn(HCOO)_2{\cdot}(ND_2)_2CO$ (MF2U) and compared with the experimental measurements.

Key words: Heisenberg antiferromagnet, sublattice magnetization, specific heat

1. Introduction

As noticed by many authors [1-3], in the last several decades there has been an increasing interest in quasi two-dimensional Heisenberg antiferromagnetics (Q2DHAFM), from both theoretical and experimental point of view. From a theoretical point of view, it is important to notice that a rather simple model yields an agreement with experiments.

For a wide class of compounds (K_2MnF_4, Rb_2MnF_4,...) the interactions between the ions that lie within a single plane of a crystal lattice are the dominant ones. Interactions between the ions from the neighboring and further planes are at least several orders of magnitude weaker [4] and play a secondary role. Because of that, these compounds are usually being referred to as quasi two-dimensional.

$Mn(HCOO)_2{\cdot}(ND_2)_2CO$ is an example of a Q2D antiferromagnetic material. In this system, Mn^{2+} ions, which are responsible for antiferromagnetism, are distributed within the layers (i.e. the planes of a 3D crystal lattice), and form simple quadratic lattice [3]. Layers are separated from each other by intervening urea molecules. This kind of system can be described by the standard Heisenberg Hamiltonian. However, according to Mermin-Wagner theorem [5], no long-range order (LRO) is possible in the isotropic Heisenberg model for a 2D case. For an LRO to exist, some form of anisotropy must be present in the system. Relying on previous works [1, 6-9], we use here the XXZ type of anisotropy, for a Heisenberg model with a spin $S = 5/2$.

Our analysis will be focused on the temperature dependence of magnetic specific heat for Q2DHAFM below the critical temperature. Since spontaneous sublattice magnetization enters our final expression for internal energy, the determination of this quantity is of primary interest. For that purpose we will employ Green's function (GF) method, widely used in theory of magnetism. The main problem with GF approach is the decoupling procedure for higher order GF's that enter equations for the initial ones. Tyablikov's decoupling procedure [10] has been used with great deal of success in theory of QHAFM's [1, 8], and it will the basis of calculations performed here. Due to the structure of the Hamiltonian and used GFs, in the process of determing internal energy of the system we are facing another difficulty: 3-operator correlation functions must be eliminated in favor of 2-operator correlation functions (see equations (9)-(12) below). In spite of the fact that two consecutive approximations are performed (one for GF's, and another one for correlation functions), we were able to produce result in agreement with experiment.

2. Internal energy of the system

The model used here for theoretical analysis is the Heisenberg model of a Q2DAFM with XXZ type of anisotropy and NN approximation. In the absence of external magnetic field, the Hamiltonian of such a system is (see Ref. [1])

$$\hat{H} = \frac{J}{2}\sum_{\vec{n},\vec{\lambda}}\left\{\hat{S}^{+}_{\vec{n}}(a)\hat{S}^{+}_{\vec{n}+\vec{\lambda}}(b) + \hat{S}^{-}_{\vec{n}}(a)\hat{S}^{-}_{\vec{n}+\vec{\lambda}}(b)\right\} - J\eta\sum_{\vec{n},\vec{\lambda}}\hat{S}^{z}_{\vec{n}}(a)\hat{S}^{z}_{\vec{n}+\vec{\lambda}}(b) \tag{1}$$

Here, J is NN exchange integral, η is anisotropy and vector $\vec{n}$ is a two-dimensional vector of square lattice. Index (a) refers to the first sublattice (spin "up") and index (b) to the second one (spin "down"). Also, quantization axis in b sublattice was rotated by 180°. We see from (1) that the internal energy of this antiferromagnet can be written as

$$\langle\hat{H}\rangle = \frac{J}{2}\sum_{\vec{n},\vec{\lambda}}\left\{\langle\hat{S}^{+}_{\vec{n}}(a)\hat{S}^{+}_{\vec{n}+\vec{\lambda}}(b)\rangle + \langle\hat{S}^{-}_{\vec{n}}(a)\hat{S}^{-}_{\vec{n}+\vec{\lambda}}(b)\rangle\right\} - J\eta\sum_{\vec{n},\vec{\lambda}}\langle\hat{S}^{z}_{\vec{n}}(a)\hat{S}^{z}_{\vec{n}+\vec{\lambda}}(b)\rangle \tag{2}$$

where $\langle ... \rangle$ denotes an average over the canonical ensemble. Our first task will be to eliminate correlation function $\langle\hat{S}^{z}_{\vec{n}}(a)\hat{S}^{z}_{\vec{n}+\vec{\lambda}}(b)\rangle$. This can be done with use of equations of motion for $\hat{S}^{+}_{\vec{n}}(a)$ and $\hat{S}^{-}_{\vec{n}}(a)$:

$$i\frac{d}{dt}\hat{S}^{+}_{\vec{n}}(a) = J\sum_{\vec{\lambda}}\hat{S}^{z}_{\vec{n}}(a)\hat{S}^{-}_{\vec{n}+\vec{\lambda}}(b) + J\eta\sum_{\vec{\lambda}}\hat{S}^{+}_{\vec{n}}(a)\hat{S}^{z}_{\vec{n}+\vec{\lambda}}(b) \tag{3}$$

$$i\frac{d}{dt}\hat{S}^{-}_{\vec{n}}(a) = J\sum_{\vec{\lambda}}\hat{S}^{z}_{\vec{n}}(a)\hat{S}^{+}_{\vec{n}+\vec{\lambda}}(b) - J\eta\sum_{\vec{\lambda}}\hat{S}^{-}_{\vec{n}}(a)\hat{S}^{z}_{\vec{n}+\vec{\lambda}}(b). \tag{4}$$

By multiplying equation (3) with $\hat{S}^{-}_{\vec{\rho}}(a)$ from the left, equation (4) with $\hat{S}^{+}_{\vec{\rho}}(a)$ from the right, averaging both sides of the corresponding equations and subtracting them, one finds

$$\begin{aligned}-J\eta\sum_{\vec{\lambda}}\langle\hat{S}^{z}_{\vec{n}}(a)\hat{S}^{z}_{\vec{n}+\vec{\lambda}}(b)\rangle = \frac{1}{4}\left\{\left\langle\hat{S}^{-}_{\vec{n}}(a)i\frac{d\hat{S}^{+}_{\vec{n}}(a)}{dt}\right\rangle - \left\langle i\frac{d\hat{S}^{-}_{\vec{n}}(a)}{dt}\hat{S}^{+}_{\vec{n}}(a)\right\rangle\right\} - \\ -J\sum_{\vec{\lambda}}\langle\hat{S}^{z}_{\vec{n}}(a)\hat{S}^{+}_{\vec{n}}(a)\hat{S}^{+}_{\vec{n}+\vec{\lambda}}(b)\rangle - J\sum_{\vec{\lambda}}\langle\hat{S}^{z}_{\vec{n}}(a)\hat{S}^{-}_{\vec{n}}(a)\hat{S}^{-}_{\vec{n}+\vec{\lambda}}(b)\rangle -\end{aligned}$$

$$-\frac{J\eta}{2}\sum_{\vec{\lambda}}\langle \hat{S}^{+}_{\vec{n}}(a)\hat{S}^{-}_{\vec{n}}(a)\hat{S}^{z}_{\vec{n}+\vec{\lambda}}(b)\rangle. \tag{5}$$

Now we can write down the energy per lattice site

$$\begin{aligned}\langle \hat{H}\rangle \equiv E = \langle \hat{H}_2\rangle + \frac{1}{4}\left\{\left\langle \hat{S}^{-}_{\vec{n}}(a)\, i\frac{d\hat{S}^{+}_{\vec{n}}(a)}{dt}\right\rangle - \left\langle i\frac{d\hat{S}^{-}_{\vec{n}}(a)}{dt}\hat{S}^{+}_{\vec{n}}(a)\right\rangle\right\} - \\ -J\sum_{\vec{\lambda}}\langle \hat{S}^{z}_{\vec{n}}(a)\hat{S}^{+}_{\vec{n}}(a)\hat{S}^{+}_{\vec{n}+\vec{\lambda}}(b)\rangle - J\sum_{\vec{\lambda}}\langle \hat{S}^{z}_{\vec{n}}(a)\hat{S}^{-}_{\vec{n}}(a)\hat{S}^{-}_{\vec{n}+\vec{\lambda}}(b)\rangle - \\ -\frac{J\eta}{2}\sum_{\vec{\lambda}}\langle \hat{S}^{+}_{\vec{n}}(a)\hat{S}^{-}_{\vec{n}}(a)\hat{S}^{z}_{\vec{n}+\vec{\lambda}}(b)\rangle,\end{aligned} \tag{6}$$

$$\langle \hat{H}_2\rangle = \frac{J}{2}\sum_{\vec{\lambda}}\left\{\langle \hat{S}^{+}_{\vec{n}}(a)\hat{S}^{+}_{\vec{n}+\vec{\lambda}}(b)\rangle + \langle \hat{S}^{-}_{\vec{n}}(a)\hat{S}^{-}_{\vec{n}+\vec{\lambda}}(b)\rangle\right\} \tag{7}$$

Correlation functions which consist of 2-operator product (for instance $\langle \hat{A}\hat{B}\rangle$) can be calculated with use of two-time temperature Green function of the form $\langle\langle \hat{A}|\hat{B}\rangle\rangle$ and spectral theorem. This procedure leaves 3-operator correlation functions undetermined. One way to resolve this situation is to put simply

$$\langle \hat{S}^{z}_{\vec{n}}(a)\hat{S}^{+}_{\vec{n}+\vec{\lambda}}(b)\hat{S}^{+}_{\vec{n}}(a)\rangle \simeq \langle S^{z}(a)\rangle\langle \hat{S}^{+}_{\vec{n}+\vec{\lambda}}(b)\hat{S}^{+}_{\vec{n}}(a)\rangle. \tag{8}$$

The above identity is based on Tyablikov's decoupling scheme for Green's functions

$$\langle\langle \hat{S}^{z}_{\vec{n}}\hat{S}^{\pm}_{\vec{m}}|\hat{B}\rangle\rangle \to \langle S^{z}\rangle\langle\langle \hat{S}^{\pm}_{\vec{m}}|B\rangle\rangle, \tag{9}$$

which is appropriate for higher temperatures. On the other hand, for low temperatures, we should expect better results with

$$\langle \hat{S}^{z}_{\vec{n}}(a)\hat{S}^{+}_{\vec{m}}(b)\hat{S}^{+}_{\vec{n}}(a)\rangle \simeq \langle S^{z}(a)\rangle\langle \hat{S}^{+}_{\vec{m}}(b)\hat{S}^{+}_{\vec{n}}(a)\rangle - \alpha\langle \hat{S}^{+}_{\vec{n}}(a)\hat{S}^{+}_{\vec{m}}(b)\rangle\langle \hat{S}^{-}_{\vec{n}}(a)\hat{S}^{+}_{\vec{n}}(a)\rangle. \tag{10}$$

The last relation is a modification of Callen's decoupling [11] of Green's functions in the case of an antiferromagnet:

$$\langle\langle \hat{S}^{z}_{g}\hat{S}^{\pm}_{f}|\hat{B}\rangle\rangle \to \langle S^{z}\rangle\langle\langle \hat{S}^{\pm}_{f}|\hat{B}\rangle\rangle - \alpha\langle \hat{S}^{\pm}_{g}\hat{S}^{\pm}_{f}\rangle\langle\langle \hat{S}^{\mp}_{g}|\hat{B}\rangle\rangle, \tag{11}$$

and $\alpha = \langle S^{z}\rangle/2S^{2}$ is the decoupling parameter introduced by Callen. As temperature approaches its critical value, α tends to zero, and Callen's decoupling reduces to the one of Tyablikov. Nevertheless, the contribution of Callen's corrections to Tyablikov's decoupling is significant for a specific heat close to T_N, since $d\alpha/dT$ is a very steep function in this region. Having all this in mind, we adopt a Callen-like procedure for higher order correlation functions, and equation (6) reduces to

$$\begin{aligned}E = \langle \hat{H}_2\rangle(1 - \frac{\langle S^{z}\rangle}{2}) + \frac{1}{4}\left\{\left\langle \hat{S}^{-}_{\vec{n}}(a)\, i\frac{d\hat{S}^{+}_{\vec{n}}(a)}{dt}\right\rangle - \left\langle i\frac{d\hat{S}^{-}_{\vec{n}}(a)}{dt}\hat{S}^{+}_{\vec{n}}(a)\right\rangle\right\} - \\ -\frac{\epsilon}{2}\langle \hat{S}^{+}_{\vec{n}}(a)\hat{S}^{-}_{\vec{n}}(a)\rangle - \\ -\frac{J\alpha}{4}\sum_{\vec{\lambda}}\left\{\langle \hat{S}^{-}_{\vec{n}}(a)\hat{S}^{-}_{\vec{n}+\vec{\lambda}}(b)\rangle\langle \hat{S}^{+}_{\vec{n}}(a)\hat{S}^{-}_{\vec{n}}(a)\rangle + \langle \hat{S}^{+}_{\vec{n}}(a)\hat{S}^{+}_{\vec{n}+\vec{\lambda}}(b)\rangle\langle \hat{S}^{-}_{\vec{n}}(a)\hat{S}^{+}_{\vec{n}}(a)\rangle\right\} - \\ -\frac{J\eta\alpha}{2}\sum_{\vec{\lambda}}\langle \hat{S}^{-}_{\vec{n}+\vec{\lambda}}(b)\hat{S}^{-}_{\vec{n}}(a)\rangle\langle \hat{S}^{+}_{\vec{n}+\vec{\lambda}}(b)\hat{S}^{+}_{\vec{n}}(a)\rangle.\end{aligned} \tag{12}$$

Here $\epsilon = J\langle S^z\rangle\eta z$ and z is the number of in-plane nearest neighbors. We have also taken into account the fact that in the absence of external field both sublattice magnetizations are equal, i.e. $\langle S^z(a)\rangle = \langle S^z(b)\rangle \equiv \langle S^z\rangle$. Green's function method within the Tyablikov decoupling scheme, together with equation (12) and Callen's approximation for sublattice magnetization, is sufficient for determining magnetic specific heat.

3. Green's function method

Let us define

$$G_1(\vec{n},\vec{m}) = \langle\langle \hat{S}^+_{\vec{n}}(a)|\hat{S}^-_{\vec{m}}(a)\rangle\rangle, \qquad \Gamma_1(\vec{n},\vec{m}) = \langle\langle \hat{S}^-_{\vec{n}}(b)|\hat{S}^-_{\vec{m}}(a)\rangle\rangle \tag{13}$$

$$G_2(\vec{n},\vec{m}) = \langle\langle \hat{S}^+_{\vec{n}}(a)|\hat{S}^+_{\vec{m}}(b)\rangle\rangle, \qquad \Gamma_2(\vec{n},\vec{m}) = \langle\langle \hat{S}^-_{\vec{n}}(b)|\hat{S}^+_{\vec{m}}(b)\rangle\rangle. \tag{14}$$

Equations of motion for the corresponding Green's functions (in energy representation) are

$$\begin{aligned}
\omega\langle\langle \hat{S}^+_{\vec{n}}(a)|\hat{S}^-_{\vec{m}}(a)\rangle\rangle_\omega &= \frac{i}{2\pi}\langle S^z\rangle + J\sum_{\vec{\lambda}}\langle\langle \hat{S}^z_{\vec{n}}(a)\hat{S}^-_{\vec{m}+\vec{\lambda}}(b)|\hat{S}^-_{\vec{m}}(a)\rangle\rangle_\omega + \\
&+J\eta\sum_{\vec{\lambda}}\langle\langle \hat{S}^+_{\vec{n}}(a)\hat{S}^z_{\vec{m}+\vec{\lambda}}(b)|\hat{S}^-_{\vec{m}}(a)\rangle\rangle_\omega, \qquad (15)\\
\omega\langle\langle \hat{S}^-_{\vec{n}}(b)|\hat{S}^-_{\vec{m}}(a)\rangle\rangle_\omega &= -J\sum_{\vec{\lambda}}\langle\langle \hat{S}^z_{\vec{n}}(b)\hat{S}^+_{\vec{m}+\vec{\lambda}}(a)|\hat{S}^-_{\vec{m}}(a)\rangle\rangle_\omega - \\
&-J\eta\sum_{\vec{\lambda}}\langle\langle \hat{S}^-_{\vec{n}}(b)\hat{S}^z_{\vec{m}+\vec{\lambda}}(a)|\hat{S}^-_{\vec{m}}(a)\rangle\rangle_\omega, \qquad (16)
\end{aligned}$$

and

$$\begin{aligned}
\omega\langle\langle \hat{S}^+_{\vec{n}}(a)|\hat{S}^+_{\vec{m}}(b)\rangle\rangle_\omega &= +J\sum_{\vec{\lambda}}\langle\langle \hat{S}^z_{\vec{n}}(a)\hat{S}^-_{\vec{m}+\vec{\lambda}}(b)|\hat{S}^+_{\vec{m}}(b)\rangle\rangle_\omega + \\
&+J\eta\sum_{\vec{\lambda}}\langle\langle \hat{S}^+_{\vec{n}}(a)\hat{S}^z_{\vec{m}+\vec{\lambda}}(b)|\hat{S}^+_{\vec{m}}(b)\rangle\rangle_\omega, \qquad (17)\\
\omega\langle\langle \hat{S}^-_{\vec{n}}(b)|\hat{S}^+_{\vec{m}}(b)\rangle\rangle_\omega &= \frac{i}{2\pi}\langle S^z\rangle - J\sum_{\vec{\lambda}}\langle\langle \hat{S}^z_{\vec{n}}(b)\hat{S}^+_{\vec{m}+\vec{\lambda}}(a)|\hat{S}^+_{\vec{m}}(b)\rangle\rangle_\omega - \\
&-J\eta\sum_{\vec{\lambda}}\langle\langle \hat{S}^-_{\vec{n}}(b)\hat{S}^z_{\vec{m}+\vec{\lambda}}(a)|\hat{S}^+_{\vec{m}}(b)\rangle\rangle_\omega. \qquad (18)
\end{aligned}$$

After applying Tyablikov's approximation (equation(9)), and going over to momentum space via

$$\hat{S}^-_{\vec{n}} = \frac{1}{\sqrt{N_2}}\sum_{\vec{k}_\parallel}\hat{S}^-_{\vec{k}_\parallel}e^{i\vec{k}_\parallel\vec{n}}\,, \tag{19}$$

we obtain the following systems for GF's

$$\begin{aligned}
[\omega-\epsilon]\langle\langle \hat{S}^+(a)|\hat{S}^-(a)\rangle\rangle_{\omega,\vec{k}_\parallel} - J(\vec{k}_\parallel)\langle S^z\rangle\langle\langle \hat{S}^-(b)|\hat{S}^-(a)\rangle\rangle_{\omega,\vec{k}_\parallel} &= \frac{i}{2\pi}2\langle S^z\rangle\\
J(\vec{k}_\parallel)\langle\langle \hat{S}^+(a)|\hat{S}^-(a)\rangle\rangle_{\omega,\vec{k}_\parallel} - [\omega+\epsilon]\langle\langle \hat{S}^-(b)|\hat{S}^-(a)\rangle\rangle_{\omega,\vec{k}_\parallel} &= 0 \qquad (20)
\end{aligned}$$

and

$$\begin{aligned}
[\omega-\epsilon]\langle\langle\hat{S}^{+}(a)|\hat{S}^{+}(b)\rangle\rangle_{\omega,\vec{k}_{\|}}-J(\vec{k}_{\|})\langle S^{z}\rangle\langle\langle\hat{S}^{-}(b)|\hat{S}^{+}(b)\rangle\rangle_{\omega,\vec{k}_{\|}} &= 0\\
J(\vec{k}_{\|})\langle S^{z}\rangle\langle\langle\hat{S}^{+}(a)|\hat{S}^{+}(b)\rangle\rangle_{\omega,\vec{k}_{\|}}+[\omega+\epsilon]\langle S^{z}\rangle\langle\langle\hat{S}^{-}(b)|\hat{S}^{+}(b)\rangle\rangle_{\omega,\vec{k}_{\|}} &= -\frac{i}{2\pi}2\langle S^{z}\rangle,
\end{aligned} \tag{21}$$

where N_2 is the number of unit cells within the layer, $J(\vec{k}_{\|})=Jz\gamma(\vec{k}_{\|})$, and the geometrical factor is given by

$$\gamma(\vec{k}_{\|})=\frac{1}{z}\sum_{\vec{\lambda}}e^{i\vec{k}_{\|}\vec{\lambda}}=\cos\frac{ak_x}{2}\cos\frac{ak_y}{2}. \tag{22}$$

Complete analysis of antiferromagnet described by Hamiltonian (1) needs to include GF's for adjoint operators. It is shown in [1] that it leads to the following expression for the energies of elementary excitations

$$\omega_{\vec{k}_{\|}}=\sqrt{\epsilon^{2}-(\langle S^{z}\rangle J(\vec{k}_{\|}))^{2}}. \tag{23}$$

Solutions of systems (20) and (21), together with (23) are

$$\langle\langle\hat{S}^{+}(a)|\hat{S}^{-}(a)\rangle\rangle_{\omega,\vec{k}_{\|}} = \frac{i}{2\pi}\frac{\langle S^{z}\rangle}{\omega_{\vec{k}_{\|}}}\left\{\frac{\omega_{\vec{k}_{\|}}+\epsilon}{\omega-\omega_{\vec{k}_{\|}}}+\frac{\omega_{\vec{k}_{\|}}-\epsilon}{\omega+\omega_{\vec{k}_{\|}}}\right\}, \tag{24}$$

$$\begin{aligned}
\langle\langle\hat{S}^{-}(b)|\hat{S}^{-}(a)\rangle\rangle_{\omega,\vec{k}_{\|}} &= \langle\langle\hat{S}^{+}(a)|\hat{S}^{+}(b)\rangle\rangle_{\omega,\vec{k}_{\|}}=\\
&= -\frac{i}{2\pi}\frac{\langle S^{z}\rangle^{2}J(\vec{k}_{\|})}{\omega_{\vec{k}_{\|}}}\left\{\frac{1}{\omega-\omega_{\vec{k}_{\|}}}+\frac{1}{\omega+\omega_{\vec{k}_{\|}}}\right\}.
\end{aligned} \tag{25}$$

Although needed for closing the system of equations with G_2, the function Γ_2 is of no interest for us. The corresponding correlation functions are determined by the spectral theorem

$$\langle\hat{S}^{+}_{\vec{n}}(a)\hat{S}^{-}_{\vec{n}}(a)\rangle = \langle S^{z}\rangle+\frac{1}{N_2}\sum_{\vec{k}_{\|}}\frac{\langle S^{z}\rangle\epsilon}{\omega_{\vec{k}_{\|}}}\coth\frac{\omega_{\vec{k}_{\|}}}{2k_BT}\,, \tag{26}$$

$$\langle\hat{S}^{-}_{\vec{n}}(a)\hat{S}^{+}_{\vec{n}}(a)\rangle = -\langle S^{z}\rangle+\frac{1}{N_2}\sum_{\vec{k}_{\|}}\frac{\langle S^{z}\rangle\epsilon}{\omega_{\vec{k}_{\|}}}\coth\frac{\omega_{\vec{k}_{\|}}}{2k_BT}\,, \tag{27}$$

$$\begin{aligned}
\left\langle\hat{S}^{-}_{\vec{n}}(a)i\frac{d\hat{S}^{+}_{\vec{n}}(a)}{dt}\right\rangle &= -\left\langle i\frac{d\hat{S}^{-}_{\vec{n}}(a)}{dt}\hat{S}^{+}_{\vec{n}}(a)\right\rangle=\\
&= -\langle S^{z}\rangle\epsilon+\frac{1}{N_2}\sum_{\vec{k}_{\|}}\langle S^{z}\rangle\omega_{\vec{k}_{\|}}\coth\frac{\omega_{\vec{k}_{\|}}}{2k_BT}\,,
\end{aligned} \tag{28}$$

$$\begin{aligned}
\langle\hat{S}^{\pm}_{\vec{n}}(a)\hat{S}^{\pm}_{\vec{n}+\vec{\lambda}}(b)\rangle &= \langle\hat{S}^{\pm}_{\vec{n}+\vec{\lambda}}(b)\hat{S}^{\pm}_{\vec{n}}(a)\rangle=\\
&= -\frac{1}{N_2}\sum_{\vec{k}_{\|}}\frac{\langle S^{z}\rangle^{2}J(\vec{k}_{\|})}{\omega_{\vec{k}_{\|}}}\coth\frac{\omega_{\vec{k}_{\|}}}{2k_BT}\,.
\end{aligned} \tag{29}$$

Finally, substituting these correlation functions in equation (12), we have

$$E=\frac{1}{N_2}\sum_{\vec{k}_{\|}}\frac{{\omega_{\vec{k}_{\|}}}^{2}-\epsilon^{2}}{\omega_{\vec{k}_{\|}}}\coth\frac{\omega_{\vec{k}_{\|}}}{2k_BT}-\langle S^{z}\rangle\epsilon-\frac{\langle S^{z}\rangle^{2}\epsilon}{4S^{2}}\left\{F_1(T)F_2(T)-F_3(T)\right\}, \tag{30}$$

where

$$\begin{aligned} F_1(T) &= \frac{1}{N_2}\sum_{\vec{k}_{\|}} \frac{\epsilon/\eta}{\omega_{\vec{k}_{\|}}} \coth\frac{\omega_{\vec{k}_{\|}}}{2k_BT}\,, \\ F_2(T) &= \frac{1}{N_2}\sum_{\vec{k}_{\|}} \frac{\epsilon^2-\omega^2_{\vec{k}_{\|}}}{\epsilon\omega_{\vec{k}_{\|}}}\eta\,\coth\frac{\omega_{\vec{k}_{\|}}}{2k_BT}\,, \qquad (31) \\ F_3(T) &= \frac{1}{N_2^2}\sum_{\vec{k}_{\|}}\sum_{\vec{q}_{\|}} \gamma(\vec{k}_{\|}+\vec{q}_{\|})\frac{\langle S^z\rangle^2 J(\vec{k}_{\|})J(\vec{q}_{\|})}{\omega_{\vec{k}_{\|}}\omega_{\vec{q}_{\|}}}\coth\frac{\omega_{\vec{k}_{\|}}}{2k_BT}\,\coth\frac{\omega_{\vec{q}_{\|}}}{2k_BT}\,. \end{aligned}$$

Sublattice magnetization, $\langle S^z\rangle$ may be obtained as follows. We rewrite equation (26) as

$$\langle \hat{S}^+_{\vec{n}}(a)\hat{S}^-_{\vec{n}}(a)\rangle = 2\langle S^z\rangle P_S(T) \qquad (32)$$

and use Callen's method for magnetization [11]. The result is a self-consistent equation for $\langle S^z\rangle$ (It is shown in [1] that this result is in agreement with the Mermin-Wagner theorem):

$$\langle S^z\rangle = \frac{(S-P_S(T))(1+P_S(T))^{2S+1}+(1+S+P_S(T))(P_S(T))^{2S+1}}{(1+P_S(T))^{2S+1}-(P_S(T))^{2S+1}}, \qquad (33)$$

which, together with (30), determine the energy of the system as a function of temperature. This allows us to introduce the specific heat

$$C_V = \frac{dE}{dT}. \qquad (34)$$

Expression (33) covers a temperature interval from $T = 0$ K to the Neel temperature. This means that the definition of specific heat (34), together with (30), (31) and (33), forms the equation for C_V below the critical temperature.

4. Numerical analysis

In the previous section, we have derived a self-consistent equation for magnetization and an equation for specific heat of quasi two-dimensional Heisenberg antiferromagnet with an arbitrary spin S. At this point we focus on a particular case of $\mathrm{Mn(HCOO)_2{\cdot}(ND_2)_2CO}$. This compound, an excellent example of Heisenberg antiferromagnet with a spin $S = 5/2$, has been well studied experimentally [3]. Experimental value for the exchange integral [3] is $J/k_B = 0.68$ K. As far as η is concerned, in principle, it would be possible to determine this quantity from experimental data on magnon dispersion. Unfortunately, no such data are available right now. On the other hand, detailed description of sublattice magnetization dependence on temperature is given in [1]. Within the same XXZ anisotropy model, the critical temperature is found to be

$$T_N = \frac{JS(S+1)}{3}\left[\frac{1}{N_2}\sum_{\vec{k}_{\|}}\frac{\eta}{\eta^2-\gamma(\vec{k}_{\|})^2}\right]^{-1}. \qquad (35)$$

Since the experimental value for low magnetic ordering temperature is $T_N = 3.77$ K, it follows from (35) that $\eta = 1.0104$. This result is in agreement with the estimation given in [6].

With these values for S, η and J/k_B, the solution of equation (33) for $\langle S^z \rangle$ is presented in Fig. 1, along with the function $d\langle S^z \rangle/dT$.

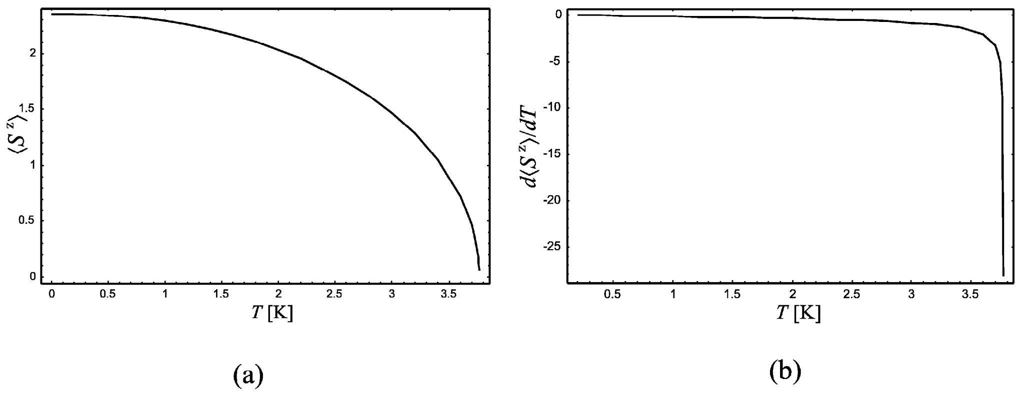

Figure 1. (a) Magnetization $\langle S^z \rangle$ as a function of temperature. (b) Derivate of the magnetization, $d\langle S^z \rangle/dT$, as a function of temperature.

Finally, specific heat, as function of temperature is presented in Fig. 2 (for comparison, on the same graph is plotted the specific heat calculated with simplified Tyablikov-like approximation for the correlation functions Eq. (8)), together with experimental results taken from [3].

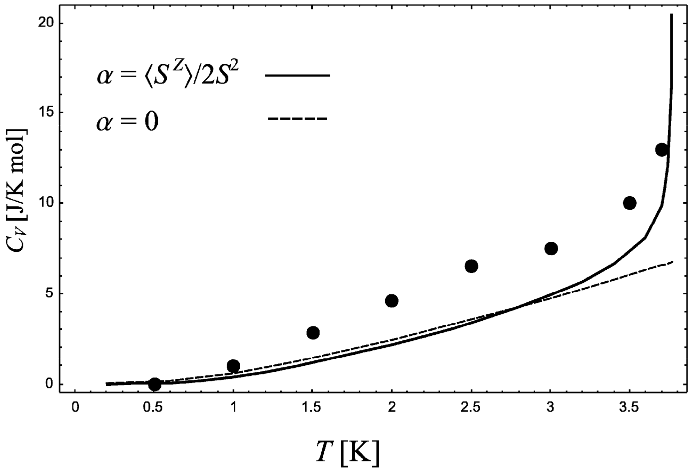

Figure 2. Temperature dependence of the specific heat calculated with Callen-like (solid line) and with Tyablikov-like (dashed line) approximation for the correlation functions. Dots represent experimental results (see Ref. [3]).

5. Results and discusion

Let us summarize the main results obtained here. The Hamiltonian (1) was used as a starting point in determing the internal energy of the system. We applied the GF method and random phase decoupling scheme to calculate relevant correlation functions. Numerical analysis (see Fig. 2) shows that a Callen-like procedure for correlation functions (equation(11)) produces divergent specific heat at T_N and simplified Tyablikov-like (equation(8)) procedure does not, since in Tyablikov's approximation one assumes that the correlations between $\hat{S}^{\pm}$ on one lattice site and $\hat{S}^z$ on another lattice site may be neglected. Disregarding these correlations in the definition of internal energy, we end up with just molecular field approximation. The Callen-like procedure preserves some of the correlations and numerical values for specific heat near T_N are closer to the experimental ones.

Acknowledgments

This work was supported by the Serbian Ministry of Science and Environmental Protection: Grant No 141018.

References

1. D. Kapor, M. Pantić, M. Manojlović and M. Pavkov, J. Res. Phys. **30**, 104 (2006).
2. E. Maunousakis, Rev. Mod. Phys. **63**, 1 (1991).
3. K. Takeda, M. Mito, K. Nakajima, K. Kakurai and K. Yamagata, Phys. Rev. B **63**, 024425 (2001).
4. A. F. M. Arts and H. W. de Wijn, Phys. Rev. B **15**, 4348 (1976).
5. N. Mermin and H. Wagner, Phys. Rev. Lett. **17**, 1133 (1966).
6. A. Cuccoli, T. Roscilde, V. Tognetti, R. Vaia and P. Verrucchi, arXiv:cond-mat/0303119v1
7. A. Cuccoli, T. Roscilde, V. Tognetti and P. Verrucchi, Phys. Rev. B **62**, 3771 (2000).
8. C. Pich and F. Schwabl, Phys. Rev B. **49**, 413 (1994).
9. C. Pich and F. Schwabl, J. Mag. Magn. Mater, **140**, 1709 (1995).
10. S. V. Tyablikov, *The Methods in the Quantum Theory of Magnetism*, (Plenum Press, New York, 1967).
11. H. B. Callen, Phys. Rev. **130**, 890 (1963).
12. B. Schroder, V. Wagner, N. Lehner, K. M. Kesharwani and R. Geick, Phys. Stat. Sol. (b) **97**, 501 (1980).
13. C. M. J. van Uijen and H. W. de Wijn, Phys. Rev. B **30**, 5265 (1984).
14. A. Cuccoli, V. Tognetti, R. Vaia and P. Verrucchi, Phys. Rev. B **56**, 14456 (1997).

Journal of Research in Physics

INFORMATION FOR CONTRIBUTORS

This Journal is devoted to the publication of original papers in **fundamental and applied physics**. The papers are in principle Articles, while Review Articles will be published by invitation only.

Contributors should send their manuscripts to Professor M. Škrinjar, Editor, Department of Physics, Faculty of Sciences, University of Novi Sad, Trg Dositeja Obradovića 4, 21000 Novi Sad, Serbia. (Fax #:+381-(21)-459-367; E-mail:fizika@uns.ns.ac.yu).

All manuscripts must be submitted in English. Manuscripts should be submitted in duplicate and should be typewritten and double spaced with wide margins. Only one side of each sheet should be used.

Manuscripts should consist of the title, followed by author(s) name(s) and adresse(s), abstract, key words, body of the text and the list of the references. Authors should *not* include references in Abstracts.

References must be numbered in the order in which they are referred to in the text: e.g. S. Wagner [1] or [1]. In the text, such abbreviations as Ref. [4] or Refs. [7-10] may be used.

The full references should be listed in the numerical order of citation in the text at the end of the article. Examples:

1. S. Autler and C. H. Townes, Phys. Rev. A **10**, 489 (1982). – for articles
2. E. U. Shirley, *The Theory of Molecules*, p. 399, (The University Press, Cambridge, 1954). – for books
3. C. E. Moore, "Selected Tables of Atomic Spectra", NSRDS-NBS3, Setion 5, National Bureau of Standards, Washington, DC 20025 (1975). – for reports.

Tables and figures should be sent with the paper on the separate pages. All photographs, graphs, and diagrams should be numbered consecutively. The legends should be typed on a separate page at the end of the article. The author's name, the figure number, and an indication of its proper orientation should be written on the back of each figure.

Line drawings must be submitted in camera-ready form and should be drawn in india ink on stiff white paper or printed on quality laser printer. The letters and symbols should be drawn so as to be clearly legible when reduced.

Authors are asked to suggest at least three referees who may revise their manuscript.

Page proofs will be sent to the author (or the first-mentioned author in a paper of multiple authorship) for checking. **Corrections to the proofs must be restricted to printer's errors**. Authors are particularly requested to return their corrected proofs as quickly as possible. Please note that **authors are urged to check their proofs carefully before return, since late corrections cannot be guaranteed for inclusion in the printed journal.**

The first-named author of each paper will receive 25 reprints free of charge.

Journal of Research in Physics

Volume 31 Number 1 October 2007

CONTENTS

Igor Salom *Poincare Generators as Quadratic Heisenberg Operators and Equations of Motion* 1

M. Ćirišan, R. J. Pelaez, S. Djurović, J. A. Aparicio and S. Mar *Stark Broadening Measurements of Low-intensity Xe II Lines in Pulsed Discharge* 11

J. Slivka, I. Bikit, M. Vesković, M. Krmar, N. Todorović, D. Mrdja, S. Forkapić *Evaluation of Efficiency Calibration Methods of Semiconductor Gamma Spectrometers* 19

I. Bikit, D. Mrdja, I Aničin, M. Vesković, S. Forkapić *Cross-section for X-ray Production by Cosmic Muons* 31

A. Kovalchuk, G. Beshkov, S. Shapoval *Dehydrogenation of Low-temperature ECR-plasma Silicon Nitride Films under Rapid Thermal Annealing* 37

K. Ivanović and Ž. Kovačević *Looking for the Resonant States in High-temperature Superconductors with Impurities* 47

D. D. Štrbac, S. R. Lukić, D. M. Petrović, G. R. Štrbac, J. M. Gonzalez-Leal, A. Srinivasan *Study of the Composition Homogeneity of Amorphous Thin Films from the System Cu-As-S-Se by Scanning Electron Microscopy* 55

M. P. Slankamenac, S. R. Lukić, F. Skuban, I. O. Gut, M. Živanov *Influence of Electrical Contacts on Measurement of Electrical Conductivity of Amorphous Semiconductors from the System Cu-As-Se-I* 61

Nikolay Peev *Particle Collision in an Amorphous Medium at Equilibrium* 69

S. Radošević, M. Rutonjski, M. Pantić, D. Kapor *Magnetic Contribution to Specific Heat of a Series of Quasi Two-dimensional Antiferromagnetics* 79